T. Swasdisevi et al.

6

thermal conductivity, density and viscosity of the gas and particles are essentially constant. (ii) The heat loss through the vessel wall and draft plates is negligible. (iii) The temperature of each particle may be represented by an average value. (iv) Direct particle-to-particle heat transfer is negligible. (v) The Ranz-Marshall correlation [18] is applicable for gas-to-particle heat transfer in the spout region, while the correlation of Sartori et al. is applicable in the downcomer region.

The thermal equation is as follows:

$$\frac{\partial}{\partial t}(\varepsilon T_{\rm g}) + \frac{\partial}{\partial x_i}(\varepsilon u_{\rm i} T_{\rm g}) = \frac{Q_{\rm s}}{\rho_{\rm g} c_{\rm p,g}} + \frac{1}{\rho_{\rm g} c_{\rm p,g}} \frac{\partial}{\partial x_i} \left( k_{\rm c} \frac{\partial T_{\rm g}}{\partial x_i} \right), \tag{4}$$

where  $Q_s$  is the heat transfer rate between the surrounding gas and a particle in a unit volume:

$$Q_{\rm s} = \frac{6(1-\varepsilon)}{d_{\rm p}} h_{\rm p} (T_{{\rm p},k} - T_{\rm g}). \tag{5}$$

The heat transfer coefficient  $(h_p)$  is estimated as follows. The Ranz-Marshall correlation [18] for the spout region is:

$$Nu = 2.0 + 0.6Pr^{1/3}Re^{1/2}.$$
 (6a)

The correlation of Sartori et al. [19] for downward moving beds in the downcomer region is:

$$Nu = 1.54 Pr^{1/3} Re^{0.57}, (6b)$$

where:

$$\begin{aligned} \text{Nu} &= h_{\text{p}} d_{\text{p}} / k_{\text{c}}, \\ \text{Pr} &= c_{\text{p,g}} \mu_{\text{g}} / k_{\text{c}}, \\ \text{Re} &= \frac{|\bar{v}_{\text{p}}}{\mu_{\text{g}}} \frac{-u | \rho_{\text{g}} \varepsilon d_{\text{p}}}{\mu_{\text{g}}}. \end{aligned}$$

#### 2.2. Particle motion and temperature

The particle motion is calculated by simultaneously applying Newton's law to each individual particle while taking into account the external gravity force  $(f_g)$ , the gassolid drag forces  $(f_D)$ , and the contact forces between the particles and against the wall  $(f_C)$ . The drag force is the sum of the reactionary forces in (3) and the pressure gradient as follows:

$$f_{D} = \left(\frac{\beta}{1 - \varepsilon} (u - v_{p}) - \frac{\partial p}{\partial x}\right) V_{p}. \tag{7}$$

where  $V_p$  is the volume of a particle. The contact force is calculated by using the DEM correlation proposed by Cundall and Strack [20]. An individual particle often comes into simultaneous contact with several particles or the wall. Therefore, the

contact force  $f_C$  is the sum of all such forces. Newton's equation of motion can be written as follows:

$$\ddot{x} = \frac{f_{\rm C} + f_{\rm D}}{m} + g. \tag{8}$$

where m is the mass of the particle. The rotational motion of a particle caused by the tangential force is calculated from

$$\dot{\omega} = \frac{T}{I},\tag{9}$$

where T is the torque caused by the tangential components of the contact forces and I is the moment of inertia of the particle.

The energy balance for a particle is given by the following equation:

$$\rho_{p}c_{p,k}V_{p}\frac{dT_{p,k}}{dt} = -h_{p}A_{p,k}(T_{p,k} - T_{g}), \tag{10}$$

where  $V_p$  is the volume of the particle.  $c_{p,k}$  and  $A_{p,k}$  are the specific heat and external surface area of the particle.

#### 3. MATERIALS AND METHOD

The geometry of the vessel is set as close as possible to the medium-scale experimental apparatus of Kudra et al. [3]. As shown in Fig. 1, the normal distance is the spacing between the draft plate and the slanting base. The particles are spherical and monodisperse. Their physical properties are based on shelled corn. These properties and the dimensions of the vessel used in the present investigation and the experiments of Kudra et al. [3] and Kalwar et al. [21] are summarized in Table 1. The number of particles corresponding to the same bed height of 0.90 m as the experiments is approximately 26 000. The angle of the slanted base is 60°. The friction coefficients (both static and kinetic) and the Poisson's ratio of the particles are 0.30 and 0.25, respectively. The coefficient of restitution is taken to be 0.90. The appropriate value of the spring constant at 800 N/m in the contact force model was determined in the same manner as Kawaguchi et al. [7]. Air at 20°C and 1 atm is used as the fluid for investigating the particle dynamics in the absence of heat transfer. The gas flow is two-dimensional.

The maximum allowable time step for numerical intergration is estimated using the oscillation period of the spring-mass system recommended by Tsuji et al. [6].

$$\Delta t \leqslant \frac{\pi \sqrt{m/k}}{5},\tag{11}$$

where  $\Delta t$  and k are the integration time step and spring constant, respectively. The actual time step used is 0.0003 s. To determine the minimum spouting velocity, the superficial gas velocity is gradually reduced from a sufficiently large value. The superficial gas velocity is defined as the gas velocity over an empty cross-

Table 1. Properties of particles and dimensions of vessels used in the DEM simulation and the experiments of Kudra et al. [3] and Kalwar [21]

	Simulation	Experiments	
Particle			
diameter, dp (mm)	8.0	8.0	
density, $\rho_p$ (kg/m <sup>3</sup> )	1231	1231	
sphericity, $\phi$	l .	0.755	
Vessel			
width, W (mm)	495	500	
depth, Lb (mm)	40	40	
width of gas inlet, Wi (mm)	33	33	
width of draft plates, Wd (mm)	55	50	
entrance height, He (mm)	95	100	
spout height, H <sub>d</sub> (mm)	912	900	
normal distance (mm)	37.97	42.64	
slant angle, $\theta$	60	60	
Dimensionless sizes			
$W/W_{i}$	15	15.1	
$W/d_p$	61.8	62.5	
$W_i/d_p$	4.1	4.1	
$W_d/W_i$	1.6	1.5	

section of the rectangular vessel. The calculation results will be verified against the experimental results of Kudra et al. [3] and Kalwar [21].

In the case of convective gas-to-particle heat transfer, air and particles at 33°C are used as the initial temperature condition. The average properties of air are taken at 65.6°C and 1 atm while the inlet air temperature at the bottom is 150°C. This temperature is suitable for drying shelled corn. The geometry of the vessel and the physical properties of the particles are summarized in Table 1. The specific heat of particle (shelled corn) is 2 400 J/kgk.

### 4. RESULTS AND DISCUSSION

### 4.1. Minimum spouting velocity (ums) and pressure drop

The calculated pressure drop versus the inlet gas velocity is shown in Fig. 2.  $u_{\rm ms}$  represents a turning point at which a slight reduction of the superficial gas velocity causes the spout to collapse and the pressure drop to significantly increase. Figure 3 shows some snapshots of the flow patterns in the spouted bed with draft plates. In Fig. 3, the spout begins to collapse at the superficial gas velocity 1.25 m/s. The minimum spouting velocity and corresponding pressure drop can be estimated from the correlation given by Kudra et al. [3] as follows:

$$u_{\rm ms} = \sqrt{g w_{\rm d}} \phi^{0.68} \theta^{-0.084} \left( \frac{\rho_{\rm p} - \rho_{\rm g}}{\rho_{\rm g}} \frac{H_{\rm e}}{L_{\rm b}} \right)^{0.15} \left( \frac{w_{\rm d} d_{\rm p}}{w_{\rm i} H_{\rm b}} \right)^{0.084}. \tag{12}$$

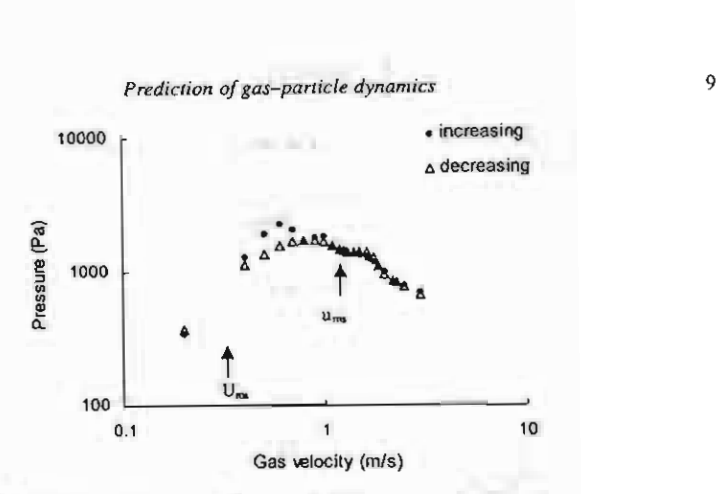


Figure 2. Calculated pressure drop versus the superficial inlet gas velocity of the spouted bed with draft plates.

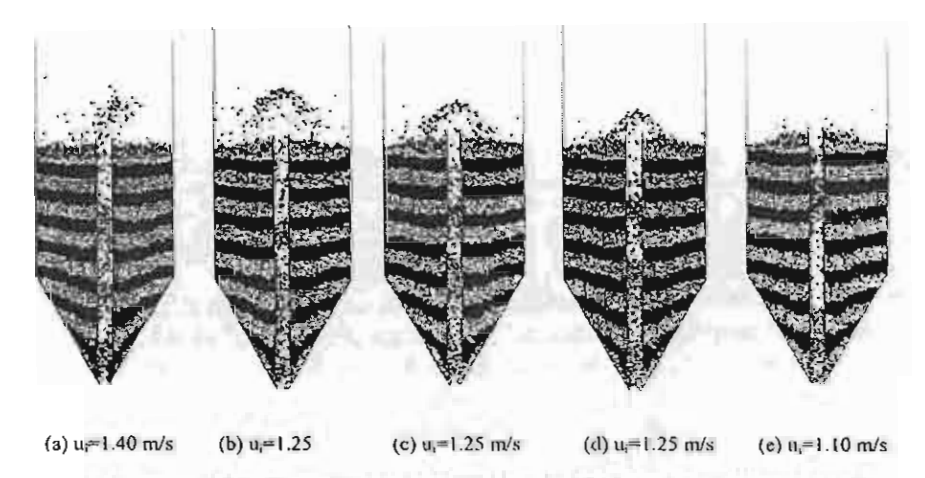


Figure 3. Snapshots of the flow patterns in the spouted bed with draft plates for various gas velocities. This figure is published in colour on http://www.ingenta.com

The calculated minimum spouting velocity ( $u_{\rm ms}$ ) at a bed height 0.9 m is 1.25 m/s, while the prediction of Kudra's is 1.12 m/s. The small discrepancy in the  $u_{\rm ms}$  values may be ascribed to the slight differences in the vessel geometry. In the simulation,  $H_{\rm e}$  and  $W_{\rm d}$  are 95 and 55 mm, respectively, whereas they are 100 and 50 mm in the experiment. Based on an experimental value of 1.12 m/s and (12), the predicted  $u_{\rm ms}$  under the same vessel geometry should be  $(1.12)(55/50)^{0.5}(95/100)^{0.15}(55/50)^{0.084} = 1.18$  m/s, which agrees well with the simulation value of 1.25 m/s.

The correlation for the spouting pressure drop is as follows:

$$\Delta P_{\text{ms}} = \rho_{\text{b}} (gH_{\text{d}})^{0.79} \theta^{0.33} \left( \frac{W_{\text{s}}}{w_{\text{b}} L_{\text{b}} \rho_{\text{b}}} \right)^{0.46} \left( \frac{s}{w_{\text{d}}} \right)^{0.42} \left( \frac{w_{\text{i}} H_{\text{b}}}{w_{\text{d}} H_{\text{d}}} \right)^{0.11}. \tag{13}$$

As in the experiment of Kalwar [2], the pressure drop is measured between a central height of 11 mm above the bottom and the atmospheric pressure. The plotted pressure drop is time-smoothed over 1.8 s because slug flow causes the pressure to fluctuate strongly. Initially, the pressure drop increases as the superficial gas velocity increases. When the velocity reaches a certain value, the pressure drop starts to decrease gradually. Conversely, when the superficial gas velocity decreases from a sufficiently high value, the pressure drop gradually increases. Then it increases significantly after passing the  $u_{\rm ms}$  point. The hysteresis loop in the 2DSB occurs as shown in Fig. 2 because the flow resistance of the dense packed bed is higher than the loose one. In practice, the hysteresis loop will be shrunk somewhat if the increase-decrease cycle is repeated by starting with a loose rather than a relatively dense packed bed. However, the hysteresis cannot be eliminated entirely due to the inherent irreversibility of the jet penetration phenomenon [22]. The small discrepancy between our calculated minimum spouting pressure drop and Kudra's prediction (1.40 versus 1.20 kPa or 1.17:1) can be attributed to the above difference in the predicted and experimental  $u_{ms}$  (1.25 versus 1.12 m/s or  $(1.25/1.12)^2 = 1.24:1$ ). It is assumed here that the pressure drop is proportional to the square of the velocity.

### 4.2. Particle motion in the spout region

In this section, the spatial distribution of the particle velocity is investigated for two regions: the spout and the downcomer. To save computer memory, the particle velocities are recorded every 0.03 s. Next the particle velocities are time-smoothed over a period of 1.8 s corresponding to 60 snapshots. Figure 4a shows the profile of the time-smoothed vertical velocity of the particles and Fig. 4b shows the time-smoothed void fraction at different heights in the spout region when the inlet superficial gas velocity is 1.40 m/s ( $u_i = 1.12u_{ms}$ ). In Fig. 4,  $z/R_d$  is the

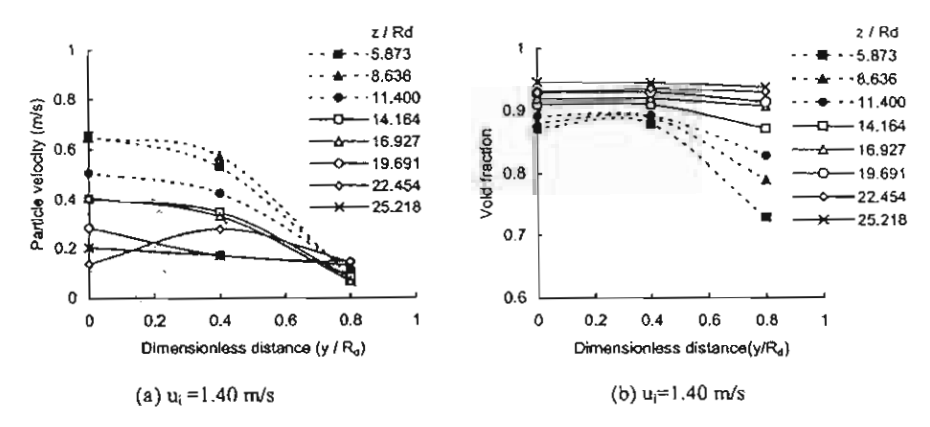


Figure 4. The profiles of (a) the vertical particle velocity and (b) the void fraction at different heights in the spout region.

dimensionless height. The dimensionless distance  $(y/R_d)$  is measured from the central axis of the spout. The draft plates are located at  $y/R_d=\pm 1$ . The vertical particle velocity in the spout decreases against the increased height because of slugging. The slugs formed in the upper region increase the flow resistance in the spout. The vertical particle velocities adjacent to the draft plates are lower than the local average value and some particles even fall down. In the present work, some slug flow occurs in the spout region at the minimum spouting velocity  $(u_{ms}=1.25 \text{ m/s})$ . The slugs gradually disappear when the superficial gas velocity further increases. The fountain is stable at  $u_i > 1.5u_{ms}$  ( $u_i > 1.86 \text{ m/s}$ ). The observed formation of slugs in the simulation of the 2DSB, which is related to the waves of particles developed in the lower region of the spout [23], is consistent with reported experimental results.

### 4.3. Particle motion in the downcomer region

The profile of the vertical particle velocity in the downcomer region is shown in Fig. 5 for various heights. Here, downward velocities are plotted as positive values. The draft plates are located at  $y/R_d=\pm 1$  and the wall at  $y/R_d=\pm 9$ . As the height increases, the vertical particle velocities decrease in the vicinity of the draft plates, whereas those near the vessel walls increase with the increasing height. Generally, the downward particle velocities near the walls are lower than those near the draft plates because the increased flow resistance between the particles and the slanting base retards the return flow of the particles to the spout. In the lower region  $(z/R_d=5.873-11.400)$ , the downward particle velocities are higher than those in the upper region  $(z/R_d=14.164-25.218)$  because of the reduction in the cross-sectional area by the slanting base.

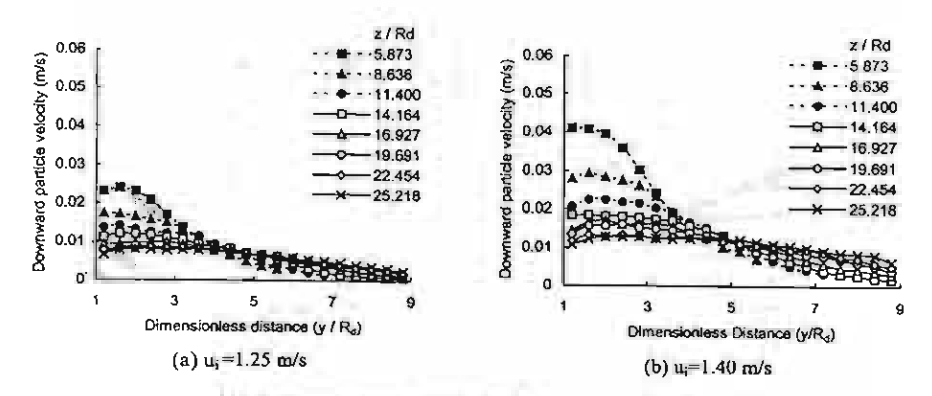


Figure 5. Downward particle vertical velocity profile in the downcomer for various dimensionless heights at two superficial gas velocities.

T. Swasdisevi et al.

### 4.4. Particle circulation rate

The particle circulation rate can be estimated from the particle velocity above the slanting base, voidage, particle density and cross-sectional area of the downcomer as follows:

$$W_{\rm s} = A_{\rm d} v_{\rm ps} \rho_{\rm p} (1 - \varepsilon), \tag{14}$$

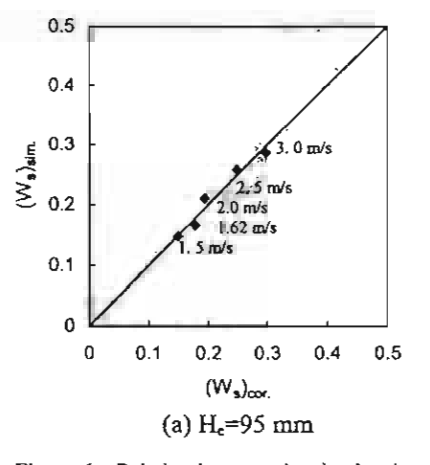
where  $W_s$ ,  $A_d$ ,  $v_{ps}$ ,  $\rho_p$  and  $\varepsilon$  are the particle circulation rate, cross-sectional area of the downcomer, particle velocity above the slanting base, particle density and voidage, respectively. As expected, the particle circulation rate increases with the increasing gas flow rate as shown in Fig. 6.

4.4.1. Effect of the separation height  $(H_e)$  on the particle circulation rate. The obtained empirical correlation between the particle circulation rate and gas velocity is as follows:

$$W_{\rm s} = \begin{cases} 0.3251u_{\rm i}^{0.5} - 0.265 & \text{for } H_{\rm e} = 95 \text{ mm} \\ 0.1641u_{\rm i}^{0.5} + 0.111 & \text{for } H_{\rm e} = 152 \text{ mm}. \end{cases}$$
 (15)

Figure 6 compares the simulated particle circulation rate and that of the above correlation for both separation heights, 95 and 152 mm. When the separation height increases from 95 to 152 mm, the normal distance in Fig. 1 increases from 37.97 to 66.47 mm, thus resulting in a larger number of circulating particles entering the spout.

4.4.2. Effect of the coefficient of friction on the particle circulation rate. The obtained empirical correlation for the circulation rate at 1.25 m/s (=  $u_{ms}$ ) as a



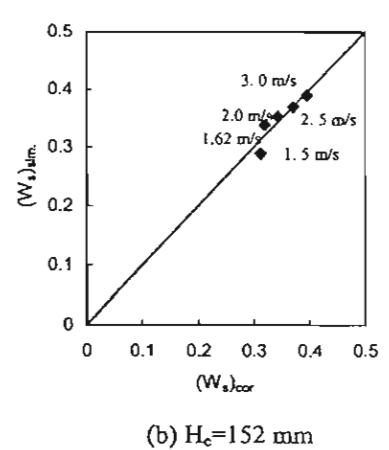


Figure 6. Relation between the simulated particle circulation rate and that of correlation (15) at various inlet gas velocities ( $H_c = 95$  and 152 mm).

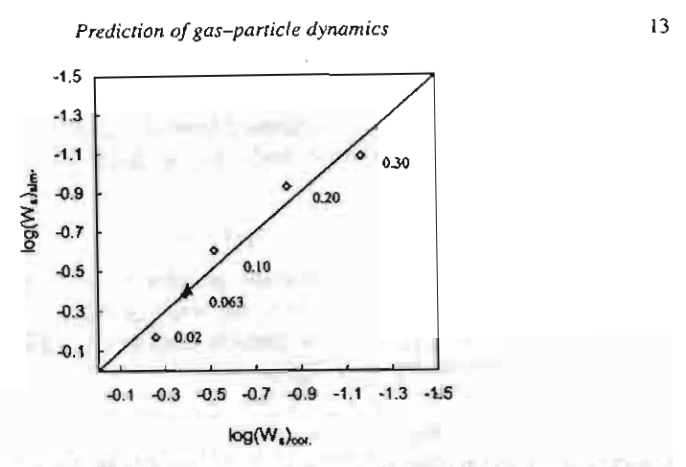


Figure 7. Relation between  $log(W_s)$  of simulation and that of correlation (16) at various friction coefficients ( $\mu = 0.02, 0.063, 0.1, 0.2$  and 0.3).

function of the friction coefficient is as follows:

$$\log(W_s) = 3.25(\mu) - 0.194,\tag{16}$$

where  $\mu$  is the friction coefficient. As for the effect of the bed height, the simulation results at  $u_{ms}$  show that the bed height does not significantly affect the particle circulation rate in the 2DSB with draft plates, which is consistent with Kalwar [21]. As expected, the particle circulation rate decreases as the friction coefficient increases. Figure 7 compares the simulated  $W_s$  to that predicted by correlation (16). An apparent friction coefficient of 0.063 gives a circulation rate consistent with the experimental value of 0.39 kg/s reported by Kalwar [21]. Obviously, the friction coefficient has a significant effect on the particle circulation rate in the 2DSB with draft plates.

### 4.5. Role of draft plates in the 2DSB

When the draft plates are removed from the vessel, our simulations show that spouting no longer occurs in the vessel at the bed height of 0.9 m (26 000 particles). A bubbling bed instead occurs in the vessel as shown in Fig. 8. Even as the gas velocity is further increased, the bubbling bed still persists. The spouting does not occur in the vessel because the particle size is quite large. Malek and Lu [24] found that the maximum spoutable bed depth decreased as the particle size increased. Figure 9 shows the observed flow patterns in the 2DSB at the bed height of 0.4 m (10 000 particles). Spouting does occur at this reduced bed height when the gas velocity sufficiently increases. The minimum spouting velocity and pressure drop are about 2.0 m/s and 1.75 kPa, respectively. As expected, the minimum spouting velocity and pressure drop of the 2DSB without draft plates are significantly higher than with draft plates. In conclusion, the draft plates cannot only reduce the

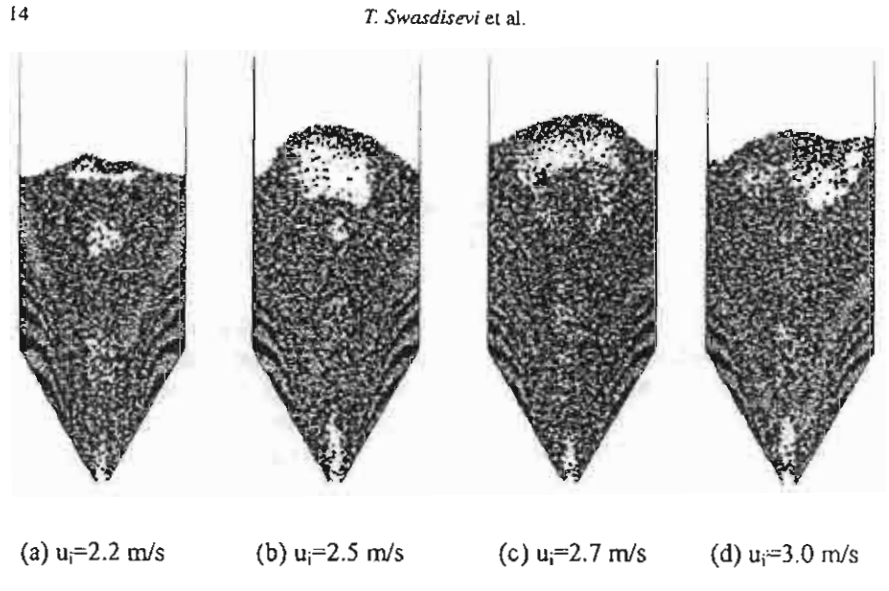


Figure 8. Snapshots of flow patterns in 2DSBs at the bed height of 0.9 m (26 000 particles). This figure is published in colour on http://www.ingenta.com

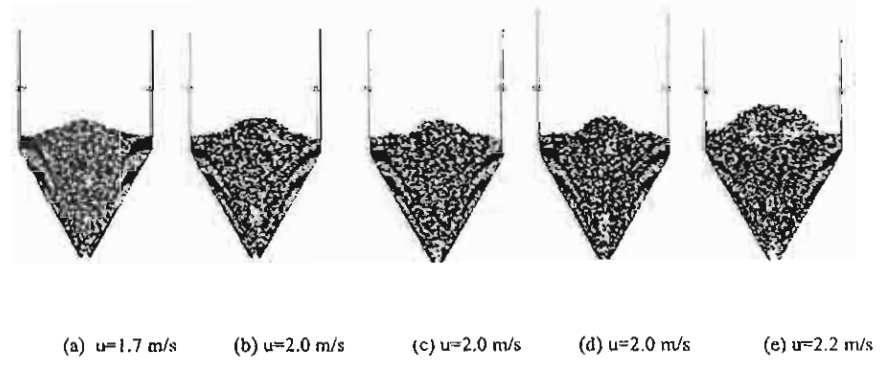


Figure 9. Snapshots of flow patterns in the 2DSBs at the bed height of 0.4 m (10 000 particles). This figure is published in colour on http://www.ingenta.com

minimum spouting velocity and pressure drop, but also increase the spoutable bed height.

### 4.6. Degree of mixing in the 2DSB

The degree of particle mixing in a 2DSB without draft plates is also investigated in this work. The degree of mixing indicates how good the mixing of particles is in the system. The formulas used for calculating the degree of mixing (M) are as

Prediction of gas-particle dynamics

15

follows [25]:

$$M = 1 - \frac{\sigma_{\rm p}}{\sigma_{\rm o}}, \qquad (17)$$

$$\sigma_{\rm p}^2 = \frac{\sum (x_{\rm i} - \bar{x}_{\rm c}^2)}{N}, \qquad (18)$$

$$\sigma_{\rm p}^2 = \frac{\sum (x_{\rm i} - \bar{x}_{\rm c}^2)}{N},$$
 (18)

$$\sigma_{\rm o}^2 = \bar{x}_{\rm c}(1 - \bar{x}_{\rm c}),$$
 (19)

where  $\bar{x}_c$  is the theoretical average number of particles in a sampling cell,  $x_i$  is the observed number of particles in each sampling cell, N is the number of the sampling cells,  $\sigma_0^2$  is the sample variance of the number of particles in the sampling cells,  $\sigma_0^2$ is the theoretical variance in the case of complete segregation, and M is zero and unity in the case of complete segregation and random mixing, respectively. The relation between M and elapsed time for various superficial gas velocities at 26 000 and 10000 particles is shown in Fig. 10 (Rochana and Pinyopotjanard, private communication, 2003). In Fig. 10a, M initially oscillates up to 2 s. Subsequently, M reaches 0.5-0.6 (poor mixing) at velocity of 2.2 and 2.5 m/s. At a velocity of 2.7 and 3.0 m/s, M gradually increases with time. It means that these velocities are high enough for mixing. In Fig. 10b, M initially oscillates at 0-2 s after which its value becomes steady at 0.9-1 (good mixing) for all velocities. As expected, the mixing in a 2DSB with 10 000 particles is better than that with 26 000 particles.

### 4.7. Effect of gas-to-particle heat transfer in the 2DSB with draft plates

When hot air is injected into the bottom of the spouted bed, gas-to-particle heat transfer occurs in the spouted bed. The additional effect of gas-to-particle heat transfer is also investigated here. Figure 11 shows the temperature profiles of the particles and air in the spouted bed with draft plates at various times. It is found that the average particle temperature in the spout region is higher than that in the downcomer region. The particles are heated for a short time in the spout region. The particle temperature adjacent to the slant base is lower than the other regions because the friction between the particles and the slanted base decreases the return flow of the particles to the spout region. Similarly, the air temperature in the spout region is higher than that in the downcomer region. The air temperature gradually increases with time. Figure 12 shows the profiles of the gas-to-particle heat transfer coefficient and Reynolds number over the dimensionless height  $(z/R_d)$ 16.927-22.454 (above the slanted base) in the spout and downcomer region at 150°C. The average Reynolds number in the spout and downcomer are 5690 and 130, respectively. As a result, the heat transfer coefficient in the spout region is significantly higher than that in downcomer region. In the spout region, the heat transfer coefficient decreases against the increased height. The heat transfer coefficient near the draft plates is lower than that near the central axis because the number of particles near the draft plate is more concentrated and the local gas velocity is slower than elsewhere. Therefore, the particles near the draft plates will

v=2.7 m/s

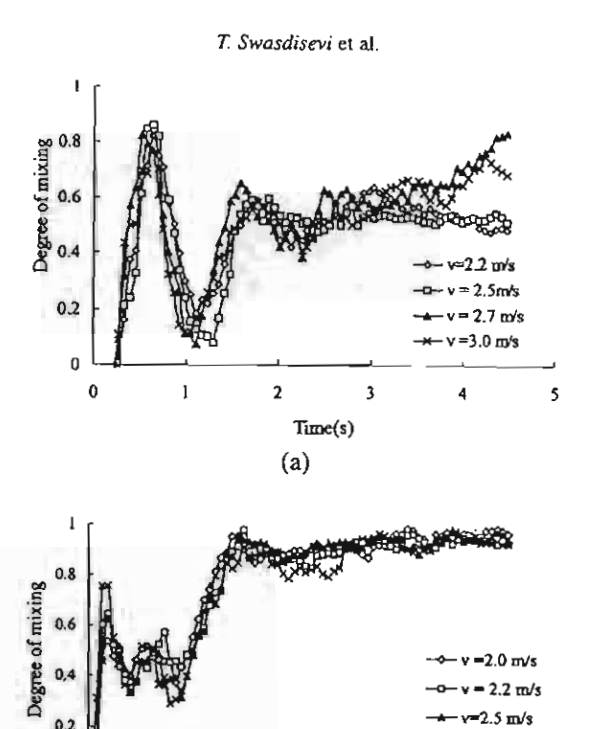


Figure 10. Relation between the degree of mixing and fluidization time for various superficial gas velocities at (a) 26 000 and (b) 10 000 particles.

Time (s) (b) 3

have contact to gas. In the downcomer region, the heat transfer coefficient is rather uniform. The heat transfer coefficient near the draft plate and the wall is slightly higher than elsewhere. It may be the result of the channeling effect at these regions. Our simulation reveals that the gas-to-particle heat transfer occurs mainly in the central or spout region, as reported previously by Freitas and Freire [26].

### 5. CONCLUSIONS

The aerodynamics of particles and fluid flow in the 2DSB with draft plates has been investigated in detail with the aid of the DEM. The validity of the method in the absence of heat transfer has been confirmed with the published experimental data of Kudra [3] and Kalwar [21]. Our results reveal that some slug flow still occurs in the spout at the minimum spouting velocity. This is the reason why the time-smoothed particle velocity decreases in the spout region as the height

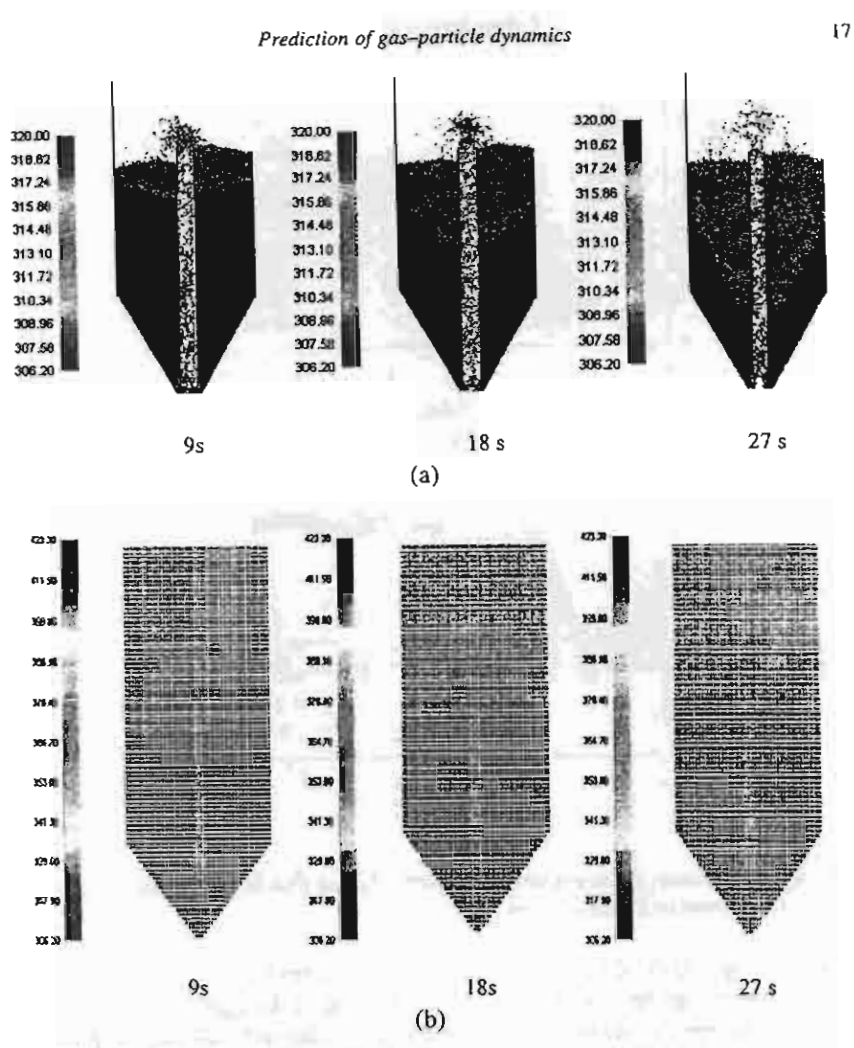
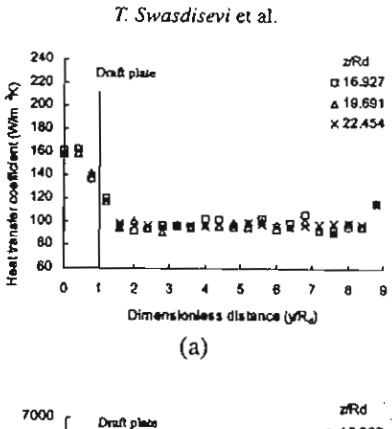


Figure 11. (a) Particle temperature and (b) air temperature distributions in the 2DSB with draft plates at 2 m/s and 150°C. This figure is published in colour on http://www.ingenta.com

increases. The slugs gradually disappear when the gas velocity is further increased. In the downcomer region, the downward particle velocities near the draft plates are found to decrease as the height increases, whereas the velocities near the walls increase with the increasing height. The particle circulation rate decreases when the coefficient of friction increases. The calculated particle circulation rate shows good agreement with the experimental value of Kalwar [21] when the friction coefficient is sufficiently small at 0.063. The installation of the draft plates in the 2DSB not only reduces the minimum spouting velocity and pressure drop, but also increases the maximum spoutable bed height. The mixing in the 2DSB with 10000 particles





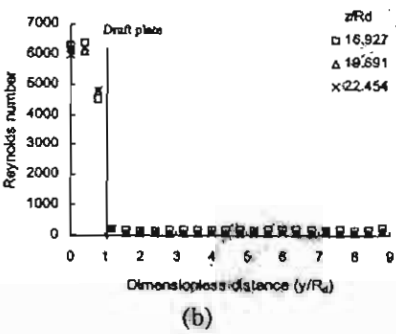


Figure 12. Profile of (a) the height-averaged heat transfer coefficient and (b) Reynolds number over the dimensionless height  $(z/R_d)$  16.927–22.454 in the spout and downcomer at 150°C and 2.0 m/s.

is significantly better than that with 26 000 particles. The heat transfer coefficient decreases against the increased height in the spout region, but it is rather uniform in the downcomer region. The gas-to-particle heat transfer occurs mainly in the central or spout region.

### Acknowledgements

T. S. is grateful to the Thailand Research Fund (TRF) for its Royal Golden Jubilee PhD Scholarship and to the Association of International Education Japan (AIEJ) for its 1-year student exchange fellowship to do research in Osaka University. W. T. and T. C. are grateful to the TRF for financial support from its Team Research Promotion Fund. W. T., T. C. and T. T. are grateful to Chulalongkorn University (TJTTP-JBIC Project) for supporting their short-term stays to carry out research collaboration between Osaka University and Chulalongkorn University.

### REFERENCES

 L. M. Passos, A. S. Mujumdar and G. S. V. Raghavan, Spouted beds for drying: principles and design consideration, in: Advances in Drying, pp. 359-397. Hemisphere, New York (1987).

- A. S. Mujumdar, Spouted bed technology a brief review, in: Drying'84, pp. 151-157. Hemisphere, New York (1984).
- T. Kudra, A. S. Mujumdar, G. S. V. Raghavan and M. I. Kalwar, Two-dimensional spouted beds: some hydrodynamic, heat transfer and drying characteristics, in: *Drying* '92, pp. 65-83 (1992).
- R. J. Rhodes, X. S. Wang, M. Nguyen, P. Stewart and K. Liffman, Onset of cohesive behavior in gas fluidized beds: a numerical study using DEM simulation, Chem. Engng Sci., 4433

  –4438
  (2001).
- Y. Tsuji, T. Tanaka and T. Ishida, Lagrangian numerical simulation of plug flow of cohesionless particles in a horizontal pipe, Powder Technol. 71, 239-250 (1992).
- Y. Tsuji, T. Kawaguchi and T. Tanaka, Discrete particle simulation of two-dimensional fluidized bed. Powder Technol. 77, 79-87 (1993).
- T. Kawaguchi, T. Tanaka and Y. Tsuji, Numerical simulation of two-dimensional fluidized beds using the discrete element method (comparison between the two- and three-dimensional models), Powder Technol. 96, 129-138 (1998).
- T. Kawaguchi, M. Sakamoto, T. Tanaka and Y. Tsuji, Quasi-three-dimensional numerical simulation of spouted beds in cylinder, *Powder Technol.* 109, 3–12 (2000).
- Y. Kaneko, T. Shiojima and M. Horio, DEM simulation of fluidized beds for gas-phase olefin polymerization, Chem. Engng Sci. 54, 5809-5821 (1999).
- K. Kawagi, K. Takano and M. Horio, The effect of tangential lubrication by bridge liquid on the behavior of agglomerating fluidized beds, *Powder Technol.* 113, 287–298 (2000).
- D. Rong and M. Horio, Behavior of particles and bubbles around immersed tubes in a fluidized bed at high temperature and pressure: a DEM simulation, Int. J. Multiphase Flow 27, 89–105 (2001).
- K. Kuwagi and M. Horio, A numerical study on agglomerate formation in a fluidized bed of fine cohesive particles, Chem. Engng Sci. 57, 4737-4744 (2002).
- M. A. Van Nierop, G. Glover, A. L. Hinde and M. H. Moys, A discrete element method investigation of the charge motion and power draw of an experimental two-dimensional mill, Int. J. Miner. Process. 61, 77-92 (2001).
- T. Madiyanon, S. Soponronnarit and W. Tia, Industrial-scale prototype of continuous spouted bed paddy dryer, *Drying Technol.* 19, 207-216 (2001).
- T. Madiyanon, S. Soponronnarit and W. Tia, A two-region mathematical model for batch drying of grains in a two-dimensional spouted bed, *Drying Technol.* 19, 1045–1064 (2001).
- 16. S. Ergun, Fluid flow through packed columns, Chem. Engng Prog. 48 (1952).
- C. Y. Wen and Y. H. Yu, Mechanics of fluidization, Chem. Engng Prog. Sump. Ser. 62, 100 (1966).
- W. E. Ranz and Marshall, Friction and transfer coefficients for single particles and packed beds, Chem. Engng Prog. 48, 247-253 (1952).
- D. J. M. Sartori, J. T. Freire and G. Massarani, Transferencia de calor gas-grao em leito deslizante, in: Proc. 5th Natl Meet. on Drying, pp. 318-341, Lavras (1985).
- P. A. Cundall and O. D. L. Strack, A discrete numerical model for granular assemblies, Geotechnique 29, 47-65 (1979).
- M. I. Kalwar, Aerodynamics and drying characteristics of grains in two-dimensional spouted beds, PhD Thesis, McGill University (1991).
- 22. K. B. Mathur and N. Epstein, Spouted Beds. Academic Press, London (1974).
- G. Volpicelli, G. Raso and L. Massimilla, Gas and solid flow in bidimensional spouted beds. in: Proc. Eindhoven Fluidization Symp., Eindhoven, p. 123 (1967).
- 24. M. A. Malek and B. C. Y. Lu, Heat transfer in a spouted beds, Can. J. Chem. Engng 42 (1964).
- K. Gotoh, H. Masuda and K. Higashitani, Powder Technology Handbook, 2nd edu. Marcel Dekker, New York (1997).
- L. A. P. Freitas and J. T. Freire, Gas-to-particle heat transfer in a draft tube spouted bed with continuous solids feeding, in: Proc. 11th Int. Drying Symp., Greece, Vol. A, pp. 176-183 (1998).

50

51

52

53

54

55

56

57

58

59

61

62

63

64

65

66

67

68

69

70

71

72

73

74

75

76

77

78

79

80

81

82

83

84

85

86

87

88

89

90

91

92

93

94

95

### **Modeling of Experimental Treatment** of Acetaldehyde-Laden Air and **Phenol-Containing Water Using** Corona Discharge Technique

1

2

3

5

9

10

12

13

14

15

16

17

18

19

20

21

22

23

24

25

26

27

28

29

30

31

32

33

34

35

36

37

38

39

40

41

42

43

44

45

46

47

48

KAJORNSAK FAUNGNAWAKIJ, t." NORIAKI SANO. TAWATCHAL CHARLNPANITKUL, 'AND WIWUT TANTHAPANICHAKOON .. \$

Center of Excellence in Particle Technology, Department of Chemical Engineering, Chulalongkorn University, Patumwan, Bangkok 10330, Thailand, Department of Mechanical and System Engineering, University of Hyogo, 2167 Shosha, Himeji 671-2201, Japan, and National Nanotechnology Center, NSTDA, Thailand Science Park, Klong Luang, Phathumthani 12120, Thailand

Acetaldehyde-laden air and phenol-contaminated water were experimentally treated using corona discharge reactions and gas absorption in a single water-film column. Mathematical modeling of the combined treatment was developed in this work. Efficient removal of the gaseous acetaldehyde was achieved while the corona discharge reactions produced short-lived species such as 0 and 0as well as ozone. Direct contact of the radicals and ions with water was known to produce aqueous OH radical. which contributes to the decomposition of organic contaminants: phenol, absorbed acetaldehyde, and intermediate byproducts in the water. The influence of initial phenol concentration ranging from 15 to 50 mg L-1 and that of influent acetaldehyde ranging from 0 to 200 ppm were experimentally investigated and used to build the math model. The maximum energetic efficiency of TOC, phenol, and acetaldehyde were obtained at 25.6 × 10 -8 mol carbon J $^{-1}$ , 25.0  $\times$  10 $^{-9}$  mol phenol J $^{-1}$ , and 2.0  $\times$  10 $^{-9}$ mol acetaldehyde J-1, respectively. The predictions for the decomposition of acetaldehyde, phenol, and their intermediates were found to be in good agreement with the experimental results.

### Introduction

High-voltage electrical discharge is presently employed in various applications, for example carbon-nanomaterial synthesis (1), gas synthesis (2, 3), gas purification (4-10), and water purification (11-14). Focusing on gas purification, atmospheric electrical discharge technique has become a common method for high-efficiency purification of gaseous pollutants at trace concentrations. A number of the electrical discharge techniques such as dc corona discharge (4-7).

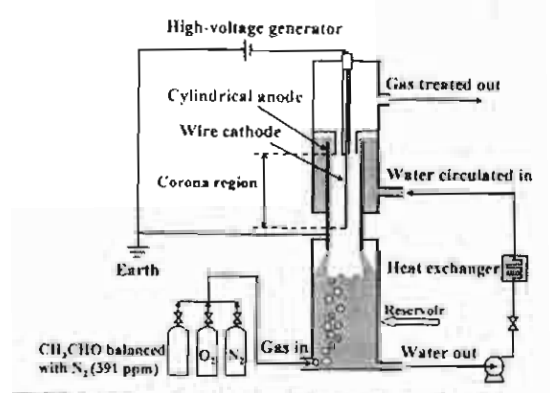


FIGURE 1. Schematic diagram of the experimental setup.

pulsed corona discharge (8, 9), and electron beam (10) have been widely developed. In the dc corona discharge technique, low energy electrons are utilized for the removal of the gaseous pollutants. The dc corona discharge is quite promising in terms of removal efficiency with relatively low byproduct formation. At present, several types of dc corona discharge reactors are available. One of them, the wettedwall corona discharge reactor, was proposed to enhance the removal efficiency by adding gas absorption effect to gasphase reactions (6). In this reactor, a thin falling liquid film flowing on the vertical anode surface simultaneously absorbs soluble gases and the negative ions produced by electron attachment, ionization, and dissociation of the target gases. In recent years, pulsed plasma discharge (11, 12) and dc corona discharge (13) have been developed for the treatment of aqueous organic compounds. The wetted-wall reactor was also applied to the purification of wastewater (14). In this method, the organic contaminants were effectively degraded by the OH radical along with ozone.

By combining the features of the wetted-wall reactor, we have proposed the present reactor for the simultaneous purification of gas and water (15). Gaseous contaminants were removed from the main gas stream by a combination of gas corona reactions and gas absorption. Simultaneous removal of aqueous contaminants was achieved by their decomposition with the OH radical produced by direct contact of gas corona species with water. With simultaneous purification, not only can the operating cost, the operation time, and the energy consumption be minimized, but the total investment cost for the equipment can also be reduced.

In this article, a kinetic model for simultaneous treatment of phenol-containing wastewater and acetaldehyde-laden air in a cylindrical wetted-wall corona-discharge reactor was developed. The influence of gaseous acetaldehyde inlet concentration and initial aqueous phenol concentration, as well as their major intermediate products, on the simultaneous treatment was investigated. Then, the simulation results were compared with the experimental ones. The developed model should be useful for scale-up of the system for practical application.

#### Experimental Section

The experimental apparatus is schematically shown in Figure 1. A high dc voltage of 8-13 kV with negative polarity was applied on a stainless steel (SUS) wire cathode (0.34 mm diameter) stretched along the center of a grounded SUS cylindrical anode (34 mm inner diameter; 200 mm length) to generate corona discharge. The length of the corona

<sup>\*</sup> Corresponding author phone: +66-2-564-6984; fax: +66-2-564-6985; e-mail: wiwiii@nanotec.or.th.

¹ Chulalongkorn University.

University of Hyogo.

<sup>§</sup> National Nanotechnology Center, NSTDA.

Present address: Japan Science and Technology Agency, Innovation Plaza Kyoto, 1-30 Ohara Goryo, Nishikyo-ku, Kyoto 615-

98

99

100

101

102

103

104

105

106

107

108

109

110

111

112

113

114

115

116

117

118

119

120 121

122

123

124

125

126

127

128

129 130

131

132

133

134

135

136

137

138

TABLE 1. Gas Coron	na Reaction and Decomposition of Organic Species in Aqueo	us Phase	
equation	reaction	(L mol 1 s 1)	ref.
1	$O_2 + e^{-1} \rightarrow O + O + e^{-1}$		16, 17
2	$O_2 + e^{-1} - O^- + O$		16, 18
3	$O_2 + O - O_3$		16
4	$O_{(aq)} + H_2O_{(aq)} \rightarrow 2OH_{(aq)}$		11, 13, 20
5	$O^{-1}_{(aq)} + H_2O_{(aq)} \rightarrow OH_{(aq)} + OH_{(aq)}$		20
6	acetaldehyde $+$ OH $\xrightarrow{k_1}$ acetic acid	5 × 109	parameter estimation
7	acetaldehyde + OH - unidentified product (UPc1)	$4 \times 10^9$	parameter estimation
8	acetic acid + OH + CO <sub>2</sub> + H <sub>2</sub> O	5 · 10 <sup>9</sup>	parameter estimation
9	$UP_{AD} + OH \xrightarrow{k_4} CO_2 + H_2O$	$8 \times 10^{9}$	parameter estimation
10	phenol + OH + catechol	$7 \times 10^{9}$	28
11	phenol + OH + hydroquinone	$6.5 \times 10^9$	22
12	phenol + OH resorcinol	$1 \times 10^9$	22
13	phenol + OH - unidentified product (UP <sub>C6</sub> )	1 × 109	parameter estimation
14	catechol + OH - UP <sub>CB</sub>	1.1 × 10 <sup>10</sup>	29
15	hydroquinone + OH - UP <sub>CG</sub>	1 × 1011	22
16	resorcinol + OH - UP <sub>C6</sub>	1 × 10 <sup>10</sup>	30
17	$UP_{C6} + OH \xrightarrow{k_{12}}$ acetic acid	1 × 10 <sup>10</sup>	parameter estimation

discharge region was fixed at 140 mm throughout the experiments. The desired gas mixture of acetaldehyde, Oz. and Nz was prepared by mixing commercial standard gases. The gas mixture at the flow rate of 100 mL min-1 at 25 °C, 101.3 kPa, was continuously supplied to the reactor by bubbling into a water reservoir at the bottom of the reactor column. Aqueous phenol solution (1 I. in volume) was supplied to the reactor as a thin falling film on the inner wall of the anode through the corona reaction zone, and was circulated at a flow rate of 1.4 L min 1. The average water film thickness in the absence of corona discharge was calculated as 0.4 mm. The temperature of the water phase was controlled at 10 °C by passing it through a heat exchanger unit.

For gas analysis, the effluent stream was periodically sampled and analyzed using an FID gas chromatograph (Shimadzu, GC-9A; Column, Porapak Q). Ozone produced under corona discharge condition was measured by the iodometric method. Meantime, potential byproducts such as NO, and CO were measured with gas detector tubes (GASTEC.Co., Ltd. and Kitagawa Co., Ltd.). For water analysis, a high performance liquid chromatograph (HPLC) with a UV-Vis detector (Shimadzu, SPD-10AVP) and the abovementioned FID-GC were used for analyses of phenol, acetaldehyde, and intermediate products in the circulating water. In the HPLC analysis, an adsorption column, Devolosil (Nomura chemical,  $\phi$  4.6 mm × 50 mm), was operated at a fixed temperature of 20 °C. The UV-Vis detector was set at a wavelength of 277 nm. The carrier liquid was 0.1% aqueous phosphoric acid mixed with acctonitrile (2%). Total organic carbon (TOC) and pH of the circulating water were monitored by a TOC analyzer (Shimadzu, TOC-5000) and a pH meter (Horiba, pH meter F-22), respectively.

Development of Mathematical Model. To set up the model, a clear overall conception of the relevant mass transfer phenomena and reaction pathways of the target compounds in the present system was indispensable. The reactions of concern in the present corona discharge system are shown in Table 1. Figure 2a shows a simplified concept of the relevant mass transfer phenomena and the formation of aqueous OH radical via direct contact with gas corona discharge. Corona discharge is generated by applying a high dc voltage onto the wire cathode with negative polarity. Consequently,

energetic electrons are emitted from the wire cathode and accelerated toward the anode along the electric field. During their drift, dissociation and ionization of oxygen can produce O radical in the high strength electric field adjacent to the cathode as shown in eq 1 (16, 17). In the adjacent low strength electric field next to the high strength zone, dissociative electron attachment to oxygen can also produce O and O via eq 2 (16, 18). Reaction of oxygen with the O radical would produce ozone via eq 3. It should be noted that  $O_2^+$ ,  $O_3^-$ , and some ions can also be produced by corona discharge reactions. However, among those ions, O" is considered to be the dominant species in the dc corona discharge (19).

139

140

141

142

143

144

145

146

147

148

149

150

151

152

153

154

155

156

157

158

When O and O reach the interfacial water and dissolve into it, they subsequently react with water molecules to produce reactive OH radical in water as described in eqs 4 and 5 (11, 13, 20). In addition, OH, H2O2, and some related radicals can also be produced in the gas corona zone since water vapor is present in the gas phase. These gaseous species along with ozone would also transfer into the water. It should be noted that the OH radical can be generated by radiolysis

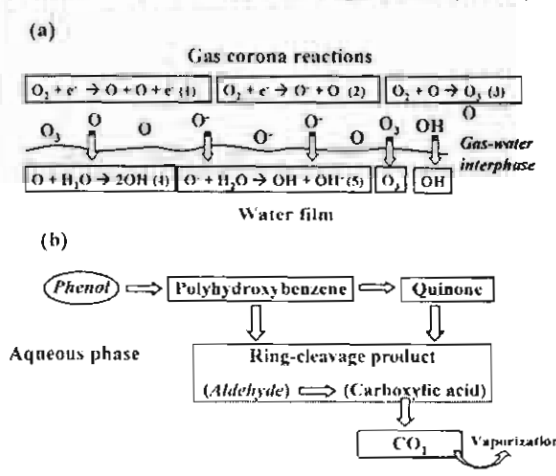


FIGURE 2. (a) Concept of mass transfer phenomena and formation of OH radical in water, and (b) reaction pathway of phenol and acetaldehyde in aqueous phase under corona discharge treatment.

in the pulsed corona discharge (10, 21) and in the pulseless corona discharge (22). In these works, the corona was directly generated in water by submerged corona spot. However, according to our previous report (23), aqueous acetaldehyde could not be decomposed in the present reactor under corona discharge in the absence of oxygen. This indicated that production of OH by radiolysis in the present reactor was negligible.

When the gas stream was bubbled through the phenol solution, acetaldehyde was absorbed into the phenol contaminated solution. As a result, aqueous solution containing phenol and acetaldehyde flowed through the corona zone as a falling thin film on the inner surface of the anodic cylinder. In the corona zone, ions and radicals produced by gas corona were continuously supplied to the solution to form the hydroxyl radical. Meanwhile, organic compounds in water were continuously decomposed. If a small quantity of gaseous acetaldehyde remained in the gas stream, it was expected to be completely removed in the gaseous corona zone by radical reactions (24, 25), ozonation, and cluster formation (24).

Decomposition pathways of phenol by oxidation processes such as radiolysis (10, 21, 22), oxidation by hydroxyl (11-13) and by ozonation, and ultrasonic irradiation (26) have been reported. On the basis of these studies, Figure 2b shows that phenol was first oxidized to polyhydroxybenzenes and subsequently to quinones. Both of them proceeded to yield ring-cleavage products, i.e., aldehydes and carboxylic acid groups. Finally, carboxylic acids, such as formic and acetic acids, were converted to carbon dioxide. As for the decomposition pathway of aqueous acetaldehyde, it was reported that aqueous acetaldehyde was mainly decomposed to acetic acid before being unineralized to carbon dioxide by the oxidation process (6, 27).

On the basis of the decomposition pathways mentioned in the previous section, the overall reaction scheme was proposed as described in eqs 6-17. The assumptions used in developing the model are as follows:

(1) With rate constants of orders of 101 L mol 1 s-1 or higher, OH radical was considered as the dominant species for the decomposition of aqueous organic compounds. In comparison, the reaction rates of phenol and acetaldehyde with ozone were considered to be negligible with rate constants of orders of 103 L mol-1 s-1 and 1.5 L mol-1 s-1, respectively (31, 32). During corona discharge operation, ozone was detected at a maximum ca. 2000 ppm in the process studied here. To evaluate the contribution of ozone, separate treatment of acetaldehyde and phenol was conducted by feeding 2000 ppm ozone in the influent gas stream. It was found that aqueous acetaldehyde was scarcely decomposed by ozone, whereas phenol decomposition by ozone was about 2-3 times slower than that by corona discharge induced species. In addition, TOC was ineffectively decomposed by ozone under the conditions studied (7, 15).

(2) A first-order reaction with respect to each of the two species in eqs 6-17 was assumed in the model.

(3) Unidentified intermediate products from the decomposition of acetaldehyde, UP<sub>Cl</sub>, and from that of phenol, UP<sub>Cl</sub>, were assumed to be  $C_1$  and  $C_6$  compounds, respectively.

(4) The reactor was assumed to be isothermal and well-mixed since the decomposition of phenol and acetaldehyde was considered to fully take place in the reservoir under the corona discharge zone. Gas bubbling and water film falling down the anode made the reservoir behave like a well-mixed reactor. The water volume in the reservoir constituted approximately 60% of the total volume of the solution.

(5) We have experimentally checked the equilibrium concentration of acetaldehyde as shown in the Supporting Information. At equilibrium, more than 95% of acetaldehyde could be absorbed into the water under the present condition. In fact, the effluent concentration of gaseous acetaldehyde

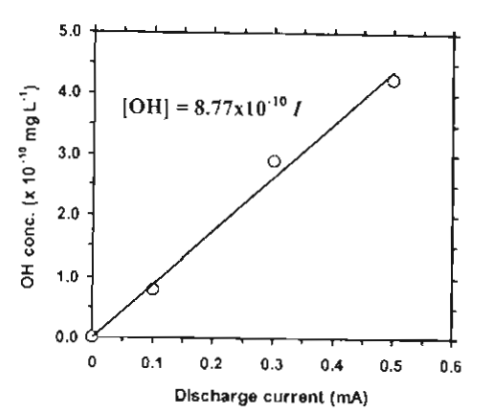


FIGURE 3. OH concentrations determined by model fitting with experimental results for various corona discharge currents.

was found to be lower than the detection limit in all experiments of the simultaneous treatment. Consequently, though gaseous acetaldehyde could be removed in both gas and liquid phases, only the liquid phase needed to be considered in the present model.

(6) The volume of the solution circulated in the system was constant.

(7) The concentration of the reactive OH radical was assumed to reach some pseudo-steady state as determined from experimental data. This pseudo-steady-state assumption has been adopted for the simulation of phenol decomposition in the radiolysis process (11, 21, 22).

In any case, vaporization of phenol during the operation was negligible. Taking molar material balances of the reactive species in the liquid phase, we obtained a set of 8 linear ordinary differential equations as shown in Table 2. The set

#### TABLE 2. Molar Species Material Balance in Aqueous Phase

```
d[AD]/dt
                      q_gC_{s-g} infW - (k_1+k_2)[AD][OH]
d[UPc1]/dt
                      k_2[AD][OH] - k_4[UP_{C1}][OH]
                      k_1[AD][OH] + k_{12}[UP_{C6}][OH] - k_3[AA][OH]
d[AA]/dt
d(PHI/dt
                =
                      (k_5 + k_6 + k_7 + k_8)[PH][OH]
                      k_{5}[PH][OH] - k_{9}[CC][OH]
k_{6}[PH][OH] - k_{10}[HQ][OH]
d(CCI/dt
                =
d(HO)/dt
                300
                      k_7[PH][OH] - k_{11}[RC][OH]
dIRCVdt.
                      k_{8}(PH)[OH) + k_{9}(CC)[OH) + k_{10}[HQ](OH)
d[UPcsl/dt
                      + k11(RC)[OH) - k12[UPc6][OH]
```

of equations was numerically integrated using the fourth-order Runge—Kutta method. The rate constants involved in the reactions were obtained through the literature except for  $k_1$ ,  $k_2$ ,  $k_3$ ,  $k_4$ ,  $k_6$ , and  $k_{12}$  which were estimated directly from the experimental data through curve-fitting. [OH],  $k_1$ ,  $k_2$ ,  $k_3$ ,  $k_4$ ,  $k_6$ , and  $k_{12}$  were determined by rationally varying their values until the simulation and experimental results were fitted according to the applied treatment conditions. In this way, OH, the rate constants, and all measured compounds indicated in eqs 6–17 were calculated. As shown in eqs 1, 2, 4, and 5, it was considered that aqueous [OH] concentration was determined by corona discharge conditions, i.e., the corona current I. A correlation between I and [OH] was obtained and is presented in the next section.

### Results and Discussion

Simulated OH Concentration and Estimation of Reaction Rate Constants. In Figure 3, the aqueous concentration of OH radical (mg L<sup>-1</sup>) was determined by model fitting with the experimental data as a linear function of the corona current (I, mA) as  $[OH] = 8.77 \times 10^{-10}I$  in the range of 0.1-0.5 mA. When the corona current increased, the number of

energetic electrons would follow suit. More electrons naturally yielded more radicals and ions in the gaseous corona reactions. As a result, production of aqueous OH radicals should be accelerated. Under the condition studied here, any effect of interfacial surface roughness of water film on OH production was insignificant.

As indicated in Table 1, the values of k1, k2, k3, k4, k8, and ky could not be found in the literature and had to be determined from the experimental results via curve-fitting.  $k_1$  and  $k_2$  were estimated as  $5 \times 10^9$  and  $4 \times 10^9$  L mol  $^{-1}$  s respectively. These rate constants have the same order of magnitude as the reaction rate of aldehyde group toward OH reported as  $1 \times 10^9$  L mol<sup>-1</sup> s<sup>-1</sup> (31). The rate constants of acetic acid,  $k_3$ , and unidentified product,  $k_4$ , were of the same order of magnitude at 5 × 109 and 8 × 109 L mol 1 s-1, respectively. With these reaction rate values and the assumption that UP was C1 compounds, formic acid and formaldehyde appeared to be the plausible species in the corona process. As previously reported, formaldehyde was slightly detected during acetaldehyde removal under corona discharge process (4). Decomposition of phenol to UPcs by the reaction with OH has a reaction rate of 1 × 109 L mols 1. This rate constant was consistent with those of phenol decomposition to polyhydroxybenzene and quinone groups with a 10° order of magnitude. It was reported that C6 compounds such as 1,4 benzoquinone, pyrogallol, and 1,2,4 benzenetriol were produced by reaction of OH radical with catechol, hydroquinone, or resorcinol (15, 21). Here k12 was determined as 1 × 1010 L mol-1 s-

A sensitivity analysis of the six parameters.  $k_1$ .  $k_2$ .  $k_3$ .  $k_4$ .  $k_8$ , and  $k_{12}$ , was conducted via simulation as shown in the Supporting Information. Each parameter was changed by  $\pm 10\%$  to determine the sensitivity. As it turned out, ca.  $\pm 6\%$  deviation in phenol concentration was observed when  $k_3$  was changed. Deviation of acetaldehyde at ca.  $\pm 5-6$  and  $\pm 4-4.5$  were affected by  $k_1$  and  $k_2$ , respectively.  $k_3$  had the highest effect on the acetic acid at -13% deviation whereas  $k_1$ .  $k_2$ ,  $k_4$ .  $k_3$ , and  $k_{12}$  contributed to less than 2% in deviation.  $k_4$  was found to be sensitive to TOC at maximum at ca. -5%. and the order of sensitivity with respect to the TOC was as follows:  $k_4 \geq k_3 \geq k_1 \geq k_2 \geq k_{12} \geq k_3$ .

Validation of Model at Various Corona Currents. Figure 4 shows the concentrations of (a) aqueous phenol and (b) TOC during simultaneous treatment at different corona discharge currents. I. Influent concentration of gaseous acetaldehyde,  $C_{n-q \ mf}$ , and initial concentration of phenol,  $C_{p-t \ mf}$ , were set at 15 ppm and 30 mg L  $^1$ , respectively. Increase of corona current results in an increase of phenol and TOC decomposition rate. Degradation rate of TOC was relatively slow compared with that of phenol. This is because TOC contained some stable intermediates as explained above. It should be noted that under this low concentration of influent acetaldehyde, its effluent concentration was reduced to zero during the process. As clearly seen in Figure 4, the simulation results showed good agreement with the experimental ones.

Validation of Model at Various Influent Acetaldehyde Concentrations. Figure 5 shows the concentrations of (a) aqueous phenol, (b) aqueous acetaldehyde, and (c) TOC during simultaneous treatment at various influent concentrations of gaseous acetaldehyde ranging from 0 to 200 ppm for a fixed initial concentration of phenol at 30 mg L<sup>-1</sup>. In Figure 5a, the experimental results showed that the aqueous concentrations of phenol rapidly decreased toward zero within around 3 h when  $C_{a-g\ inf}$  ranged from 0 to 200 ppm. Obviously acetaldehyde in this range did not affect the degradation rates of phenol. As for the concentration of aqueous acetaldehyde, Figure 5b shows that it initially increased in the early stage for all runs. Subsequently, aqueous acetaldehyde gradually decreased. A higher  $C_{a-g\ inf}$ 

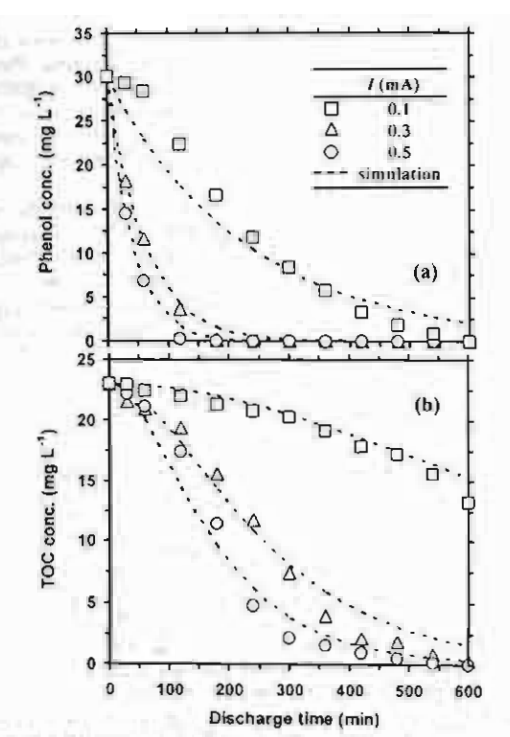


FIGURE 4. Time course of predicted and experimental concentrations for various corona currents. Concentrations of (a) aqueous phenol and (b) TOC;  $C_{p-1\;lal}=30\;$  mg L<sup>-1</sup>,  $C_{n-p\;lal}=15\;$  ppm.

3.39

3:17

logically resulted in a higher residual acetaldehyde concentration. As shown in Figure 5c, the time course of TOC concentration revealed that TOC can efficiently be degraded when the influent concentration of acetaldehyde was 30 ppm. Influent concentrations of 100 ppm or higher obviously inhibited the TOC degradation rate. Figure 5 shows that the mathematical model and the experimental data agreed fairly well at various influent acetaldehyde concentrations.

Validation of Model at Various Initial Phenol Concentrations. Figure 6 shows the concentrations of (a) aqueous phenol and (b) TOC during simultaneous treatment at various initial concentrations of phenol ranging from 15 to 50 mg L | for a fixed influent acetaldehyde concentration of 30 ppm. Aqueous phenol rapidly decreased toward zero for all cases. while the concentration of aqueous acetaldehyde (not shown here) remained essentially at zero throughout the operation. TOC degradation was much slower than phenol degradation. After ca. 8 h, TOC reached a similar concentration of around 4-5 mg  $L^{-1}$ . Then its value remained essentially constant. This means that TOC generation rate equals TOC decomposition rate. At this stage, it was considered that generation of TOC was solely from influent acetaldehyde and its intermediates. Though the simulation results provided a good fit to the experimental ones, it should be pointed out that when the initial concentration of phenol was as high as 50 mg L. 1, the predicted phenol and TOC decomposition rates were slightly underestimated. This is because, at a higher concentration of phenol, decomposition by ozonation could become more significant, thereby resulting in a faster decomposition rate

Validation of Model Against the Observed Intermediate Products. The predicted and experimentally observed concentrations of intermediate aqueous products are compared in Figure 7. The representative condition here was at  $C_{n-g}$  inf = 30 ppm,  $C_{p-l}$  ini = 15 mg L<sup>-1</sup>, and I = 0.3 m $\Lambda$ . Hydroquinone, catechol, and resorcinol were detected as primary intermediate products which were completely mineralized after about

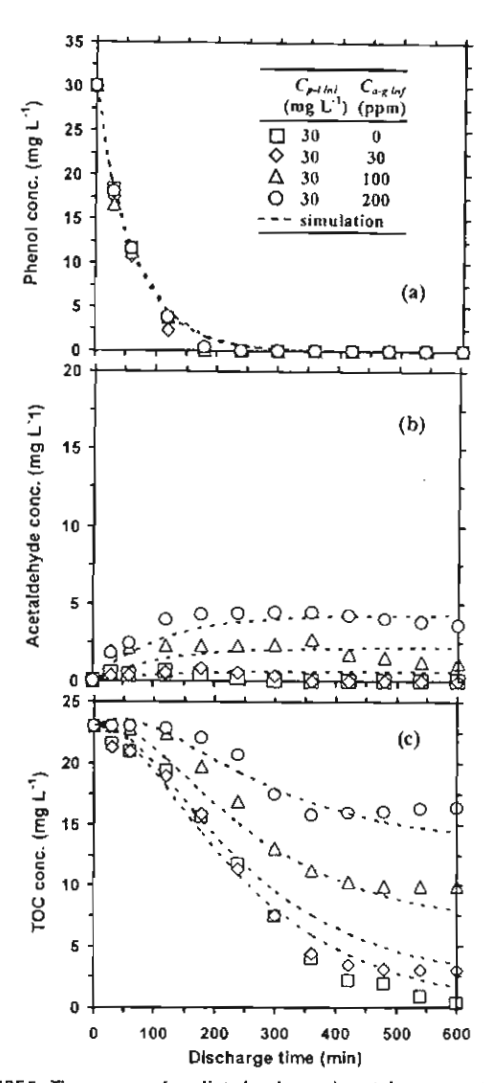


FIGURE 5. Time course of predicted and experimental concentrations for various influent acetaldehyde concentrations and a fixed initial phenol concentration. Concentrations of (a) aqueous phenol, (b) aqueous acetaldehyde, and (c) TOC;  $C_{s-g\ int}=0-200\ \mathrm{ppm}$ ,  $C_{p-l\ int}=30\ \mathrm{mg\ L^{-1}}$ ,  $l=0.3\ \mathrm{mA}$ .

374

376

376

377

378

379

380

381 382

383

384

385 386

387

388

389

390

391

392

300 min. Among these intermediates, catechol was a major species, whereas hydroquinone and resorcinol were minor. The simulated concentration of these intermediates showed good agreement with the experimental ones. After ca. 7 h of treatment, acetic acid occupied approximately 75% of the TOC. Therefore acetic acid was considered as the major stable intermediate product. Concentrations of acetic acid at 10 h operation under various Co-1 ini/Ca-g inj ratios and corona currents are depicted in Figure 8. Increase of Cp-1 Inil Ca g and from 15/30 to 50/30 resulted in more residual acetic acid. This means that a longer time is needed for the treatment process to reach a stable concentration of acetic acid. corresponding to the stable TOC concentration. However, acetic acid decomposition rate could be significantly enhanced by increasing the corona current. As clearly seen from the case of  $C_{p-1\,im}/C_{a-g\,inf}=30/30$ , increasing corona current from 0.1 to 0.5 mA could obviously decrease acetic acid from ca. 7 to 1 mg L-1. The predicted acetic acid concentration also fitted well with the experimental

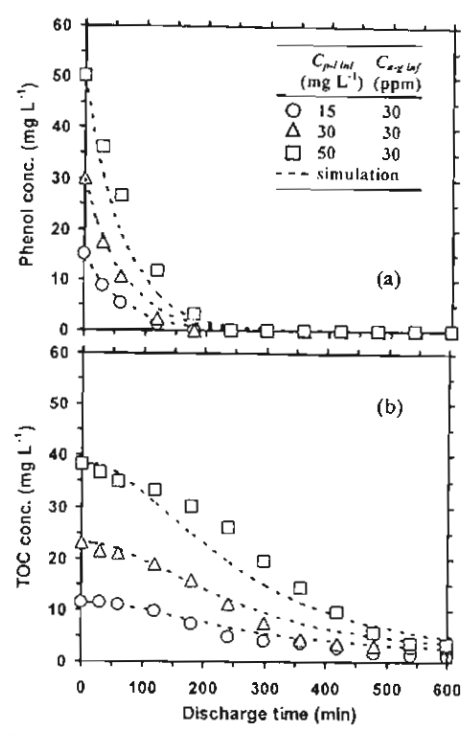


FIGURE 6. Time course of predicted and experimental concentrations for various initial phenol concentrations and a fixed influent acetaldehyde concentration. Concentrations of (a) aqueous phenol and (b) TOC;  $C_{p-1 \ ini} = 15-50 \ \text{mg L}^{-1}$ ,  $C_{s-q \ ini} = 30 \ \text{ppm}$ ,  $I = 0.3 \ \text{mA}$ .

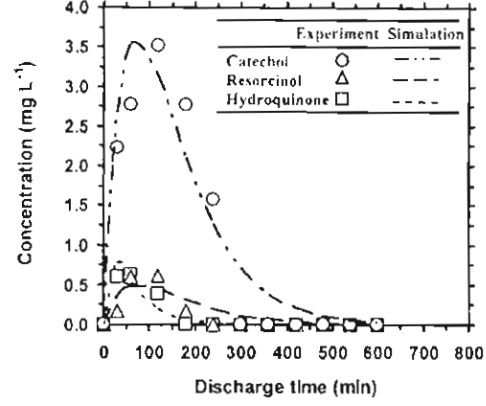


FIGURE 7. Time course of predicted and experimental concentrations of primary intermediates, hydroquinone, resorcinol, and catechol for  $C_{p-l\ lnl}=15$  mg L<sup>-1</sup>,  $C_{p-p\ lnl}=30$  ppm, I=0.3 mA.

Energetic efficiency of TOC degradation  $J_{TOC}$  by the present technique was calculated to evaluate the system from the viewpoint of energy yield. 393

394

395

396

397

398

399

400

401

$$J_{TOC} = \frac{(W(C_{p-1 \, lm}/1000)R_{c-p} + q_g)}{(C_{a-g \, lm} - C_{a-g \, eff})10^{-6} m_a R_{c-a} t_{1/2})/2m_c}{IV t_{1/2}}$$
(18)

where W,  $C_{p-1 inn}$ ,  $C_{a-p inf}$ ,  $C_{a-p inf}$ ,  $C_{n-p}$ ,  $R_{c-n}$ ,  $t_{1/2}$ ,  $q_g$ ,  $m_c$ ,  $m_{ni}$  and  $m_p$  are, respectively, water volume, initial phenol concentration, influent acetaldehyde concentration, effluent acetaldehyde concentration, weight ratio of carbon in phenol, weight ratio of carbon in acetaldehyde, the period for which TOC under corona discharge is degraded by half of that

403

404

405

406

407

408

409

410

411

412

413

414

415

416

417

418

419

420

421

422 423

424

425

426

427 428

429

430

431

432

433

434

435

436

437

438 439

440

441

442

443

444

445

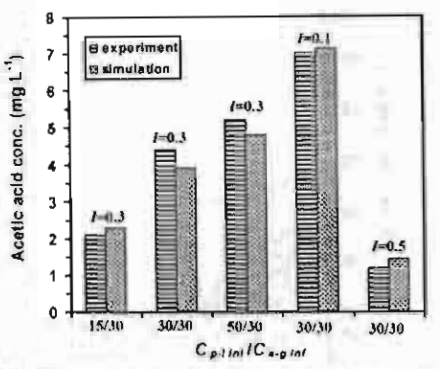


FIGURE 8. Predicted and experimental concentrations of stable byproduct, acetic acid, at 10 h operation. I = 0.1-0.5 mA.

without corona discharge, molar flow rate of feed gas, atomic mass of carbon, molecular mass of acetaldehyde, and that of phenol. Equation 18 was transformed to eas 19 and 20 for the determination of energetic efficiency of phenol Je and acetaldehyde JA, respectively.

$$J_p = \frac{W(C_{p-1\,ini}/1000)/2m_p}{IVt_{1/2}} \tag{19}$$

$$J_{A} = \frac{q_{g}(C_{a-g} \inf_{inf} - C_{a-g} \inf_{eg})10^{-6}}{IV}$$
 (20)

Here ITOC, IP, and IA respectively represent the average moles of carbon, phenol, and acctaldehyde degraded by unit energy. The maximum  $J_{RX}$ ,  $J_{Pi}$  and  $J_A$  obtained by the present technique were found as 25.6  $\times$  10<sup>-9</sup> mol carbon J  $^{-1}$ , 25.0  $\times$ 10 mol phenol J-1, and 2.0 x 10 mol acetaldehyde J-1, respectively. More detailed results of the energetic efficiency are shown in the Supporting Information. As comparison, phenol degradation using hybrid electrical discharge and single-liquid-phase electrical discharge were reported with energy yield of 0.89  $\times$  10<sup>-9</sup> mol phenol J<sup>-1</sup> and 0.30  $\times$  10<sup>-9</sup> mol phenol ]-1, respectively (33). As for other advanced oxidation processes, an energetic efficiency of 0.3 x 10-9 to 0.6 × 10 mol phenol J was reported for the system of UV-photolysis (34) and ultrasound (35). Anyway it should be noted that differences in experimental conditions of the treatment systems could significantly influence their performance

During the corona discharge operation, pH of water decreased from ca. 5.5-6 to ca. 3.5-4 within 3 h. After that, the pH of water gradually increased to ca. 4-4.5 and then remained essentially constant. It should be noted that the final value and decreasing rate of pH depended on the applied corona current. The observed results of pH change are shown in the Supporting Information.

As for gaseous byproduct analysis, NO., CO, and other potential hydrocarbon species generated in the corona discharge were not detected during the whole operation. It may be inferred that all acetaldehyde was rapidly absorbed into the water during gas bubbling, and gas-phase reaction of acetaldehyde could be neglected. Even if a small amount of undissolved acetaldehyde happened to remain in the gas phase, it would be removed by gas corona reaction. In-situ absorption of gaseous byproducts produced by the gas corona reaction contributed to their removal from gas stream.

Though the simulation results show good agreement with all experimental ones, it should be pointed out that ozone and peroxide, which partially contribute to the decomposition of aqueous organic compounds, have been omitted to simplify the present model. In future extension of the model, gas corona reactions and mass transfer of gas corona species between the gas and water phases along with contributions of O3, H2O2, and OH should be included in the model to determine the concentration of the OH radical as well as other short-lived species in water. It should be noted that production of OH radical strongly depends on experimental conditions such as corona current, dimension of the reactor. concentration of oxygen at the inlet, and water circulation rate.

446

447

448

449

450

451

452

453 454

455

456

457

458

459

460

461

462

463

464

465

466

467

468

4659

470

471 472

473

474

475

476

477

478

479

480

481

182

483

484

485

486

487

488

489

490

491

492

493

494

495

496

497

498

499

500

### Acknowledgments

Financial support from the Thailand Research Fund (Grant PHID/0180/2543 of Royal Golden Jubilee Ph.D. Program (TRF-RGJ) for K.F. and W.T., and Research Team Award (TRF RTA) for W.T. and T.C.] is acknowledged. K.F. visited University of Hyogo under partial support from the Association of International Education Japan (AIEJ), and N.S. visited Chulalongkorn University under the Thailand-Japan Technology Transfer Project (T)TTP-JBIC).

#### Supporting Information Available

Sensitivity analysis of the model (Table S1), energetic efficiency of the treatment process (Table S2), changes of pH during the treatment process (Figures S1, S2, and S3), and the phase-equilibrium concentration of acetaldehyde (Figure S4). This information is available free of charge via the Internet at http://pubs.acs.org.

### Nomenclature

Mament	idiate
[AA]	concentration of aqueous acetic acid (mol L-1)
[AD]	concentration of aqueous acetaldehyde (mol $L^{-1}$ )
[CC]	concentration of aqueous catechol (mol 11)
(HQ)	concentration of aqueous hydroquinone (mol $L^{-1}$ )
[OH]	concentration of aqueous hydroxyl radical (mol $L^{-1}$ )
(PH)	concentration of aqueous phenol (mol L-1)
(RC)	concentration of aqueous resorcinol (mol L-1)
[UP <sub>CI</sub> ]	concentration of unidentified intermediate $C_1$ products (mol $L^{-1}$ )
(UP <sub>C6</sub> )	concentration of unidentified intermediate $C_6$ products (mol $L^{-1}$ )
Carr; inf	influent concentration of gaseous acetaldehyde (ppm by mol)
Cu K eff	effluent concentration of gaseous acetaldehyde (ppm by mol)
$C_{p-t \ int}$	initial concentration of aqueous phenol (mg l -1)
dc	direct current (-)
I	corona discharge current (mA)
$J_A$	energetic efficiency of acetaldehyde (mol acetaldehyde J <sup>-1</sup> )
JP.	energetic efficiency of phenol (mol phenol J-1)
Imr	energetic efficiency of TOC (mol carbon J-1)
$k_l$	rate constant of ith reaction (L mol-1 s-1)
$m_a$	molecular mass of acetaldehyde (g mol-1)
$m_c$	atomic mass of carbon (g mol-1)

molecular mass of phenol (g mol-1)

501	$q_g$	molar flow rate of gas (mol sec-1)	purification by a wer
502	$R_{c-p}$	weight ratio of carbons in phenol (-)	composition of aqueo Chem. Eng. Jpn. 2004
503	$R_{c-a}$	weight ratio of carbons in acetaldehyde (-)	(16) Peyrous, R.; Pignolet, I
504	ľ	discharge time (sec)	species created by an el J. Phys. D: Appl. Phys
505 506 <b>50</b> 7	<i>t</i> <sub>1/2</sub>	period for which TOC under corona discharge is degraded by half of that without corona discharge (sec)	(17) Loiseau, J. F.; Mong Numerical simulation a cylindrical oxygen-to 27, 63-73.
508	TOC	total organic carbon (mg L-1)	(18) Moruzzi, J. L.; Phelps, reactions in O <sub>2</sub> , CO <sub>2</sub> , I
509	V	applied voltage (kV)	high pressures. J. Cher (19) Ushijima, S.; Nishioka,
510	W	total water volume (L)	O under atmospheric 758 –763.
511	Literatu	re Cited	(20) Colussi, A. J.; Weavers, dynamics and quantit 1998, 102, 6927–6934. (21) Joshi, A. A.; Locke, B.
512 513 514 515 516 517 518 519 520 521 522 523 524 525 526 527 528 529	oxy, ionin 287. (2) Sup stea gas 1656 (3) Seki Nor refo 4456 (4) Tan gas 171 (5) Tam vapy AIC	at, K.; Chavadej, S.; Lobba, L. L.; Mallinson, R. G. Combined in reforming and partial oxidation of methane to synthesis under electrical discharge. Ind. Eng. Chem. Res. 2003, 42, 4–1661.  ne, Y.; Urasaki, K.; Kado, S.; Matsukata, M.; Kikuchi, I. lequilibrium pulsed discharge: a novel method for steam rming of hydrocarbon or alcohols. Energy Fitels 2004, 18, 459.  non, H.; Mizoata, H.; Sano, N.; Okazaki, M. New concept of purification by electron attachment. AIChEJ. 1995, 41, 1701–1.  non, H.; Sano, N.; Okazaki, M. Influence of oxygen and water for on removal of sulfur compounds by electron attachment. IEJ. 1996, 42, 1481–1486.	hydroxyl radicals, hydr pulsed streamer corona Mater. 1995, 41, 3-30 (22) Shin, W. T.; Yaicoumi, discharge process for water. Ind. Eng. Chem. (23) Faungnawakij, K.; Sano panitkul, T.; Tanthapa dissolved inorganic ad hyde by use of wetted Eng. Technol. 2004, 27 (24) Sano, N.; Nagamoto, Removal of acetaldeh discharge reactor. Ind. 3791. (25) Butkovskaya, N. I.; Senstudy of reaction of hyd secondary reactions of Phys. Chem. A. 2000, 1
530 531 532 533	iodí	<ol> <li>N.; Nagamoto, T.; Tamon, H.; Okazaki, M. Removal of ne and methyl iodide in gas by wetted-wall reactor based elective electron attachment. J. Chem. Eng. Jpn. 1996, 29.</li> <li>S4.</li> </ol>	(26) Masaki, K.; Matsuoka, N.; Yonemoto, T. Kinei in the presence of TiO <sub>2</sub>

(7) Faungnawakij, K.; Sano, N.; Yamamoto, D.; Kanki, T.; Charinpanitkul, T.; Tanthapanichakoon, W. Removal of acetaldehyde in air using a wetted-wall corona discharge reactor. Chem. Eng. J. 2004, 103, 105-122.

534

535

536

537

538

539

540

541

542

543

544

545

546

547

548

549

550

551

552

553

554

555

556

557

558

559

560 561

562

563

564

565

(8) Yamamoto, T.; Ramanathan, K.; Lawless, P. A.; Ensor, D. S.; Newsome, J. R.; Planks, N.; Ramsey, G. H. Control of volatile organic compounds by an ac energized ferroelectric pellet reactor and a pulsed corona reactor. IEEE Trans. Ind. Appl.

(9) Haung, L.; Nakajo, K.; Ozawa, S.; Masuda, H. Decomposition of dichloromethane in a wire-in-tube pulsed corona reactor. Environ. Sci. Technol. 2001. 35, #275-1281.

(10) Kawamura, K. Simultaneous removal of NO, and SO, by electron

beam. Kagaku Kogaku 1989, 53, 820-821.
(11) Grymonpre, D. R., Finey, W. C.; Locke, B. R. Aqueous-phase pulsed streamer corona reactor using suspended activated carbon particles for phenol oxidation: model-data comparison. Chem. Ling. Sci. 1999, 54, 3095-3105. (12) Hoeben, W. F. L. M. Pulsei Corona-Induced Degradation of

Organic Materials in Water, Technische Universiteit Eindhoven: Eindhoven, The Netherlands, 2000.

(13) Sano, N.; Kawashima, T.; Fujikawa, J.; Fujimoto, T.; Takaaki, K.; Kanki, T.; Toyoda, A. Decomposition of organic compounds in water by direct contact of gas corona discharge: influence of discharge conditions. Ind. Eng. Chem. Res. 2002. 41, 5906-5911.

(14) Sano, N.; Yamamoto, D.; Kanki, T.; Toyoda, A. Decomposition of phenol in water by cylindrical wetted wall reactor using direct contact of gas corona discharge. Ind. Eng. Chem. Res. 2003, 42, 5423-5428.

(15) Faungnawakij, K.; Sano, N.; Yamamoto, D.; Kanki, T.; Charinpanitkul, T.; Tanthapanichakoon, W. Simultaneous gas-water

etted-wall e frona discharge reactor, deous phenol and gascous acetaldehyde. J. 4, 37 (11), 1373-1378.

506

567 568

569

570 571

572

573

574 575

576

577

578

579

580 581

582

583 584

585

566 587 588

589

590

591

592 593

594

595

597

598 599 600

601

602

604

605

606

607

CASS

609

610

611

612

613

614

615

616

617

619

620

621

622

623

624

626

627

628

629

630

631

632

633

634

635

636

P.; Held, B. Kinetic simulation of gaseous electrical discharge in dry or humid oxygen. vs. 1989, 22, 1658–1667.

ie, C.; Peyrous, R.; Held, R.: Coste, C. of ozone axia! and radial distribution in ed ozonizer. J. Phys. D: Appl. Phys. 1994,

A. V. Survey of negative-ion-molecule 1120, CO, and mixtures of these gases at em. Phys. 1966, 45, 4617-4627,

a, M.; Sadakata, M. Selective generation of c pressure. J. Chem. Eng. Jpn. 2004, 37(6).

s, L. K.; Holfmann, M. R. Chemical bubble itative sonochemistry. J. Phys. Chem. A.

R.; Arce, P.; Finney, W. C. Formation of drogen peroxide and aqueous electrons by na discharge in aqueous solution. J. Huzard.

S.; Tsouris, C.: Dai, S. A pulseless corona the oxidation of organic compounds in n. Res. 2000, 39, 4408-4414.

no. N., Yamamoto, D.; Kanki, T., Charin-anichakogn, W. Influence of oxygen and iditives on removal of gaseous acetaldeed-wall corona discharge reactor. Chem. 27 (10), 1115-1121.

T.; Tamon, H.; Suzuki, T.; Okazaki, M. hyde and skatole in gas by a corona-id. Eng. Chem. Res. 1997, 36, 3783-

iser, D. W. Infrared chemiluminescence droxyl radical with acetaldehyde and the of acetyl radical with NO<sub>2</sub>, OH, and H. J. 104, 9428 9435.

, K.; Takahashi, A.; Shibasaki-Kitakawa, etic of ultrasonic degradation of phenol 2 particles. Ultrason. Sonochem. 2005, 12 (4), 263-269,

(27) Jacob, D. J.: Gottlied, L. W.; Prather, M. J. Chemistry of a polluted boundary layer. J. Geophys. Res. 1989, 94, 12975 -13002.

(28) Walling, C.; Goosen, A. J. Mechanism of ferric ion catalyzed decomposition of hydrogen-peroxide-effect of organic sub-strates. J. Am. Chem. Soc. 1973, 95, 2987-2991.

(29) Bielskie, B. H. J.; Cabelli, D. E.; Anudi, R. L.; Ross, A. B. Reactivity of HO<sub>2</sub>/O<sub>2</sub> radical in aqueous solution. J. Phys. Chem. Ref. Data 1985, 14, 1041.

(30) Hoigne, J.; Bader, H. Ozonation of water: selectivity and rate

oxidation of solutes. Ozone Sci. Fing. 1979, 1, 357.

(31) Buxton, G. V.; Greenstock, C. L.; Helman, W. P.; Ross, A. B. Critical review of rate constants for reaction of hydrated electron. hydrogen atoms and hydroxyl radicals ('OH/'O') in aqueous

solution. J. Phys. Chem. Ref. Data 1988, 17, 693-694. (32) Bruno, L.; David, A. R.; Deborahm, R. B. Ozone in Water Treatment; Lewis Publishers file.. Chelsea, Mf. 1991.

Lukes, P.: Locke, B. R. Degradation of substituted phenols in a hybrid gas-liquid electrical discharge reactor. Ind. Eng. Chem. Res. 2005, 44, 2921-2930.

(34) Ginemo, O.; Carbajo, M.; Beltran, F. J.; Rivas, F. J. Phenol and substituted phenois AOPs remediation. J. Hazard. Mater. 2005, 119, 99 108

(35) Petriet, C.; Lamy, M. F.; Francony, A.; Benahcene, A.; David, B.; Renaudin, V.; Gondrexon, N. Sonochemical degradation of phenol in dilute aqueous solutions: comparison of the reaction rates at 20 and 487 kHz. J. Phys. Chem. 1994, 98, 10514.

Received for review June 10, 2005. Revised manuscript received November 28, 2005. Accepted December 12, 2005.

ES051102Y 637



## วารสารพระจอมเกล้าลาดกระบัง

JOURNAL OF KING MONGKUT'S INSTITUTE OF TECHNOLOGY LADKRABANG ISSN 0858-8430 Vol.11 No.1 April 2003 ปีที่ 11 ลบับที่ 1 เมษายน 2546

### ที่ปรึกษา :

รก ประกิจ ตั้งติสานนท์ รก คร.กวิล พื้นภา รก คร.กวิวรณ ขึ้นะกระกูล รก ตร.คูษณี ขนะบริพัฒน์ คร. วัฒนรัย พงษ์นาค รก. คร.บุญวัฒน์ อัตรุ ผส. คร.เผริญรัย โรยสิทธิ์ ผส. กุลธร เลื่อนครื รศ. คร.จุฬาวัสน์ เศรษฐกุล รศ. คร.ระลิพร หาเรือนกิจ ผส. คร.สุรพล เศรษฐบุตร

### บรรณาธิการ :

รศ ครุมนัส สังวรศิลป์

### ผู้ช่วยบรรณาธิการ :

รศ ครุวิสุทธิ์ รู้กิรุ่มรื่อง

### กอณรรณาธิการ :

รศ. ตร.อัญสลี วารีทสวัสดิ์ หล่อทองค่า รศ. สุภาวดี วัดนมาศ ผศ. ตร.สุรสิทธิ์ ราตรี ผศ. ตร.ทรงยศ ตันพิพัฒน์ ผศ. ตร.ปรีชา เทียนสมประสงท์ ผศ. ตร.วรพจน์ กริสุระเทช ผศ. ตร.วิระเซษฐ์ ขันเงิน ผศ. คร. ชัยวุฒิ ฉัศรถุทัย คร. นันทนา ถ้าประภาศิริ อาจารย์อุมาหา อุไรสกุล คร. จ่าวุญ เล้าลืนวัฒนา ผส. วินา ชูโชติ คร. จันทร์บุรณ์ สถิควิริยวงศ์ ผส. คร. สุทธิชัย นทนาถิพงษ์

### บรรณาธิการบริหาร :

นางบุศรีนทร์ ตันสัพัฒน์

### ผู้ช่วยบรรณาธิการบริหาร :

นางกาวสุดนธ์ มาศนุ้ย

นหสาวปทุมติพย์ สังชพันธุ์

### เจ้าของ :

งานเง่นสริมการวิจัย กอบรัการการศึกษา สถาบัณฑคโนโลยีพระจอมเกล้าเจ้าคุณภาวาสาจการบัง กานผลองกรุง เขตลาดการบัง กรุงภาพฯ 10620 โทรศัพท์: 0-2326-4992 พริย 0-2737-3000 คือ 3780 โทรสาร: 0-2326-4997 http://www.kmid.ac.th

#### กำหนดออก :

ปีละ 3 ฉบับ (เมษายน สิภาคม และ ชันวาคม)

### วัตถุประสงค์ :

- 1. เพื่อเผยแหว่ความรู้ความก้าวหน้าของผลงานด้านวิชาการและการวิจัยแก่ผู้สนใจทั่วไป
- เป็นสื่อกลางายงานข่าวสารที่เป็นประโยชน์และมีคุณค่าที่เกี่ยวข้องกับผลงานด้านวิชากรและวิจัย
- ที่อแลกเปลี่ยนแนวคิด/ความรู้ที่เกี่ยวร้องกับผลงานด้านวิชาการและวิจัย

ข้อคิดเพิ่มของบทกรามทุกเรื่องถืองทีมที่ในรารสารา จบับนี้เป็นของผู้เขียน กองบรรณาธิการไม่มีส่วนรับผิดขอบ หรือไม่จำเป็นต้องเห็นด้วยกับข้อคิดเห็นนั้น ๆ แต่อย่างใด

# การสังเคราะห์คาร์บอนกัมมันต์จากกะลามะพร้าว โดยวิธีการกระตุ้นทางเคมีสำหรับการดูดชับฟีนอล Synthesis of Activated Carbon from Coconut Shell by Chemical Activation for the Adsorption of Phenol

อัญชลิพร วาริทสาัสดิ์ หล่อทองคำ ธีระโชติ ศรีธิระวิโรจน์ วิวัฒน์ ตัวแทะพานิชกุล\* รองศาสตราจารย์ นักศึกษาปริญญาโท ศาสตราจารย์ ภาควิชาวิศวกรรมเคมื คณะวิศวกรรมศาสตร์ สถาบันเทคโนโลยีพระจอมเกล้าเจ้าคุณ หนารลาคกระบัง รภาควิชาวิศวกรรมเคมื คณะวิศวกรรมศาสตร์ จุฬาลงกรณ์มหาวิทยาลัย

### บหลัดย่อ

งานวิจัยนี้สังเคราะห์คาร์บอนกัมมันต์จากกะลามะพร้าว โดยการกระตุ้นทางเคมือ้วยสารละลายชิงค์คลอไรด์ 60% โดยน้ำหนัก สารละลายโซเดียมคลอไรด์อื่มตัว และสารละลายผสมระหว่างสารละลายซิงค์คลอไรด์ 60% โดยน้ำหนัก และสารละลายโซเดียมคลอไรด์อื่มตัว อัตราส่วน 1:1 และ 1:2 โดยน้ำหนัก และศึกษาประสิทธิภาพการดูดขับสารละลายพื้นอลที่ความเข็มขัน 100-500 มก./ล. วิเคราะห์สภาพพื้นผิว พื้นที่ผิวจำเพาะ ขนาดของรูพรุน และปริมาตรรูพรุนรวม สภาวะการกระตุ้นที่เหมาะสม คือ ใช้สารละลาย ซิงค์คลอไรด์ 60% โดยน้ำหนัก อัตราส่วนของกะลามะพร้าวต่อสารกระตุ้น 1:2 โดยน้ำหนัก ที่อุณหภูมิ 800 'ช และเวลาการกระตุ้น 60 นาที คาร์บอนกัมมันต์ที่ได้จากสภาวะการกระตุ้นนี้มีพื้นที่ผิวจำเพาะ 1,193 ตร.ม./ก. มีรูพรุนะแบบไมโครพอร์ขนาดเฉลี่ย 13.92 อังสตรอม มีปริมาตรรูพรุนรวม 0.544 ลบ.ชม./ก. สามารถดูดขับปริมาณพินอลที่ทุกจำความเข้มขันสูงกว่าอาร์บอนกัมมันต์ ตัวอย่างอื่น และปริมาณการดูดขับใกล้เคียงกับคาร์บอนกัมมันต์ที่ใช้ทางการด้า (HRO CH M325-60) ที่มีพื้นที่ผิวจำเพาะ 1,160 ตร.ม./ก. ขนาดรูพรุนแบบไมโครพอร์เฉลี่ย 14.02 อังสตรอม และปริมาตรรูพรุนรวม 0.510 ลบ.ชม./ก. ผลการทดลองพบว่า ที่ความเข้มข้นสารละลายพื้นอล 100 มก./ล. และ 500 มก./ล. คำปริมาณการดูดขับของดาร์บอนกัมมันต์ที่ได้จากสภาวะการ กระตุ้นที่เหมาะสมนี้เท่ากับ 25.02 มก./ก. และ 103.63 มก./ก. คิดเป็นประสิทธิภาพการดูดขับ 99.71 % และ 94.93 % ตามลำดับ คำสำคัญ : คาร์บอนกัมมันต์ กะคามะทร้าว การคดขับ พินอล

#### Abstract

This work synthesized activated carbon from coconut shell by chemical activation using the solutions of zinc chloride 60 wt %, saturated sodium chloride and the mixture of both solutions at weight ratios of 1:1 and 1:2. The adsorption of phenol solutions at concentrations of 100-500 mg/l, surface of activated carbon, specific surface area, pore size diameter and total pore volume were studied. The optimum activation condition is using 60-wt% zinc chloride solution at weight ratio of coconut shell to activating agent 1:2, activation temperature at 800 °C and activation time 60 min. The activated carbon synthesized at this condition has specific surface area of 1.193 m²/g, mean micropore diameter of 13.92 :: and total pore volume of 0.544 cm ³/g. This activated carbon gave the highest adsorption capacity at all phenol concentrations companing with the other synthesized activated carbons. Its adsorption capacity was nearly the same as that from the commercial one (HRO CH M325-60), with specific surface area of 1.160 m²/g, mean micropore diameter of 14.02 ii and total pore volume of 0.510 cm ³/g. The adsorption capacity at phenol concentrations of 100 and 500 mg/l were 2502 mg/g and 103.63 mg/g, corresponding to 99.71% and 94.93% efficiency, respectively.

Keywords: Activated Carbon, Coconut Shell, Adsorption, Phenol

### 1. บทน้ำ

ปัญหามลพิษทางน้ำเป็นปัญหาทางสิ่งแวคล้อมที่สำคัญ ปัญหาหนึ่ง น้ำทิ้งจากโรงงานอุตสาหกรรมและแหล่งชุมชน ที่ถูกระบายลงสู่แหล่งน้ำธรรมชาติต่าง ๆ ทำให้คุณภาพของ แหล่งน้ำสดลง เพราะบางครั้งนอกจากจะมีสารอินทรีย์หรือ สารอนินทรีย์ปะปนอยู่เป็นปริมาณสูงแล้ว อาจมีสารพิษ เกินมาตรฐานอุตสาหกรรม ทำให้เป็นอันตรายต่อสิ่งมีชีวิต ที่อาศัยอยู่ในเหล่งน้ำนั้น

คาร์บอนกัมมันต์ (Activated Carbon) มีคุณสมบัติเป็น สารคูดชับที่ดีเพราะมีความเป็นรูพรุนและมิพื้นที่ผิวภายในสูง จึงมีการนำการ์บอนกัมมันต์มาใช้ประโยชน์ในด้านต่าง ๆ เช่น ใช้ในการปรับปรุงคุณภาพน้ำดื่มโดยใช้ก่าจัดความชุน สี กลิ่น และรส (1) ใช้ในระบบบาบัตน้ำเสียในการดูดซับสารอินทรีย์ และสารพิษ เช่น ฟินอล ซึ่งมักเกิดจากโรงงานอดสาหกรรม ประเภทโรงงานผลิตพลาสติก โรงงานผลิตสีย้อมผ้า โรงงาน ผลิตพื้นอลิกเรซิน คาร์บอนกัมมันต์ที่ใช้ในประเทศส่วนใหญ่ จะนำเข้ามาจากต่างประเทศ และมีราคาแพง งานวิจัยนี้เป็นการ ศึกษาต่อเนื่องเพื่อที่จะนำคาร์ยอนกัมมันค์ที่เตรียมจากกะลา มะพร้าวซึ่งเป็นวัสดูเหลือทิ้งจากการเกษตรที่หาได้ง่ายและมี ราคาถูกมากระตุ้นทางเคมืด้วยสารสะสายชิงค์คลอไรด์ 60% โดยน้ำหนัก สารละลายโซเดียมคลอไรค์อื่มตัว และสารละลาย ผสมระหว่างสารละลายชิงค์คลอไรด์ 60% โดยน้ำหนักและ สารละลายโชเดียมคลอไรด์อื่มตัวที่สภาวะเทมาะสม คือ อัตราส่วนโดยน้ำหนัก 1:1 และ 1:2 |2| และทดสอบการคูดซับ สารละลายฟินอลความเข้มขัน 100-500 มก./ล. และเปรียบ เทียบกับคาร์บอนกัมมันต์ที่ใช้ทางการค้า งานวิจัยนี้วิเคราะห์ สภาพพื้นผิวด้วยกล้องจลทรรศน์อิเล็กตรอน (Scanning Electron Microscope: SEM Tu JEOL JSM-5800LV) และ วิเคราะท์พื้นที่ผิวจำเพาะและปริมาตรรูพรุนรวมด้วยเครื่อง Autosorb รุ่น AUTOSORB-1

### 2. ทฤษฎีและหลักการ [1, 3-7]

### 2.1 วัตถุดิบสำหรับผลิตการ์บอนกัมมันต์

วัตถุดิบที่ใช้ในการผลิตคาร์บอนกัมมันต์แบ่งเป็นพวก เซลลูโลสทุ๊ได้จากพืช เช่น กะลามะพร้าว ชานอ้อย ซังช้าวโพด ขี้เลื่อย พวกวัตถุดิบที่ได้จากสัตว์ เช่น เลือด กระดูก นอกจากนี้ยังได้มาจากถ่านหิน เช่น ลิกไนต์ พีท วัสดุที่น่า มาใช้เป็นวัตถุดิบควรมีปริมาณการ์บอนสูง คาร์บอนกัมมันต์ ที่ผลิตจากกะลามะพร้าว กะลาตาลโตนด ซึ่งเป็นวัสดุที่มี ความหนาแน่นสูงและมีสารระเทยสูง จะมีปริมาณของรูพรุน ขนาดเล็กสูงและสามารถใช้ดูคชับสารซึ่งอยู่ในสถานะของเหลว หรือก๊าซ การแบ่งชนิดของวูพรุนตาม IUPAC จะแบ่งเป็น รูพรุนระดับไมโครพอร์มีขนาดเล็กกว่า 2 นาโนเมตร รูพรุน ระดับเมโชพอร์มีขนาด 2-50 นาโนเมตร และรูพรุนระดับ แมคโครพอร์มีขนาดใหญ่กว่า 50 นาโนเมตร [4]

### 2.2 การผลิตคาร์บอนกัมมันต์

2.2.1 การคาร์บอไนเซซัน (Carbonization) เป็นการนำ วัตถุติบมาเผาในสภาวะที่มีออกซิเจนน้อย (Pyrolysis) สารที่ ไม่ใช่คาร์บอน เช่น ไฮโดรเจน และออกซิเจนจะถูกไล่ออก ในรูปของก๊าซ คาร์บอนอิสระที่มีอยู่จะรวมตัวกันเป็นผลึก ทำให้ได้ผลิตภัณฑ์ในรูปของถ่านซาร์ ขนาดของผลึกขึ้นอยู่ กับองค์ประกอบและโครงสร้างของวัตถุดิบ และอุณหภูมิของ การเผา ถ่านุชาร์ที่ได้จากขั้นตอนนี้จะมีความสามารถในการ ดูดซับต่ำ เพราะการทำให้เป็นถ่านใช้อุณหภูมิ 400-500 ซ จึง ยังคงมีน้ำมันดิน (Tar) ตกค้างอยู่ภายในรูพรุนหรือเกาะอยู่ ตามผิว ดังนั้นต้องนำไปผ่านกระบวนการกระตุ้นเพื่อเพิ่ม ความสามารถในการดูดซับ

2.2.2 การกระดุ้น (Activation) เป็นขั้นตอนที่ทำให้ ความพรุนและพื้นที่ผิวจำเพาะเพิ่มขึ้น โดยการกำจัดให้น้ำมัน ดินหลุดออกมา ทำให้คาร์บอนกัมมันต์ที่ได้มีความสามารถใน การดูดซับสูงขึ้น การกระตุ้นทำได้ 2 วิธี คือ การกระตุ้นด้วย วิธีทางกายภาพและทางเกมี

มานัด แก้วถาวร |5| ศึกษาการผลิตคาร์บอนกัมมันต์ จากกะลามะพร้าวโดยใช้สารละลายโซเดียมคลอไรค์อื่มตัว ซึงค์คลอไรด์ 55% โดยน้ำหนัก และก๊าชคาร์บอนไดออกไซด์ เป็นสารกระตุ้น ตัวแปรที่ศึกษา คือ อุณหภูมิ อัตราส่วน ของสารกระตุ้นต่อกะลามะพร้าว อัตราการไหลของก๊าซ การ์บอนไดออกไซด์ ขนาดของกะลามะพร้าว เวลาในการ กระตุ้น หบว่าสภาวะที่เหมาะสมในการผลิตคาร์บอนกัมมันต์ สำหรับสารกระตุ้นทั้ง 3 ชนิด คือ อุณหภูมิ 900 ช อัตราส่วน ของสารกระตุ้นทั้ง 3 ชนิด คือ อุณหภูมิ 900 ช อัตราส่วน ของสารกระตุ้นต่อกะลามะพร้าว 1:2 โดยน้ำหนัก อัตราการ ไหลของก๊าซการ์บอนไดออกไซด์ 100 ล./ชม. ขนาดของกะลา

มะพร้าว 1 ซม. x 1 ซม. เวลาในการกระตุ้น 120 นาที เมื่อใช้ โซเดียมกลอไรด์อื่มตัวและก๊าซดาร์บอนไดออกไซด์เป็น สารกระตุ้น จะได้คำการดูคชับไอโอดีน 694 มก./ก. คิดเป็น ร้อยละของผลผลิต 24.57 เมื่อใช้ซิงค์คลอไรด์ 55% โดย น้ำหนักและก๊าซดาร์บอนไดออกไซด์เป็นสารกระตุ้น จะได้ คาร์บอนกัมมันต์มีคำการดูคชับไอโอดีน 686 มก./ก. และ ร้อยละของผลผลิต 33.60 และเมื่อใช้ก๊าซดาร์บอนไดออกไซด์ เป็นสารกระตุ้นเพียงอย่างเดียว จะได้ดาร์บอนกัมมันต์มีค่า การดูคชับไอโอดีน 741 มก./ก. และร้อยละของผลผลิต 22.37

วรี จำลองราษฎร์ [6] สึกษาการกำจัดสารอินทรีย์และ ฟื้นอลด้วยระบบเอสที่อาร์-ดาร์บอนกับมันต์สนิดเกล็ด (CGC-11) ชนาด 1.77-2.36 มม. และระบบควบคุม (ระบบ เอสบ็อาร์ที่ไม่มีการเดิมคาร์บอนกัมมันต์ชนิดเกล็ด) ดาร์บอน กัมมันต์ที่ใช้ผลิตจากกะลามะพร้าว มีปริมาณพื้นที่ผิวจำเพาะ 1,050-1,150 ตร ม./ก. ตัวแปรที่ศึกษา คือ บริมาณคาร์บอน กัมมันต์ ระยะเวลากักเก็บน้ำ ความเข้มข้นของฟืนอลที่ใช้ เท่ากับ 1,000 มก./ล. พบว่าปริมาณศาร์บอนกันนั้นต์ที่เหมาะสม ในระบบเอสบีอาร์-คาร์บอนกัมมันด์ชนิดเกล็ด คือ 1 000 มก สามารถทำจัด COD เหลือ 16 มก./ล. และพื้นอลเหลือ 0.2 มก./ก. ที่ระยะเวลากักเก็บน้ำ 1 วัน เมื่อเพิ่มระยะเวลากักเก็บน้ำเป็น 3, 5 และ 10 วัน ปริมาณ COD คือ 16, 14.5 และ 8 มก /a. และเหลือพีนอล 0.08 0.023 และ 0.014 มก./ล ส่วนใน ระบบควบคุมสามารถกำจัด COD เหลือ 122 มก/ล และ พื้นอลเหลือ 3.1 มก./ล. ที่ระยะเวลากักเก็บน้ำ 1 วัน เมื่อเพิ่ม ระยะเวลากักเก็บน้ำเป็น 3. 5 และ 10 วัน ปริมาณ COD คือ 48, 32 และ 16 มก./ล. และเหลือพินอล 0.35, 0.18 และ 0.018 มก./ล. ขามลำคับ

Teng และ Hsieh [7] ศึกษาการดูดซับพื้นอลใน
วัญภาคของหลวด้วยการ์บอนกัมมันต์ที่เตรียมจากถ่านบิทูมินัส
โดยการออกซีไดล์และไม่ออกซีไดส์ด้วยก๊าซดาร์บอนไดออกไซด์
ที่อุณหภูมิ 900° ขนาดของถ่านบิทูมินัสที่ใช้อยู่ในช่วง 0.421.0 มม การดูดซับพื้นอลใช้ความเข้มข้น 500 มก./ล และปริมาณ
คาร์บอนกัมมันต์ 0.2 กรัม ที่อุณหภูมิ 30° พบว่าคาร์บอน
กัมมันด์ที่เตรียมได้ทั้งจากการออกซิไดส์และไม่ออกซิไดส์
ด้วยก๊าซดาร์บอนไดออกไซด์จะมีวูพวุนแบบไมโดรพอร์
ขนาดรูพวุนเฉลี่ย 20-22 อังสตรอม อาร์บอนกัมมันต์ที่เตรียม

ได้จากการออกซิไดส์ด้วยก๊าชคาร์บอนไตออกไชด์ มีปริมาณ ทั้นที่ผิวจำเพาะ 950 สร.ม/ก. ปริมาตรรูพรุนรวม 0.50 สบ.ชม/ก. และมีปริมาณการดูดซับฟืนอลต่อกรับของคาร์บอนกับมันต์ (Q) ประมาณ 200 มก./ก. ส่วนคาร์บอนกับมันต์ที่เตรียมโดยไม่ ออกซิไดส์ด้วยก๊าซคาร์บอนไตออกไซด์ มีปริมาณพื้นที่ผิว จำเพาะ 634 ตร.ม./ก. ปริมาตรรูพรุนรวม 0.34 ลบ.ชม./ก. และมีปริมาณการดูดซับฟืนอลต่อกรับของคาร์บอนกับมันด์ ประมาณ 138 มก./ก.

### 3. การทดลอง

### 3.1 สภาวะที่ใช้ในการเครียมคาร์บอนกัมมันด์

การเตรียมคาร์บอนกัมมันต์ใช้สภาวะที่ได้ศึกษาแล้ว จากผลงานของธีระโชติและอัญชลีพร |2| ดังดารมที่ 1

สารางที่ 1 สภาวะที่เหมาะสมในการเตรียมคาร์บอนบัมมันด์ [2]

สารกระคุ้น	อัตราส่วน กะลามะพร้าว ต่อสารกระตุ้น (โดยน้ำหนัก)	ลูณหภูมิ ที่ใช้กระตุ้น (ชี)	รวคา ที่ใช้กระตุ้น (นาที)
ZnC1, 60 wr.%	1:2	800	60
NaC1	1:3	800	90
ZnC1, 60 wt.%: NaC1 (1:1) โดยน้ำหนัก	1:3	600	90
ZnC1, 60 wt.%: NaC1 (1:2) โดยน้ำหนัก	1:2	600	60

### 3.2 การเตรียมคาร์บอนกับมันด์

ผสมกะลามะพร้าวขนาดเฉลี่ย 1 ซม. x 1 ซม.ที่อบแห้ง ที่อุณหภูมิ 110°ช กับสารกระตุ้นตามอัตราส่วนในตารางที่ 1 นำไปอบที่อุณหภูมิ 130°ช จนแห้งแล้วนำไปเผาในเตาเผา ไฟฟ้าที่อุณหภูมิและเวลาตามตารางที่ 1 ล้างการ์บอนกัมมันด์ ที่ได้ด้วยน้ำกลั่นร้อน กรดเกลือเข้มขัน 5% โดยน้ำหนัก และ น้ำกลั่นร้อนจนเป็นกลาง จากนั้นนำไปอบที่อุณหภูมิ 160°ช เป็นเวลา 6 ซม. แล้วทั้งให้เย็นในโถดูดความขึ้น ชั่งน้ำหนัก และคำนวณปริมาณคาร์บอนกัมมันต์ที่ได้ แล้วนำไปบดและร่อน ผ่านตะแกรงขนาด 325 เมช (45 ไมโครเมตร) ตามมาตรฐาน ผลิตภัณฑ์อุตสาหกรรม (มอก. 900-2532) จากนั้นนำไปอบที่อุณหภูมิ 150°ช เป็นเวลา 3 ซม. แล้วทั้งให้เย็นในโถดูดความขึ้น

### 3.3 การศึกษาสภาพพื้นผิว

วิเคราะห์สภาพพื้นผิวของกะลามะพร้าว คาร์บอนกัมมันต์ ที่เตรียมได้และคาร์บอนกัมมันต์ที่ใช้ทางการค้า (HRO CH M325-60) ด้วยกล้องจุลทรรศน์อิเล็กตรอน

### 3.4 การวิเคราะห์พื้นที่ผิวจำเพาะและปริมาตรของรูพรุน รวม (8)

ชั่งกะลามะพร้าว การ์บอนกัมมันต์ที่เตรียมได้ หรือ การ์บอนกัมมันต์ที่ใช้ทางการด้า 0.01 กรัม ใส่ในเชลหลอดแก้ว ทำการทดลองภายใต้บรรยากาศก๊าซในโตรเจนที่อุณหภูมิ 350°ช เป็นเวลาอย่างน้อย 3 ชม. จากนั้นทาพื้นที่ผิวจำเพาะ และ ปริมาตรของรูพรุนด้วยเครื่อง Autosorb

### 3.5 การดูดขับสารละลายฟื้นอล

ชั่งกะลามะพร้าว คาร์บอนกัมมันต์ที่เตรียมได้ คาร์บอน กัมมันต์ที่ใช้ทางการค้าอย่างละ 1 กรัม ใส่ในขวดรูปชมพู่ ชนาด 250 มล. เทสารละลายพืนอลความเข้มข้น 100 มก./ล. จำนวน 200 มล. ลงไป แล้วเขย่าตัวยเครื่องเขย่าที่อุณหภูมิห้อง เป็นเวลา 4 ชม. นำตัวอย่างมากรองคาร์บอนกัมมันต์ออก ด้วยกระดาษกรอง Whatman เบอร์ 42 ผ่านเครื่องกรอง สุญญากาศและวิเคราะห์หาปริมาณพืนอลที่เหลือด้วยเครื่อง UV Spectrophotometer ที่ความยาวคลื่น 263 นาในเมตร ทำการ ทดลองซ้ำแต่เปลี่ยนความเข้มข้นของสารละสายพืนอลเป็น 200, 300, 400 และ 500 มก./ล. ตามลำดับ จากนั้นหา ไอโซเทอม และประสิทธิภาพการดูดชับจากค่าปริมาณการ ดูครับทีนอลที่คำนวณได้

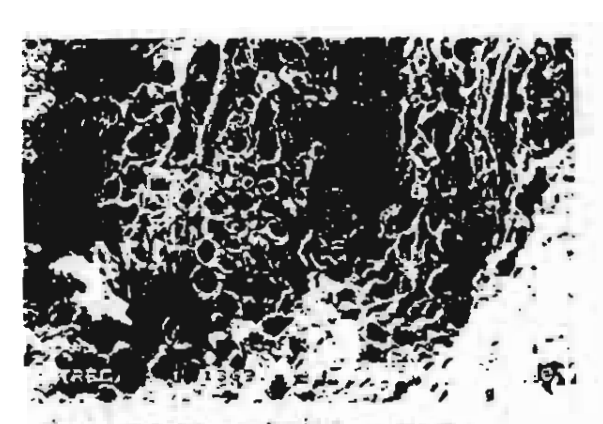
พ<u>มายเหตุ</u> ผลภาษทดลองราง ๆ ได้จากการทำล้าอย่างน้อย 3 ครั้ง

### 4. ผลการทดลองและการวิเคราะห์ผล

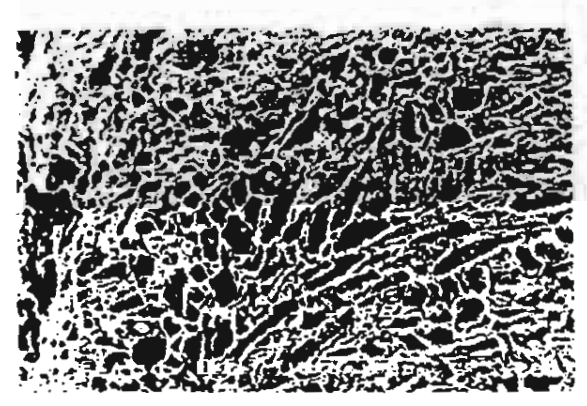
เพื่อความสะดวกจะกำหนด CS แทนกะลามะพร้าว AC1. AC2, AC3 และ AC4 แทนคาร์บอนกัมมันต์ที่กระตุ้นด้วย สารละลายซึงค์คลอไรด์ 60%โดยน้ำหนัก สารละลายโชเดียม คลอไรด์อิ่มตัว สารละลายผสมระหว่างซึงค์คลอไรด์ 60%โดยน้ำหนักและสารละลายโซเดียมคลอไรด์อิ่มตัว อัตราส่วนโดยน้ำหนัก 1:1 และ1:2 ตามลำดับ ส่วนคาร์บอนกัมมันต์ที่ใช้ ทางการค้า คือ HRO CH M325-60

### 4.1 การศึกษาสภาพพื้นผิวด้วย SEM

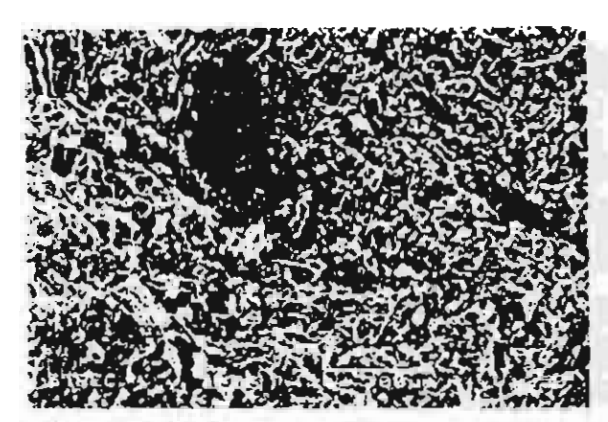
จากรูปที่ 1 จะเห็นว่ากะลามะพร้าวมีสภาพพื้นผิวแตกต่าง จากผิวคาร์บอนกัมมันต์ที่แสดงในรูปที่ 2-6 รูพรุนของ กะลามะพร้าวมีปริมาณค่อนข้างน้อยกว่า เพราะองค์ประกอบ ต่าง ๆ เช่น สารระเทย น้ำมันดินในกะลามะพร้าวยังไม่ได้ ถูกเผาไป ในรูปที่ 2 และ 6 จะเห็นว่าคาร์บอนกัมมันต์ที่ใช้ สารละลายชิงค์คลอไรด์ 60% โดยน้ำหนักเป็นสารกระตุ้น และ คาร์บอนกัมมันต์ที่ใช้ทางการค้ามีความหนาแน่นของจำนวน รูพรุนมากกว่าคาร์บอนกัมมันต์ที่กระตุ้นด้วยสารละลาย โชเตียมคลอไรด์ 60% โดยน้ำหนักและสารละลายโชเตียมคลอไรด์ อีมตัวอัตราสานโดยน้ำหนักและสารละลายโชเตียมคลอไรด์ อีมตัวอัตราสานโดยน้ำหนักและสารละลายโชเตียมคลอไรด์



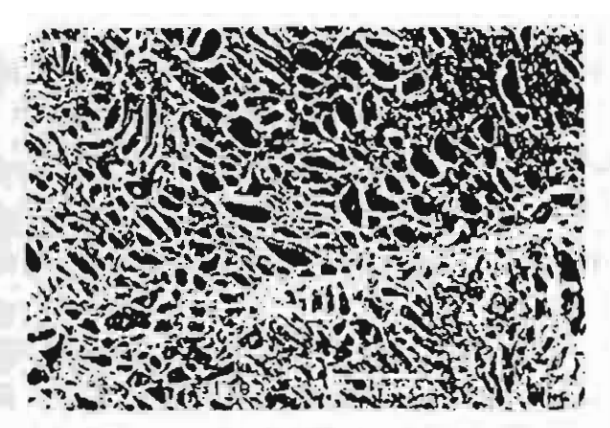
รูปที่ 1 7ป SEM ของกะลามะพร้าว ที่กำลังขยาย 250 เท่า



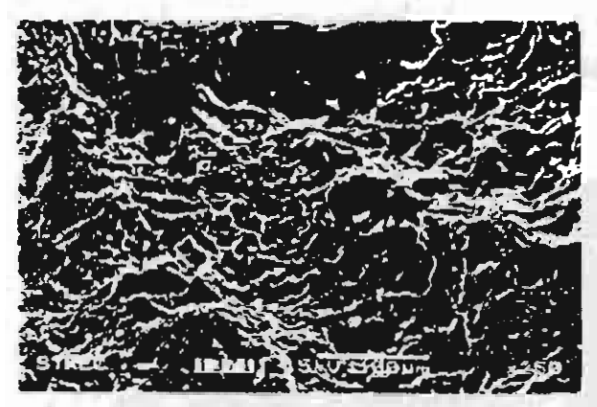
รูปที่ 2 วูป SEM ของคาร์บอนกัมมันต์เมื่อใช้สารณะลายจึงค์คลอไรด์ 60% โดยน้ำหนักเป็นสารกระตุ้น ที่กำลังจยาย 250 เท่า



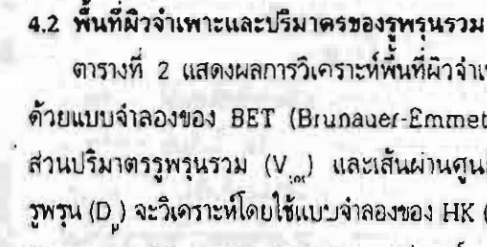
รูป SEM ของการ์บอนกัมมันต์เมื่อใช้สารละลายโซเดียมคลอไรด์ อิมตัวเป็นสารกระตุ้น ที่กำลังขยาย 250 เท่า



7ป SEM ของคาร์บอนกัมมันต์: ชี้ทางการค้า (HRO CH M325-60) ที่กำลังขยาย 250 เท่า

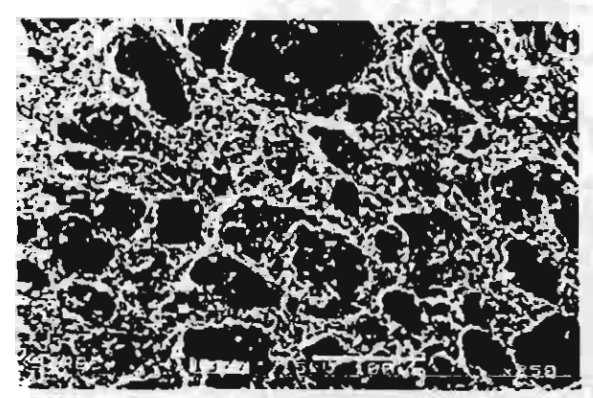


วูป SEM ของคาร์บอนกัมมันต์เมื่อใช้สารละลายผสมระหว่าง ซึ่งดั คลอไรด์ 60% โดยน้ำหนักและสารละลายโซเดียมคลอไรต์อิมตัว อัตราส่วนโดยนำหนัก 1:1 เป็นสารกระตุ้น ที่กำลังขยาย 250 เพ่า



ตารางที่ 2 แสดงผลการวิเคราะห์พื้นที่ผิวจำเพาะ (Spec) ด้วยแบบจำลองของ BET (Brunauer-Emmette-Teller) ส่วนปริมาตรรูพรุนรวม (V.,) และเส้นผ่านศูนย์กลางของ รพรุน (D) จะวิเคราะห์โดยใช้แบบจำลองของ HK (Horvath -Kawazoe) [8] จากผลการทดลองพบว่าคาร์บอนกัมมันต์ AC1 มีพื้นที่ผิวจำเพาะและปริมาตารูพรุนรวมใกล้เคียงกับ คาร์บอนกัมมันต์ที่ใช้ทางการค้า และสูงกว่าคาร์บอนกัมมันต์ AC2, AC3, AC4 และกะลามะพร้าว ซึ่งกะลามะพร้าวจะมี พื้นที่ผิวและปริมาตราพรุนรวมต่ำที่สุดเมื่อเทียบกับคาร์บอน กัมมันต์ ทั้งนี้เพราะกะลามะพร้าวยังไม่ได้ผ่านกระบวนการคาร์ บอไนเซชันและกระบวนการกระตุ้นด้วยสารเคมีเหมือนกับ คาร์บอนกัมมันต์ที่เตรียมได้และคาร์บอนกัมมันต์ที่ใช้ทางการค้า ดังนั้นองค์ประกอบต่างๆ ในกะลามะพร้าวจึงยังไม่ได้ถูกเผา ออกไปส่วนขนาดของรุพรุนจะสังเกตได้ว่าไม่แคกต่างกันมากนัก

จากงานวิจัยของ Hu และ Srinivasan [9] พบว่า การ์บอนกัมมันต์ที่เตรียมจากกะลามะพร้าวโดยการกระตุ้น ด้วยโพแทสเซียมไฮดรอกไซด์ที่อุณหภูมิ 800 ซ มีปริมาณ พื้นที่ผิวจำเพาะ 2,451 ตร ม /ก. มีรูพรุนขนาดเฉลีย 19.8 อังสตรอม ปริมาตรฐพรุนรวม 1.210 ลบ.ชม./ก. และมีปริมาณ การดูดซับฟินอลต่อกรับของคาร์บอนกัมมันต์ 396 มก./ก. ซึ่ง จะสูงกว่าเมื่อเทียบกับคาร์บอนกัมมันต์ ACI



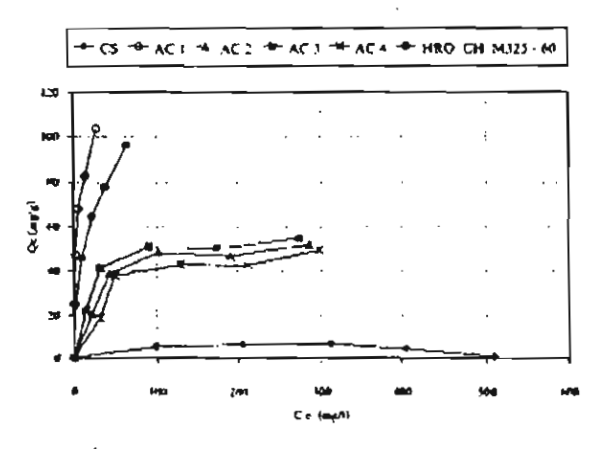
รูปที่ 5 รูป SEM ของคาร์ขอนกัมมันท์เมื่อให้สาวละลายผสมระหว่าง ริงค์คลอไรด์ 60% โดยน้ำหนักและสารละลายโซเดียมคลอไรด์ อิมพัวอัตราสานโดยนำหนัก 1:2 เป็นสารกระตุ้น ที่กำลังขยาย 250 เท่า

ตรรงที่ 2 ผลการวิเคราะห์พื้นที่ผิวจำเพาะและปริมาณรูพรุนราม

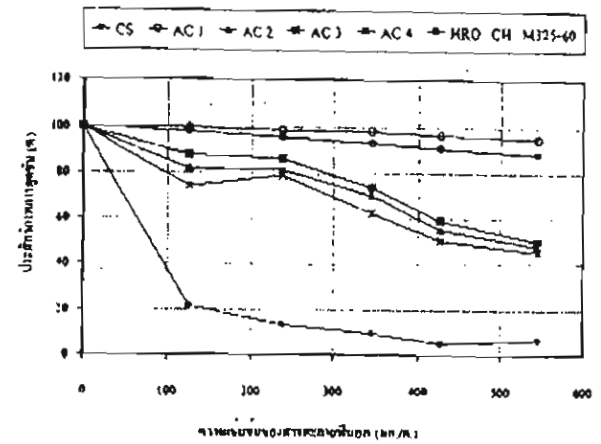
Sample	S <sub>sec</sub> (m²/g)	V (cm²/g)	D, (C)
cs	89.13	0.003	15.73
AC1	1,193	0.544	13.92
AC2	402.60	0.175	13.67
AC3	578.40	0.262	15.23
AC4	259.10	0.097	13.52
HRO CH M325-60	1.160	0,510	14.02

### 4.3 ผลการศึกษาการลูดซับสารละฮายฟีนอล

รูปที่ 7 แสดงความสัมพันธ์ระหว่างปริมาณสารละลาย พื้นอลที่ถูกดูดซับต่อกรัมของคาร์บอนกัมมันต์ (Q) กับความ เข้มขันของสารละลายพื้นอลที่สภาวะสมคุล (C) จากกราฟ ไอโซเทอมการดูดซับ พบว่าศาร์บอนกัมมันต์ AC1 จะมีค่า Q สูงที่สุด โดยสังเกตจากความชันของกราฟที่สูงกว่าที่คำความ เข้มข้นของสารละลายพื้นอลที่เท่ากัน ซึ่งสอดคล้องกับผลการ วิเคราะห์พื้นที่มิวจำเพาะและปริมาถรของรูพรุนรวม จากรูปที่ 8 และตารางที่ 3 พบว่าประสิทธิภาพการดูดซับสารละลายพื้นอล ที่ความเข้มข้นเท่ากันของคาร์บอนกัมมันต์ AC1 สูงกว่า คาร์บอนกัมมันต์ AC3, AC2 และ AC4 ตามลำคับ แต่ใกล้ เคียงกับการ์บอนกัมมันต์ที่ใช้ทางการค้า (HRO CH M325-60) ส่วนกะลามะพร้าว CS จะมีประสิทธิภาพการดูดซับต่ำที่สุด ซึ่งสอดคล้องกับผลการวิเคราะห์พื้นที่ผิวจำเพาะและปริมาตร ชองรูพรุนรวม ที่แสดงในตารางที่ 2



รูปที่ 🖍 ไอโซเทอมการตุดซับสารละลายพื้นอลบนภาร์บอนกับมันต์



รูปที่ 8 ประสิทธิภาพการคุดขับของสารละลายพื้นอลที่ความเริ่มขั้นค่างๆ

ดารางที่ 3 ปริมาณการดูดจับสารละลายฟินอล

สารดูดซับ	บริมาณการ <b>ดูดข</b> ับฮารตะตายพื้นคล (มก.ก.)									
	C1	C2	C3	C4	Cts					
CS	5.42	6.52	6.66	4.31	7.40					
AC1	25.02	47.19	67.87	82.54	103.63					
AC2	20.56	38.91	48.57	46.99	52.03					
AC3	22.11	41.27	50.98	50.43	54.57					
AC4	18 65	37.71	43.22	42.82	49.49					
HRO CH M325-60	24.67	45.67	64.45	77.58	96.36					

<u>หมายเหตุ</u> C1-C5 คือ ความเริ่มรับสารละลายพื้นอลก่อนการดูครับ

C1 = 100 มก./ล., C2 = 200 มก./ล., C3 = 300 มก./ล.,

C4 = 400 มก./ล. และ C5 = 500 มก./ล.

### 5. สรุปผลการทดลอง

สารกระดุ้นที่ดีที่สุด คือ สารละลายชิงค์คลอไรด์ 60% โดยน้ำหนัก การ์บอนกัมมันต์ที่ได้มีปริมาณพื้นที่ผิวจำเพาะ 1,193 ตร.ม./ก. มีรูพรุนแบบไมโครพอร์ชนาดเฉลี่ย 13.92 อังสตรอม มีปริมาตรรูพรุนรวม 0.544 ลป.ชม./ก. มีปริมาณ การดูดซับฟินอลที่ทุกค่าความเข้มข้นสูงกว่าคาร์บอนกัมมันต์ ตัวอย่างอื่น และใกล้เคียงกับคาร์บอนกัมมันต์ที่ใช้ทางการค้า (HRO CH M325-60) ที่มีปริมาณพื้นที่ผิวจำเพาะ 1.160 ตร.ม./ก. ชนาดรูพรุนเฉลี่ย 14.02 อังสตรอม และปริมาตรรูพรุนรวม 0.510 ลบ.ชม./ก. ที่ความเข้มข้นสารละลายฟินอล 100 มก./ล. และ 500 มก./ล. ค่าปริมาณการดูดซับของคาร์บอนกัมมันต์ ที่ได้จากการกระตุ้นตัวยสารละลายซิงค์คลอไรด์ 60% โดย น้ำหนัก เท่ากับ 25.02 มก./ก. และ 103.63 มก./ก. คิตเป็น ประสิทชิภาพการดูดซับ 99.71 % และ 94.93 % ตามลำดับ

### ก็ตดิกรรมประกาศ

โครงงานวิจัยนี้ได้รับเงินอุดหนุนบางส่วนจากโครงการเมธิ
วิจัยอาวุโส สกว. - ส.ดร. วิวัฒน์ ตัณฑะพานิชกุล ปึงบประมาณ
2545 และโครงการวิจัยร่วมภาครัฐ-เอกชนของศูนย์เชี่ยวชาญ
เฉพาะทางด้านเทคโนโลยีอนุภาค จุฬาลงกรณ์มหาวิทยาลัย
ปึงบประมาณ 2545 และบัณฑิตวิทยาลัย สถาบันเทคโนโลยี
พระจอมเกล้าเจ้าคุณทหารลาดกระบัง ขอขอบคุณบริษัท
คาร์โบกาญจน์ จำกัด ที่ให้การสนับสนุนคาร์บอนกัมมันต์ (HRO
CH M325-60) และขอขอบคุณภาควิชาเคมี คณะวิทยาศาสตร์
สถาบันเทคโนโลยีพระจอมเกล้าเจ้าคุณทหารลาดกระบัง ที่ให้
ความอนุเคราะห์เครื่องมือในการวิจัย

### เอกสารอ้างอิง

- [1] Hassler J.W., Purification with Activated Carbon. New York, Chemical Publish Co. Inc., 1974.
- [2] ชีวะโชติ ศรีธีระวิโรจน์ และ อัญชลีพร วาริทสวัสดิ์ หล่อทองคำ, ากรผลิตคาร์บอนกัมมันต์จากกะสามะพร้าว โดยใช้สารละลายชิงค์คลอไรด์ โชเดียมคลอไรด์ และ สารละลายผสมระทว่างสารละลายชิงค์คลอไรด์กับสารละลาย โชเดียมคลอไรด์เป็นสารกระตุ้น\*, วิศวสารอาดกระบัง. ปีที่ 16, ฉบับที่ 4, ธันวาคม, 2542.
- [3] Samuel D. F. and Osman M. A. Adsorption Processes for Water Treatment. Butterworth Publishers, 1986.
- [4] Gregg S. J. and Sing K. S. W., Adsorption, Surface Area and Porosity, 1982.
- [5] มหนัด แก้วการ, "มลของโซเดียมคลอไรด์ ซึ่งค์คลอไรด์ และก้าชคาร์บอนไดออกไซด์ต่อการผลิตถ่านกับมันต์ จากกะลามะพร้าว", วิทยานิพนร์มหาบัณฑิต ภาควิชา วิศวกรรมเคมี คณะวิศวกรรมศาสตร์ สถาบันเทคโนโลยี พระจอมเกล้าชนบุรี, 2537.
- |6| วรี จำลองราษฎร์, "การบำบัดสารอื่นทรีย์และฟืนอล ตัวยระบบเอสบีอาร์-ถ่านรังมันต์สนิดเกล็ด" วิทยานิพนธ์ มหาบัณฑิต สาชาวิชาเทคโนโลยีสิ่งแวดล้อม คณะพลังราน และวัสดุ สถาบันเทคโนโลยีพระจอมเกล้าชนบุรี, 2539.

- [7] Teng H. and Hsieh C.T., 'Influence of Surface Characteristics on Liquid-Phase Adsorption of Phenol by Activated Carbons Prepared from Bituminous Coal', Industrial Engineering Chemical Research, vol 37, pp. 3618-3624, 1998
- [8] Quantachrome Corporation Autosorb 1.

  Gas Sorption System Manual.
- [9] Hu Z. and Srinivasan M.P., 'Preparation of High-Surface Area Activated Carbons from Coconut Shell', Microporous and Mesoporous Materials, vol 27, pp. 11-18, 1999.

### QUALITY AND ENERGY EFFICIENCY IMPROVEMENT OF AN INDUSTRIAL TRAY DRYER

W. Tanthapanichakoon\*, P. Panapisal, W. Damrongsakkul

Department of Chemical Engineering, Chulalongkorn University, Payathai Road, Patumwan, Bangkok 10330 Thailand, E-mail: <a href="twiwut@chula.ac.th">twiwut@chula.ac.th</a>

### ABSTRACT

The energy efficiency of a full-scale industrial tray dryer and the uniformity of product moisture content were investigated. Because of non-uniform spatial distribution and internal circulation of hot air in the dryer, it was surmised that the final average moisture content of the products on each tray might not be uniform. First the status of the non-uniformity of the final product moisture content on each tray and the specific energy consumption of each batch were obtained by carrying out full-scale experiments under three typical drying conditions. Then simple modification on the exhaust ducts was made to improve the partial venting of highly humid air, and similar experiments were repeated to find out the effect on the level of product moisture uniformity and specific energy consumption. The simple improvement turned out to be effective in reducing not only the specific energy consumption but also the required drying time per batch. Since no significant improvement in the hot air distribution and circulation may be expected, the modification effect on the moisture uniformity was rather minor unless over-drying of the products would be allowed. Despite over-drying to obtain better moisture uniformity, the specific energy consumption after modification was still significantly reduced. The suitable hot air temperature was found to be 70 °C.

Key word: Tray Drying, Dogchews, Moisture Uniformity, Energy Efficiency

### INTRODUCTION

Dogchews are one of the promising export commodities of Thailand. The most important step in the production process is to preserve product quality by drying, which often turns out to be a bottleneck of the overall production capacity. Batch tray dryers are widely used for drying dogchews in Thailand. In addition to low drying capacity compared to the continuous dryer, one major problem found in numerous Thai factories is the high level of non-uniformity in the final product moisture content. To ensure that every piece of dogchews meets the same specified final moisture content, a higher moisture non-uniformity necessitates more over-drying of the majority of the products in the same batch. The present investigation on the full-scale dryer shows how a simple modification on the

exhaust ducts successfully reduced not only the specific energy consumption but also the required drying time per batch. Despite intentional over-drying to obtain better moisture uniformity, the specific energy consumption after modification was still significantly reduced. As expected, correct selection of the hot air temperature is quite important. A higher temperature will generally result in faster drying rates, thus reducing the specific energy consumption per batch and increasing the drying capacity. However, if the temperature is too high, it would lead to scorching of the products. The present findings should serve as useful guideline for further improvement of dogchews dryers in Thailand and perhaps elsewhere.

#### MATERIAL AND METHODS

#### RAW MATERIAL

Dogchews are made from cow rawhide, which is cleaned, digested and mixed with necessary ingredients such as binder and coloring agent. The present investigation was carried out at a factory near Bangkok, which exports a majority of the products to the USA and several European countries. One of the most popular dogchew products, namely, white- and chocolate-colored "Munchy", 9-10 mm in diameter, were used in this study. Before packaging the moisture content of the dogchews must be dried to around 15%.

#### DRYING PROCESS

In this factory drying of dogchews was carried out in tray dryers using hot air produced by two sets of electrical heaters installed on the ceiling of each batch dryer. Figure 1 shows samples of the dogchews produced in this factory. Dogchews were placed side by side on the trays (each 0.9 m x 1.95 m). The process control variable was the hot air temperature at the louver-type distributor on the inner side walls. Drying was continued until the average moisture content of dogchews fell below 15% (dry basis). The batch dryer can accommodate 9 pushcarts, 15 - 16 trays per cart, and about 160 pieces of wet dogchews per tray. In addition to the two electrical heaters, 7 circulating fans were installed on the ceiling of the dryer and 4 vent ducts, on the roof. In each drying experiment the initial and final average moisture contents of the dogchews on each tray and each pushcart were recorded. So was the total amount of electricity consumption per batch.

### RESULTS AND DISCUSSION

Table 1 summarizes the experimental results obtained before and after modification was carried out on the exhaust ducts. Table 2 shows the level of non-uniformity in the final moisture content of each batch compared to the final overall average value of the corresponding batch.

The definitions used in Table 1 are as follows:

$$X = \frac{\text{weight of water in material}}{\text{weight of bone dry material}} x 100 = \frac{\text{kg water}}{\text{kg dry material}} \%$$

Energy efficiency 
$$(\eta) = \frac{\text{Energy used for evaporating water}}{\text{Energy used for operating dryer}}$$

Specific Energy (E) =  $\frac{\text{Energy used for operating dryer}}{\text{Mass of evaporated water}}$ 



Figure 1. Samples of dogchew products

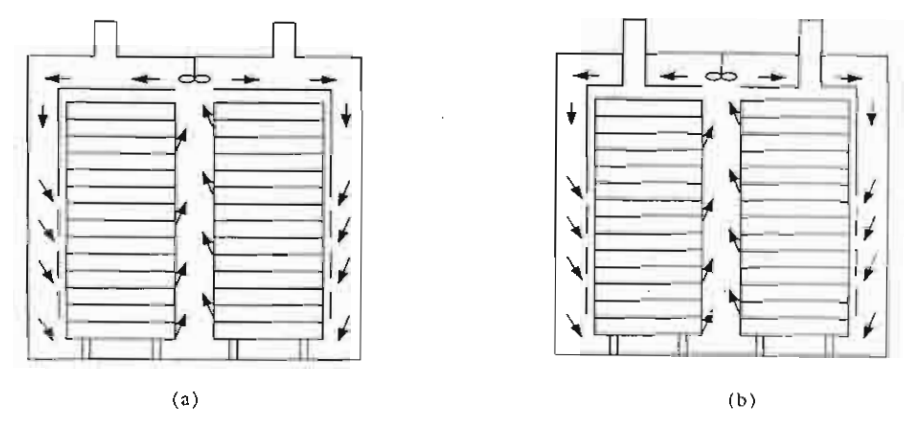


Figure 2. Cross-sectional diagram from the front view of the industrial tray dryer: (a) old dryer (b) after modification of the exhaust ducts

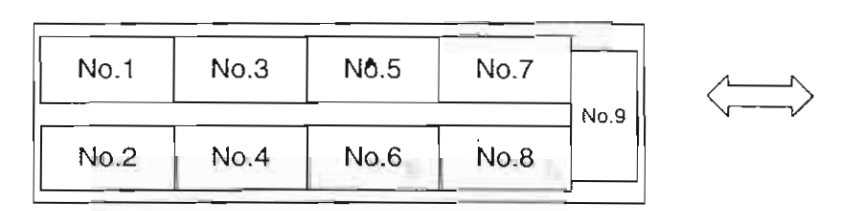


Figure 3. Layout of pushcarts in tray dryer

In Tables 1 and 2, Exp. no. 1 - 3 took place before modification of the exhaust ducts. The experimental results reveals that Exp. 3 has significantly lower specific energy consumption E and better uniformity in the product moisture content than Exp. 2. The higher E of Exp. 2 may be

attributed to the fact that both its initial and final moisture content are lower than Exp. 3, thus the former lies deeper into the falling drying rate period than the latter. It is postulated that the observed less moisture uniformity of the former may result from its large nonuniformity in the initial moisture content. When Exp. 1 and 3 are compared, we see that the former has higher specific energy consumption but better moisture uniformity than the latter. The better moisture uniformity of Exp. 1 in those trays with absolute deviations larger than 10% may be attributed to the fact that its overall product moisture content is lower than Exp. 3. The specific energy E of Exp. 1 was only slightly higher than Exp. 3 because the former used a higher setting of hot air temperature of 70°C and thus the required drying time was slightly longer despite a much higher amount of water evaporated than Exp. 3.

Table 1. Summary of Experimental Results

Dryer Type	Drying Exp. No.	Material Type	Hot Air Temperature (°C)	X <sub>1 avg</sub> (%)	X <sub>2 avg</sub>	Drying Time (br:min)	Total Energy Consumption (kWhr)	Average Rate of Evaporation (kg/hr)	Energy Efficiency n (%)	Specific Energy E(kJ/kg water)
5	1	White Munchy	70	55.84	11.47	11:50	780	39.74	41.92	5971.93
Óld Dryer	2	Choco. Munchy	60	44.25	11.88	12:00	662	32.15	40,46	6177.29
ō	3	Choco. Munchy	60	45.11	12.29	11:25	605	33.56	43.56	5684.75
ifie er	4	White Munchy	70	50.12	6.82	11:00	686	47.29	50.79	4981.04
Modifie d Dryer	5	White Munchy	70	57.13	10.51	9:50	651	47.90	54.08	4667.60

Table 2. Level of Non-uniformity in Final Moisture Content

Drying Experiment No. Percentage of trays with moisture content different from avg.	1	2	3	4	5
Between 5-10% (f <sub>1</sub> )	26.7	36.3	24.4	17.0	30.4
More than 10% (f <sub>2</sub> )	4.4	11.9	10,4	6.7	4.4

Exp. 4 and 5 were carried out after the modification. Exp. 4 has a lower E and better moisture uniformity than Exp. 5 because the final moisture content of the former is much less than the latter, thus resulting in product over-drying during the falling rate period. On the other hand, comparison of either Exp. 4 or 5 with Exp. 1, which employs the same setting of hot air temperature, conclusively shows the merit of the exhaust duct modification shown in Figure 2 in terms of energy efficiency improvement and drying time reduction. Before modification it was quite difficult to vent out part of the highly humid but heavier air. So it results in longer drying time and less energy efficiency for the same amount of water evaporated.

With respect to moisture uniformity in the products, the results before and after modification are comparable except for Exp. 4 which experienced over-drying of the products. Thus it may be postulated that the modification did not significantly improve the distribution and internal circulation of the hot air but simply facilitated the desirable partial venting of highly humid air. The arrangement of the carts in the dryer is as shown in Figure 3. Figure 4 shows the locations of trays

and pushcarts with absolute deviations in the moisture contents greater than 5% for Exp. 2 and 4, respectively. The horizontal axis represents the tray number, no. 1 being the top tray, whereas the

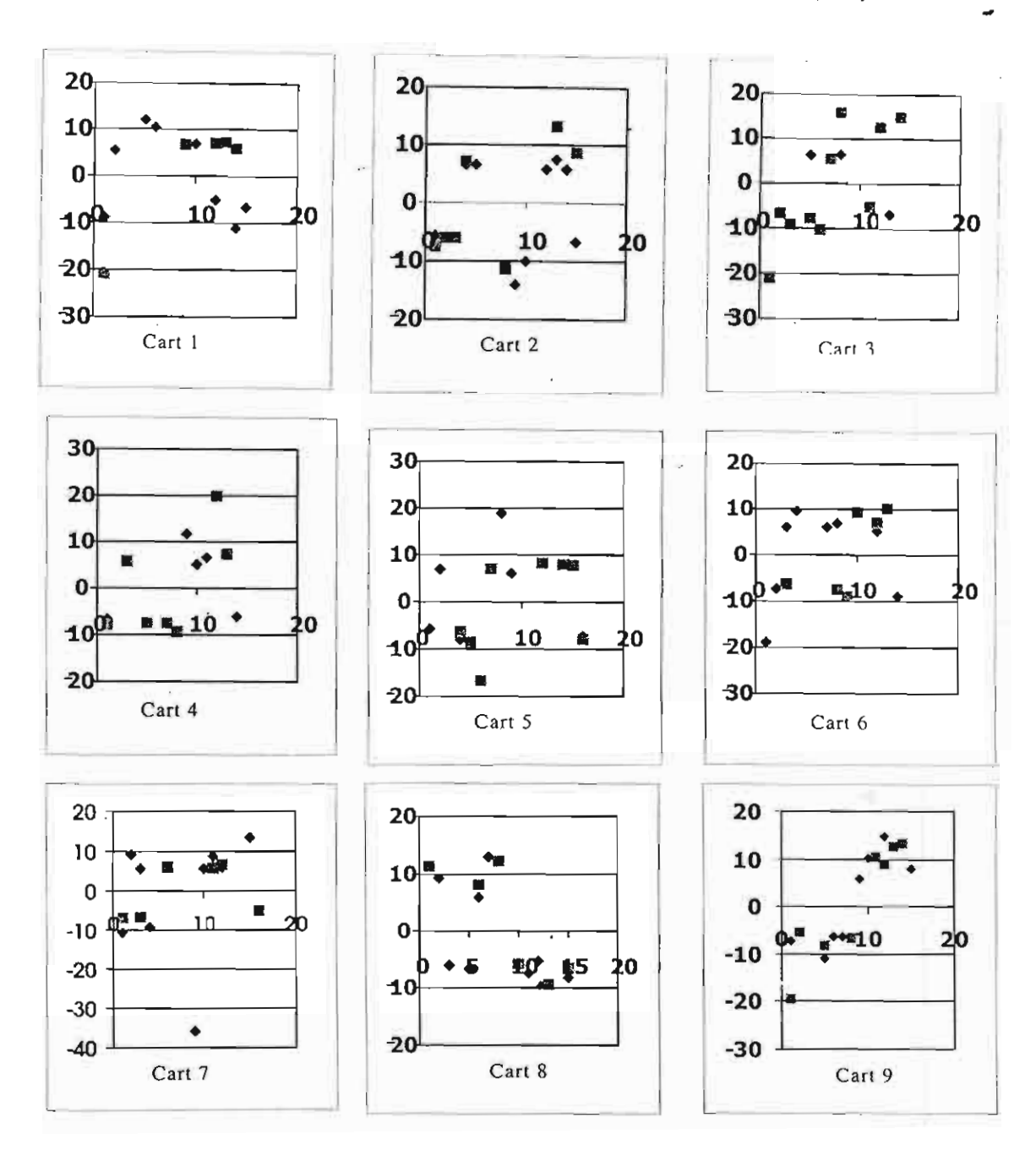


Figure 4. Comparison between Exp.2 (♠) and Exp.4 (➡) of the locations of trays exhibiting absolute deviations in final moisture content larger than 5% (Vertical axis = % moisture deviation, horizontal axis = tray no. with no.1 being on top)

vertical axis represents the observed moisture deviations, whose absolute values exceed 5%. Even though Exp. 4 yields much better moisture uniformity than Exp. 2, the clustering of the points on each eart for the two cases means that the improvement in hot air distribution and internal circulation after the modification is relatively minor.

### CONCLUSIONS

The experimental results conclusively confirm the overall merit of the simple modification on the exhaust duct. The adoption of a suitable hot air temperature of 70 °C is also advantageous. In fact, ag even higher temperature of 80 °C was tried but it ended in the scorching of the products. The major factor contributing to the higher energy efficiency and larger drying capacity is the improved partial venting of the highly humid air. Over-drying of the products generally contributes to better moisture uniformity in the dried products. However, the simple modification does not substantially improve the product moisture uniformity which mainly depends on the uniform distribution and internal circulation of hot air.

### **ACKNOWLEDGMENT**

The authors received research fund from Industrial Research Associate Support Program (IRAS) of Thailand Research Fund (TRF) while W.T. also received partial financial support from TRF Senior Research Scholar Project.

### NOTATION

X <sub>lavg</sub> average moisture content before drying	[kg water / kg dry material]
X <sub>2ave</sub> average moisture content after drying	[kg water / kg dry material]
E Specific Energy	[kl/kg water]
n Energy efficiency	7 At 1

f<sub>1</sub> Percentage of moisture content deviating between 5-10% from overall average moisture content

f<sub>2</sub> Percentage of moisture content deviating more than 10% from overall average moisture content

### LITERATURE

W. Tanthapanichakoon (2001), 2<sup>nd</sup> Progress Report "Research and Development of Continuous Dryer for Dogchews", submitted to Thailand Research Fund.

# STOCHASTIC STUDY OF AMBIENT CONCENTRATION OF PM<sub>10</sub> FUGITIVE DUST FROM STONE PROCESSING PLANTS WITH UNCERTAIN METEOROLOGICAL DATA

W. TANTHAPANICHAKOON\*, K. PHAJON-ARIPAI and T. CHARINPANITKUL

Department of Chemical Engineering, Chulalongkom-University, Phyathai Road Patumwan, Bangkok 10330, Thailand,

Keywords: Monte Carlo Simulation; PM10; Atmospheric Dispersion Model

### INTRODUCTION

Conventionally, environmental impact assessment and the efficacy of pollution control measures are simulated using past meteorological data and measurements, even though the predicted results are intended for future use. In this study, the Monte-Carlo simulation is employed to predict the degree of uncertainty in the future values of the 24-hr concentration of ambient PM<sub>10</sub> generated from stone-crushing plants using the U.S. EPA regulatory model, the ISCST3 model. Five types of metéorological inputs with uncertainty – wind direction and speed, ambient temperature, mixing height, cloudiness – are investigated to estimate the uncertainty after the introduction of dust control systems to reduce the emission rates by 80%.

### **METHODS**

First, past meteorological data are statistically analyzed to find out the proper probability distribution functions and weighting parameters. Since the ISCST3 requires hourly meteorological inputs, linear interpolation technique is employed to predict the missing values of the synoptic data of mixing height and cloudiness. Making use of statistical analysis by means of the graphical probability plot of meteorological parameters, it is found that the gamma distribution is the best representative probability distribution to describe the nature of all the past meteorological data (wind direction, wind speed, ambient temperature, mixing height, and cloudiness) and a proper value of the weighting parameter is 0.5. Next 50 random sets of stochastic variables representing 50 years of future meteorological data are generated according to the gamma distribution function. With respect to the generated meteorological inputs, it is found that the highest probability of wind direction over 1 year is in the wind sector of 135 - 180°, whereas wind speed most frequently falls in the range of 0 - 2.0 m/s. By repeating the Monte-Carlo simulations 50 times using the 50 different sets of random meteorological data, the annual stochastic nature of the ambient PM<sub>10</sub> concentration with dry deposition effect at 5 receptors is determined.

### RESULTS AND DISCUSSION

Figure 1 and Figures 2 – 3 show the map of the study area and the annual trend of statistical values of  $PM_{10}$ , respectively (Phajon-aripai, (2001)). It can be seen that, compared with other wind directions, the predominant southeastern wind direction has the most influence on the mean or expected value of the  $PM_{10}$  concentration in the study area. In addition, the high probability of the 24-hr average  $PM_{10}$  value exceeding the ambient standard (150:g/m³) can not be neglected particularly at the receptors located downwind in northwestern region. When the results at the 5 receptors are compared, it is found that the uncertainty level at receptor # 4 is higher than that at receptor # 1. Besides, by varying the weighting parameter (0.25 – 0.75) to investigate the effect of autocorrelation in the wind speed and direction on the transient behavior of the  $PM_{10}$ , it is found that the degree of autocorrelation in the wind direction has more effect than that of the wind speed, which can be attributed to the calm wind condition of the wind speed input in the study area (wind speed < 2.0 m/s).

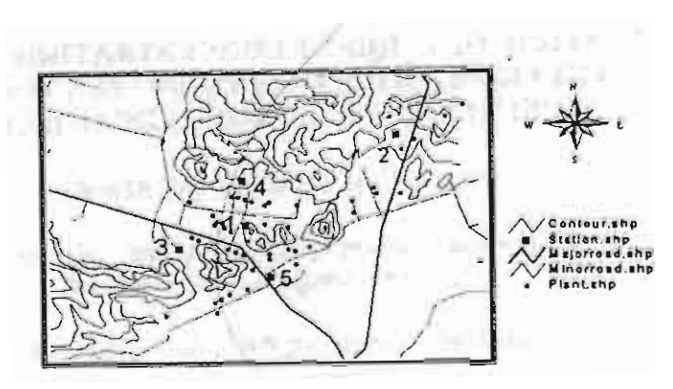


Figure 1. Map of study area with locations of stone-processing plants and receptors

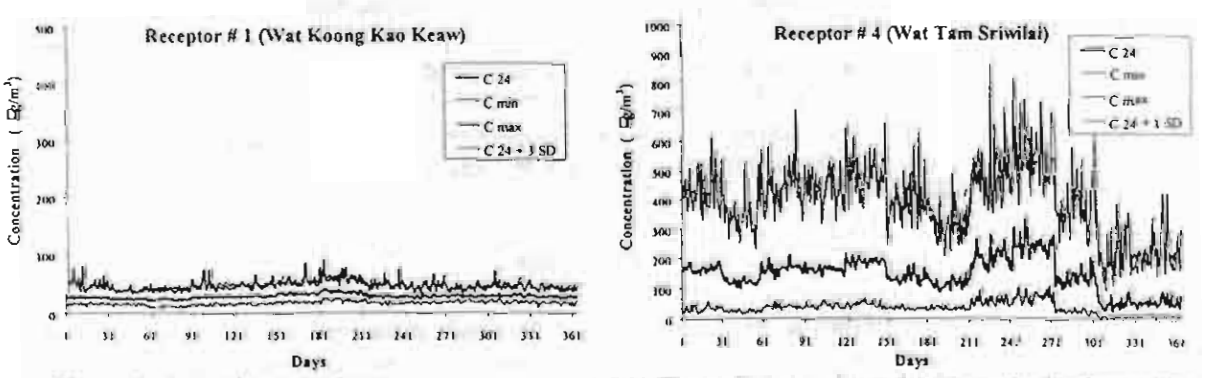


Figure 2. Annual trend of statistical values of 24-hr average concentration of PM<sub>10</sub> at receptor # 1

Figure 3. Annual trend of statistical values of 24-hr average concentration of PM<sub>10</sub> at receptor # 4

#### CONCLUSIONS

To the authors' knowledge, the present investigation using Monte-Carlo technique is the first to treat the stochastic nature of future meteorological inputs and the associated uncertainty in the predicted ambient PM<sub>10</sub>. As expected, the location of the receptor or monitoring station in combination with the prevailing meteorological data has a remarkable impact on the observed concentration and its trend. Since future meteorological data are not possible to predict accurately at the present, the Monte-Carlo simulation technique is a useful tool to estimate the level of uncertainty in the predicted concentrations after the introduction of suitable pollution control systems.

# **ACKNOWLEDGEMENT**

The authors wish to thank the Thailand Research Fund (TRF) under the Research Team Promotion Grant for financial support, Thai Meteorological Department and Pollution Control Department for the meteorological data.

#### REFERENCES

Meechumna, P. et al. (1999). Final report on Research Project submitted to Department of Mineral Resources, Ministry of Science, Technology and Environment. pp. 7-44.

Phaion-arinai, K. (2001). M.S. Thesis. Chulalongkorn University. pp. 92-97.

# ABSORPTION OF PHENOL AND ORGANIC DYES BY MESOPOROUS ACTIVATED CARBON FROM WASTE TIRE

P. Ariyadejwanich, T. Charinpanitkul, and W. Tanthapanichakoon Chulalongkom University, Bangkok 10330, Thailand

> H. Tamon, S.R. Mukai, and K. Nakagawa Kyoto University, Kyoto 606-8501, Japan

Adsorption of phenol and two organic dyes, Black 5 and Red 31, from aqueous solution on mesoporous activated carbon prepared from waste tire was carried out and, for comparison, an imported commercial activated carbon was also investigated. Phenol adsorption capacity of the prepared activated carbon was nearly equal to that of the commercial activated carbon because the micropore volumes of both carbons are almost the same. In contrast, the prepared activated carbon showed definitely higher adsorption capacities of both representative organic dyes because it had larger mesopore volume. It can be concluded that mesoporosity in the activated carbon prepared from waste tire makes it more suitable for removal of bulky molecular adsorbates from wastewater than the commercial activated carbon.

#### 1 Introduction

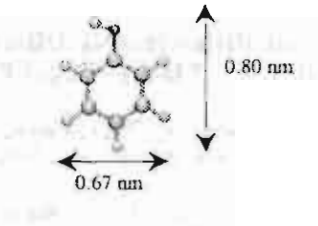
More than 330 million waste tires are discarded in each year [1] and this has become an increasingly serious waste disposal and environmental pollution problem. Several methods have been adopted to solve this severe problem, for instances, disposal in landfill sites, design of longer-life tires, recycling into new tires, or reuse in other applications, such as dock bumper, land erosion control, playground equipment etc. However, from the environmental and economical point of view, a better solution is to convert them into valuable products.

Activated carbons are widely used as adsorbents in both gas-phase and liquid-phase separation processes, and can be prepared commercially from various carbonaceous waste materials, for example, coal dust, coconut shell, wood chips, or polymer scrap, etc. [2]. In addition, it has been reported that municipal and industrial wastes can also be used as precursor in the production of activated carbons such as PET waste [3] or refuse derived fuel (RDF) [4].

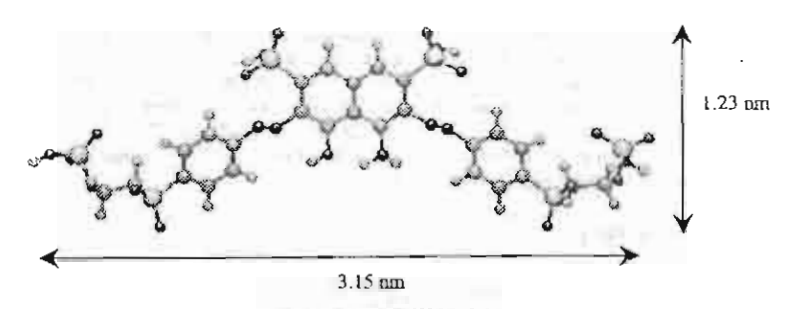
Phenol and organic dyes are often included in the wastewater from many industries. Therefore, if we can produce high-performance activated carbon from waste tires which is suitable for adsorbing these components, it can be considered as a two-fold solution to the environmental problem: transformation of waste material into pollution-cleaning adsorbent. In the present study, highly mesoporous activated carbon prepared from waste tires in our former work [5] was applied to liquid-phase adsorption of phenol and two organic dyes, Black 5 and Red 31. For comparison, a typical commercial activated carbon was also used and their adsorption isotherms were compared.

### 2 Experimental

Activated carbon treated with HCl acid prior to steam activation, called AC HCl, and a commercial activated carbon imported from the USA, called AC USA, were characterized by  $N_2$  adsorption method. Phenol (Wako Pure Chemical Industries Inc., Japan) and two organic dyes, Black 5 and Red 31 (Asia Dyestuff Industries, Thailand), were selected as adsorbates in the liquid-phase adsorption experiments. Their molecular sizes and structures, which were estimated using the WINMOPAC program, are shown in Figure 1.



a) Phenol [C<sub>6</sub>H<sub>5</sub>OH]



b) Black 5 [C26H21N5O19Na4S6]

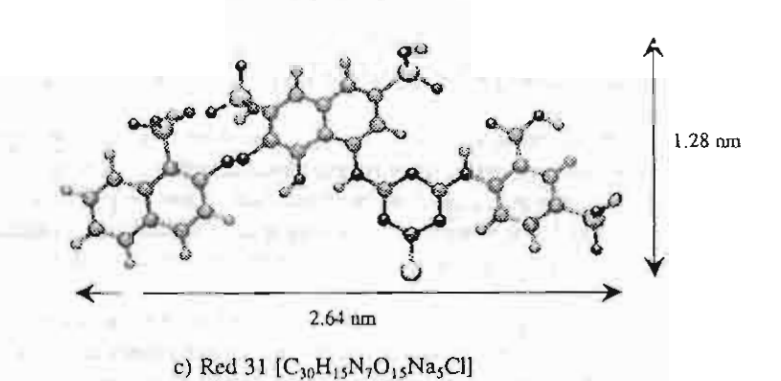


Figure 1. Molecular sizes and structures of adsorbates

For the measurement of adsorption isotherms, aqueous solutions of the required concentrations were prepared by diluting each adsorbate with distillated water. 10-200 mg of activated carbons were put into the prepared solutions of the various initial concentrations, up to 500 mg/l, and these solutions were placed in a shaking water bath at 30°C to maintain well-mixed conditions. The times to reach adsorption equilibrium determined previously were 10, 14, and 15 days for phenol, Black 5, and Red 31, respectively. After achieving the equilibrium, the solutions were filtered and their residual concentrations were measured. The initial and residual concentrations were determined by using a UV-visible spectrophotometer (UV-2200, Shimadzu Corporation, Japan) at maximum wavelengths ( $\lambda_{max}$ ) of 270, 595, and 540 nm for phenol, Black 5, and Red 31 solutions, respectively.

#### 3 Results and Discussion

The porous properties of the activated carbon prepared from waste tires and the commercial one are shown in Table 1. It is clear that the activated carbon treated with HCl prior to steam activation has significantly larger mesopore volume and slightly higher micropore volume than the commercial counterpart.

Table 1. Porous properties of activated carbons used in liquid-phase adsorption

Adsorbent	V <sub>meso</sub> (cm <sup>3</sup> /g)	V <sub>micro</sub> (cm <sup>3</sup> /g)	S <sub>BET</sub> (m <sup>2</sup> /g)
AC HCI	0.79	0.48	998
AC USA	0.24	0.39	956

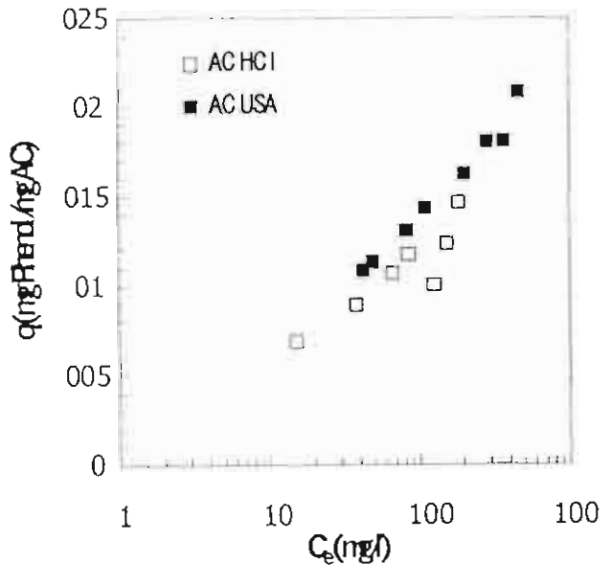


Figure 2. Adsorption isotherm of phenol on activated carbons

The phenol adsorption isotherms on both activated carbons are shown in Figure 2. It is found that phenol adsorption capacity of the present activated carbon (AC HCL) nearly equals to that of the commercial activated carbon (AC USA). Since the molecular size of phenol is smaller than the mesopore diameter (>2 nm), it may be concluded that phenol adsorption capacity depends on the more abundant microporosity.

Figures 3-4, respectively, show the Black 5 and Red 31 adsorption isotherms. As shown in Figure 1, both organic dyes have one molecular dimension larger than 2 nm, while the prepared activated carbon with higher mesopore volume showed greater adsorption capacities of both dyes than the commercial one. It may be concluded that mesoporosity plays an important role in the adsorption of large adsorbates.

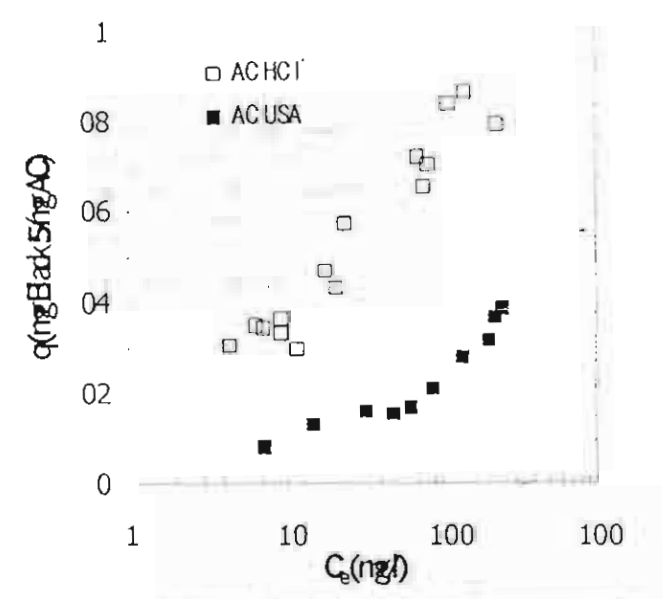


Figure 3. Adsorption isotherm of Black 5 on activated carbons

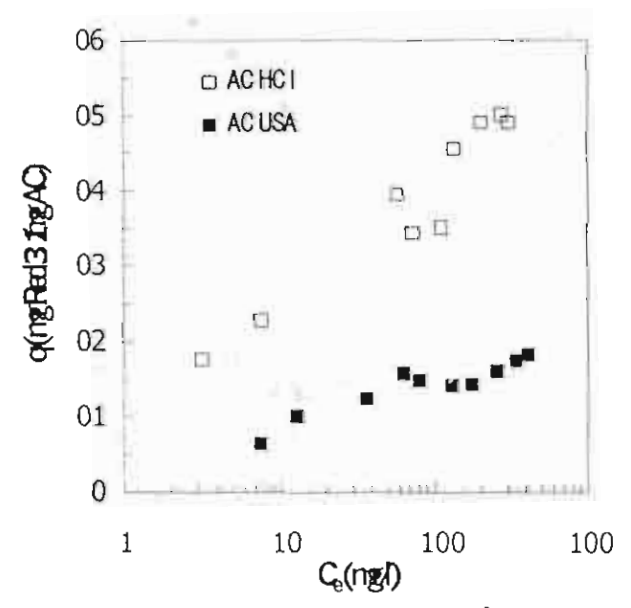


Figure 4. Adsorption isotherm of Red 31 of activated carbons

# 4 Conclusion

Highly mesoporous activated carbon prepared from waste tires by carbonization, HCl treatment, and steam activation showed the same level of phenol adsorption capacity with an imported commercial activated carbon but significantly higher adsorption capacities of both representative organic dyes. Therefore this activated carbon is more suitable for wastewater treatment, especially for adsorbing bulky molecular adsorbates.

#### 5 Acknowledgement

P. A., T. C. and W. T. respectively received full-expense Research Fellowship under Royal Golden Jubilee PhD Program and Senior Research Scholar Fund from Thailand Research Fund (TRF). H. T., S.R. M. and K. N. visited CU and carried out this collaborative research under TJTTP-JBIC Project of CU.

#### References

- Cunliffe A.M. and Williams P.T., Influence of process conditions on the rate of activation of chars derived from pyrolysis of used tires, Energy & Fuels (1999), 13(1) pp. 166-175
- Jankowska H., Swiatkowski A. and Choma J., <u>Active Carbon</u>, Ellis Horwood Limited, 1991
- Tamon H., Nakagawa K., Suzuki T. and Nagano S., Improvement of mesoporosity of activated carbons from PET by novel pre-treatment from steam activation, Carbon (1999), 37(10) pp. 1643-1645
- 4. Nagano S., Tamon H., Adzumi T., Nakagawa K. and Suzuki T., Activated carbon from municipal waste, *Carbon* (2000), 38(6) pp. 915-920
- P. Ariyadejwanich, W. Tanthapanichakoon, K. Nakagawa, S.R. Mukai and H. Tamon, Preparation and characterization of mesoporous activated carbon from waste tires, Carbon (2003), 41(1) pp. 157-164

# High-Temperature Removal of Acetaldehyde in a Corona Discharge Reactor

# WIWUT TANTHAPANICHAKOON\*, TAWATCHAI CHARINPANITKUL AND JINTAWAT CHAICHANAWONG

Department of Chemical Engineering, Chulalongkorn University Payathai Road, Pathumwan, Bangkok 10330 Thailand E-mail: fchwtt@eng.chula.ac.th

#### NORIAKI SANO

Department of Chemical Engineering, Himeji Institute of Technology 2167 Shosha, Himeji, Hyogo 671-2201, Japan

#### HAJIME TAMON

Department of Chemical Engineering, Kyoto University Yoshida-Honmachi, Sakyo-ku, Kyoto 606-8501, Japan.

Acetaldehyde is one of the malodorous gaseous components emitted at high temperature from a crematory furnace. In this study a corona discharge reactor is employed to remove acetaldehyde (CH<sub>3</sub>CHO) from N<sub>2</sub> and air from room temperature up to 300 °C. First the effect of acetaldehyde inlet concentration (200,400 and 600 ppm) is investigated. In contrast to conventional separation processes, the more dilute the inlet concentration, the higher the removal efficiency becomes because, when the discharged current is kept constant, the number ratio of discharge electrons to acetaldehyde molecules increases. Next the effect of oxygen and/or water vapor in the emission gas is investigated. Interestingly the presence of either oxygen or water vapor always enhances the removal of acetaldehyde from N<sub>2</sub>. When the reaction temperature is increased, the removal efficiency is found to increase starting from room temperature up to 200 °C, above which the tendency reverses up to 300 °C. It is found that the smallest discharge current required for complete removal of 600 ppm of acetaldehyde from the air is only 0.2 mA at room temperature. To elucidate the effect of temperature, the discharge current is deliberately set at 0.05 mA in some experiments.

#### 1 Introduction

Air pollution is an important public issue in Thailand. One major cause of air pollution is the emission of toxic and malodorous gases from many sources such as industrial plants and automobile. Recently, a latent source of public nuisance has become prominent. It is the emission of gases and particulate from the crematory furnace in a temple. There are nearly 23,000 temples in Thailand. The majority of them have crematory furnaces, most of which release the exhaust gas from the stacks to the atmosphere without any effective treatment. Although the concentration levels of malodorous gases are very low in the ppm or ppb orders, they not only pose serious public nuisance but may also be detrimental to public health. Only a few rich temples in Bangkok have installed furnaces with efficient after-burning systems to decompose the malodorous organic gaseous components. The outlet gas temperature from a well-operated furnace may be as high as 800~900 °C whereas the stack temperature may range from 150~300 °C.

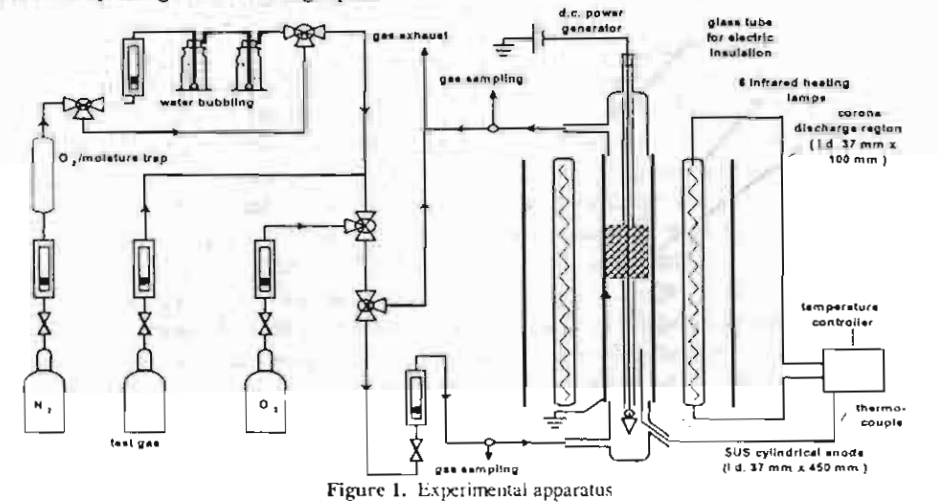
In 1995, a novel gas purification method using electron attachment was proposed [1]. The gas impurities are ionized by collisions with electrons produced, for example, in a corona discharge between a wire cathode and a cylindrical anode. The resulting negative ions drift to the anode and deposit on it. Previous studies have revealed that gases of high electron affinity, for example sulfur compounds, halogens, malodorous gases, VOCs and CFCs are selectively removed by the proposed method [1-8]. Though acetaldehyde is emitted at high temperature from a crematory furnace, there is insufficient report on the

effect of high temperature [9-11]. In this study a corona discharge reactor is employed to remove acetaldehyde (CH<sub>3</sub>CHO) from N<sub>2</sub> and air from room temperature up to 300 °C.

#### 2 Experimental Setup

Figure 1 shows a schematic diagram of the experimental apparatus. The deposition-type reactor consists of a SUS pipe, 3.7 cm inner diameter and 80 cm length, as the anode. The cathode is a 0.5-mm stainless-steel wire suspended from a silicone plug at the top of the reactor and straightened along the axis of the vertical anode by a small weight. A highvoltage DC generator (Matsusada, HAR-30N5) is utilized to supply a steady stream of low-energy electrons to the corona-discharge reactor. To control the reactor temperature, 6 infrared heating lamps (200V, 700W each) are installed lengthwise around the outside perimeter of the reactor. The temperature control unit consists of a temperature controller (FENWAL, AR-24L) and a thyrister power regulator (Shimaden, PAC15C003081-NO). The desired concentrations of acetaldehyde and coexisting oxygen are adjusted by diluting standard gases with pure nitrogen. The inlet concentrations of acetaldehyde investigated are 200, 400 and 600 ppm. Similarly, the concentrations of coexisting O2 and H<sub>2</sub>O are varied from 0-20% and 0-23000 ppm, respectively. Inlet and outlet concentrations of acetaldeliyde are analyzed using a gas chromatograph (Shimadzu Corp., GC 9A) equipped with a flame ionization detector (FID). The concentration of byproduct ozone is separately detected with appropriate gas detector tubes (GASTEC Co., Ltd. and Kitagawa Co., Ltd.).

The inlet concentrations of acetaldehyde are deliberately set higher than their reported values of ca. 4 ppm in crematory emission for two reasons. First, our present and previous investigations have conclusively shown that, as the inlet concentration of an impurity gas rises, its removal efficiency always drops because the ratio of its absolute number of molecules to the number of discharged electrons decreases. Thus the experimental results represent conservative values. Second, if the concentration is too low (a few ppm order or less), there will be high uncertainty in the measurement values obtained by the gas chromatographs.



#### 3 Results and Discussion

# 3.1 Definitions of removal efficiency

To exclude any possible effect of adsorption at low temperature and thermal decomposition at high temperature, the removal efficiency  $\psi$  is defined as Eq.1

$$\psi = \frac{(C_{out,0 mA} - C_{out,any mA})}{C_{out,0 mA}} \quad [-] \quad (1)$$

Here,  $C_{out,0\,mA}$  (ppm) and  $C_{out,\,mn\,mA}$  (ppm) are the outlet concentrations of the impurity gas without and with discharge current.

The removal efficiency per unit residence time,  $\psi'$ , in Eq. 2 takes into account the actual shorter residence time of the hot gas in the reactor even though the inlet gas flow rate (mole basis) remains unchanged before and after the reactor temperature is elevated.

$$\psi' = \frac{\psi \times residence \ time \ at \ 25^{-0}C}{residence \ time \ at \ T^{-0}C} \quad [-]$$
 (2)

At steady state, the equation of continuity requires that  $\rho_1 \langle \upsilon_1 \rangle A_1 = \rho_2 \langle \upsilon_2 \rangle A_2$ . Since  $A_1 = A_2$  and  $\rho$  is a function of the gas temperature, the gas velocity at an elevated temperature  $T_2$  will be faster than its velocity at room temperature  $T_1$ . Thus the mean residence time  $\theta_2 = \frac{V}{\langle \upsilon_2 \rangle A_2}$  of this gas at  $T_2$  is shorter than  $\theta_1 = \frac{V}{\langle \upsilon_1 \rangle A_1}$  at room temperature. Here V is the effective volume of the reactor.

#### 3.2 Effect of temperature and inlet concentration on the removal of acetaldehyde from N2

Figure 2 shows the two kinds of the removal efficiency of acetaldehyde from pure  $N_2$  at elevated temperatures. From Figure 2(a), we see that, as the temperature increase, the removal efficiency  $\psi$  decreases starting from room temperature up to 200 °C, and then the tendency reverses up to 300 °C. Figure 2(b) reveals that when the negative effect of reduced resident time is taken in account, the value of  $\psi'$  increases with temperature up to 150 °C. Tamon et al.[1] have found that the removal efficiency via electron attachment tends to decrease when the inlet concentration is increased. As expected, the present experimental results also exhibit the same tendency. The more dilute the inlet concentration, the higher the removal efficiency becomes because, when the discharged current is kept constant, the number ratio of the discharge electrons to the acetaldehyde molecules increases.

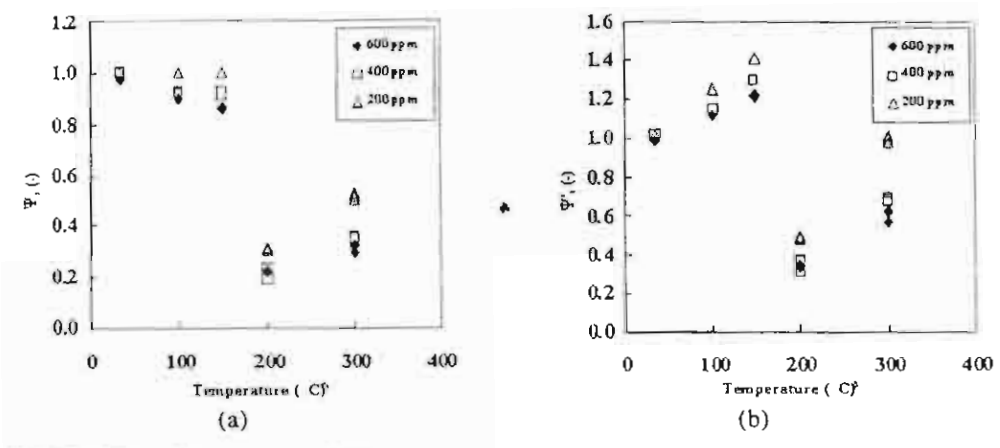


Figure 2. Effect of temperature and inlet concentration on the removal of acetaldehyde from  $N_2$ ; I=0.2 inA. SV=55.8 hr  $^{1}$  at room temperature.

# 3.3 Effect of coexisting O2 and water vapor on the removal of acetaldehyde from N2

Experiments were carried out to observe the combined effect of  $O_2$  and  $H_2O$  on the removal of acetaldehyde from  $N_2$ . Figure 3 shows the two types of the removal efficiency  $\psi$  and  $\psi'$  of acetaldehyde from  $N_2$ - $O_2$  at various concentrations of water vapor. It is found that the presence of either oxygen or water vapor always enhances the removal of acetaldehyde from  $N_2$ . When the reaction temperature is increased, the removal efficiency is found to increase starting from room temperature up to 200 °C, above which the tendency reverses up to 300 °C because less ozone is generated from  $O_2$  as temperature increases. As for the effect of  $H_2O$ , the presence of  $H_2O$  slightly retards the removal efficiency of acetaldehyde from  $N_2$ - $O_2(20\%)$  from room temperature to 300 °C because at low discharge current, the relatively much smaller number of electrons tend to attach mostly to  $H_2O$ . In addition, it is found that the smallest discharge current required for complete removal of 600 ppm of acetaldehyde from the air is only 0.2 mA at room temperature.

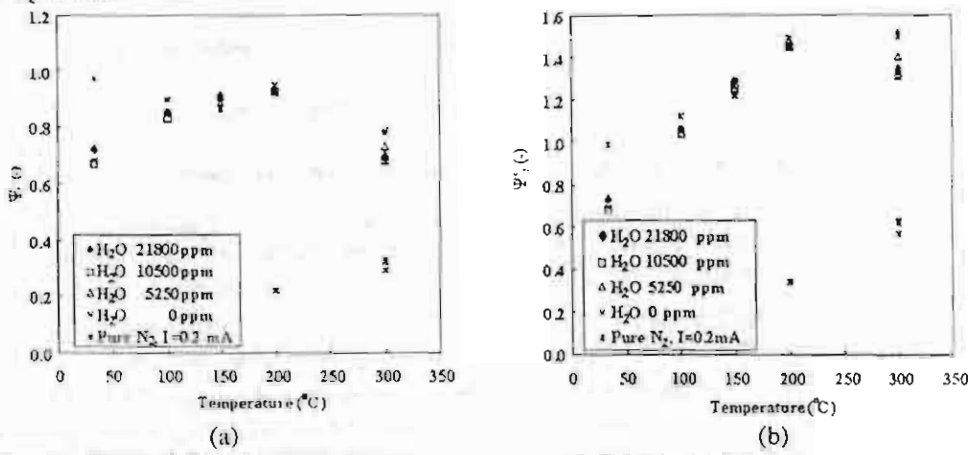


Figure 3. Combined effect of oxygen and water vapor on the removal efficiency of acetaldehyde from N<sub>2</sub> at 20% O<sub>2</sub>; [acetaldehyde]= 600 ppm, I=0.05 mA, SV=55.8 hr<sup>-1</sup> at room temperature

# 4 Conclusion

High-temperature removal of acetaldehyde in a corona discharge reactor was investigated. As expected, the more dilute the inlet concentration, the higher the removal efficiency becomes because, when the discharged current is kept constant, the number ratio of the discharge electrons to the acetaldehyde molecules increases. The presence of either oxygen or water vapor always enhances the removal of acetaldehyde from N<sub>2</sub> because of the ozone effect. In addition, it is found that the smallest discharge current required for complete removal of 600 ppm of acetaldehyde from the air is only 0.2 mA at room temperature.

# 5 Acknowledgement

W.T., T.C., and J.C. received research grant and financial support from Thailand Research Fund (High-Temperature Removal of Low-Concentration Multi-Component Air Pollutant Gases Using Electron Attachment Reaction Project and Team Research Buildup Program). H.T. and N.S. received support from TJTTP-JBIC Project of Chulalongkorn University to carry out research collaboration at C.U.

#### Notation

C = concentration, ppm

 $\psi$  = removal efficiency excluding adsorption and thermal decomposition effect, (-)

 $\psi'$  = removal efficiency per unit residence time, (-)

SV = space velocity, hr<sup>-1</sup>

 $\theta$  = mean residence time, (min)

V = effective volume of the corona discharge reactor, (ml)

 $A = \text{cross sectional area, (cm}^2)$ 

 $\langle v \rangle$  = superficial velocity, (m/s)

#### Subscript

out, 0 mA = outlet of reactor at zero discharge current

out, any mA = outlet of reactor at non-zero current

#### References

- 1. Tamon H., Mizota H., Sano N., Schulze S. and Okazaki M. "New concept of gas purification by electron attachment," AIChE J., 41, 1701-1711 (1995).
- Sano N., Nagamoto T., Tamon H., and Okazaki M. "Removal Iodine and Methyl Iodide in Gas by Wetted-Wall Reactor based on Selective Electron Attachment," J. Chem. Eng. Japan., 29, 59-64 (1996)
- 3. Sano N., Development of Gas Purification Technology by Selective Electron Attachment, *Ph.D.*, *Diss.*, Kyoto Univ., Japan (1997a).
- Sano N., Nagamoto T., Tamon H., Suzuki T., and Okazaki M., Removal of Acetaldehyde and Skatole in Gas by Corona-Discharge, Ind. Eng. Chem. Res., 36, 3783-3791(1997b).
- 5. Sano N., Tanion H., and Okazaki M., Removal of the Chlorofluorocarbon 1,1,2-Trichloro-1,2,2-trifluoroethane in Gas by a Corona-Discharge Reactor, *Ind. Eng. Chem. Res.*, 37, 1428(1998).
- 6. Tamon H., Sano N. and Okazaki M., Influence of Oxygen and Water Vapor on Removal of Sulfur Compounds by Selective Electron Attachment, AICHE J., 42, 1481-1486(1996).
- Tamon H., Imanaka H., Sano N., Okazaki M., Tanthapanichakoon W., Removal of Aromatic Compounds in Gas by Electron Attachment, Ind. Eng. Chem. Res., 37, 2770-2774(1998).
- Tanthapanichakoon W., Larpsuriyakul K., Charinpanitkul T., Sano N., Tamon H., and Okazaki M., Effect of structure of corona-discharge reactor on removal of dilute gaseous pollutants using selective electron attachment, J. Chem. Eng. Japan., 31, 7-13 (1998).
- Nishida, K. and Matsuda Y. Malodor of exhaust gas from crematory. J. Odor Control, 1981, 1-11 (in Japanese).
- Nishida, K., Malodor at Cremation Facility (Part I), PPM, 1988, 3, 49-58 (in Japanese).
- 11. Nishida, K. Malodor at Cremation Facility (Part II), PPM, 1988, 4, 51-59 (in Japanese).

# REMOVAL OF TOLUENE FROM AIR BY CORONA DISCHARGE REACTOR AT HIGH TEMPERATURE: INFLUENCE OF ELECTRIC FIELD STRENGTH

N. SANO<sup>1</sup>, W. TANTHAPANICHAKOON<sup>2</sup>, T. CHARINPANITKUL<sup>2</sup>, N. DATTAVORN<sup>2</sup>, S. CHAIYO<sup>2</sup>, AND H. TAMON<sup>3</sup>

Dept. of Chemical Eng., Himeji Institute of Technology, 2167 Shosha, Himeji, 671-2201, Japan E-mail: sano@mech.e.g.himeji-tech.ac.jp

<sup>2</sup> Dept. of Chemical Eng., Chulalongkorn University, Patumwan, Bangkok 10330, Thailand <sup>3</sup> Dept. of Chemical Eng., Kyoto University, Kyoto 606-8501, Japan

A cylindrical d.c. corona discharge reactor was used to remove toluene from air. Using this reactor, the effect of electric field strength was investigated varying wire-cathode diameters in the elevated temperature which range from room temperature to 400 °C. Electron energy depends on wire cathode diameters and gas temperature. When a thicker cathode was used, the required voltage to generate corona discharge increases. This voltage increase causes the higher electron energy. Also, when temperature is elevated, the accompanying gas expansion results in an increase at electron energy because the collision frequency of electron with gas molecules decreases. However, the gas expansion by temperature elevation causes the less resident time of the treated gas in the reactor. The experimental results show that in all temperature range examined here the removal efficiency is higher when the thicker wire-cathode is used at a constant current. When the removal efficiency based on consumed electric energy is considered, this energetic efficiency becomes higher when temperature is elevated.

#### 1 Introduction

Recently, there are considerable numbers of reports about application of discharge technologies to gas purification because such techniques are considered to be powerful methods to remove diluted contaminants in gas. There are several types of electrical discharges for gas purification such as, d.c. corona discharge [8, 6], pulsed corona discharge [4], surface discharge [5], and electron beam [1]. We have been developing d. c. corona discharge reactor because we consider this method good in terms of low byproduct formation from lower electron energy inside the reactor than other methods.

As the probability of electron attachment and related reactions depend on electron energy [2, 3], the removal efficiency depends on electrode shape which affect on electric field strength inside the reactor. For the industrial application, it is important to know the influence of temperature, especially high temperature range, because the temperature of treated gas in many cases is very high, for example combustion exhaust gases. Therefore, it is necessary to examine the effects of electrode shape and temperature on the efficiency for removing gas components by corona discharge reactor.

# 2 Experimental

Figure 1 shows the experimental set up. Carrier gas to the reactor,  $N_2$ - $O_2$  mixture ( $[O_2]$ =20%), was supplied from gas cylinders. Toluene ( $C_6H_3CH_3$ ) vapor was mixed into this carrier gas by bubbling with the liquid toluene whose temperature was

controlled at 1.7 °C. The corona-discharge reactor consists of a cylindrical anode (stainless steel cylinder of 37mm inner diameter and 800mm length) and a wire cathode stretched in the center. Three cathodes of different diameters, 0.3, 0.5, and 0.9 mm, were used to investigate the influence of electron energy. The reactor was heated up to 400 °C by six 750W infra red lamps around the anode. Pulseless high voltage of negative polarity was applied on the cathode, and the anode was grounded. The voltages to generate 0.5 mA in the removal of 2000 ppm C<sub>5</sub>H<sub>5</sub>CH<sub>3</sub> from N<sub>2</sub>-O<sub>2</sub> (20%) mixture using cathode diameters, 0.3, 0.5, and 0.9 mm were respectively 14.8, 15.3, and 17.0 kV at room temperature, and these voltages decreased with temperature down to respectively 4.1, 5.9 and 6.4 kV at 400°C. The gas analysis from the reactor inlet and outlet was carried out by gas chromatograph with FID detector (Shimadzu, GC9A).

#### 3 Results and Discussion

# 3.1 Influence of cathode diameter and temperature on electron energy

The voltage required to generate corona discharge was changed by using the different cathode diameters. It causes the change of the electric field strength, E, inside the reactor. Also, the gas temperature affects the gas density, N. It is important to notice that the electron energy depends on the electric field strength divided by gas density, E/N. E positively affects the electron energy because the electrons emitted by the corona discharge are accelerated by E. On the other hand, N negatively affects the electron energy because the frequency of the collisions between electrons and gas molecules becomes higher if N becomes higher. To approximate E/N, the electric field strength described as Eq. 1 [10] is used.

$$E = V / \{ r \ln (R/R_o) \}$$
 (1)

V, r, R,  $R_o$  are voltage, distance from center in the cylindrical reactor, inner radius of the cylindrical anode, radius of the wire cathode, respectively. Thus, the mean E/N is approximated by Eq. 2.

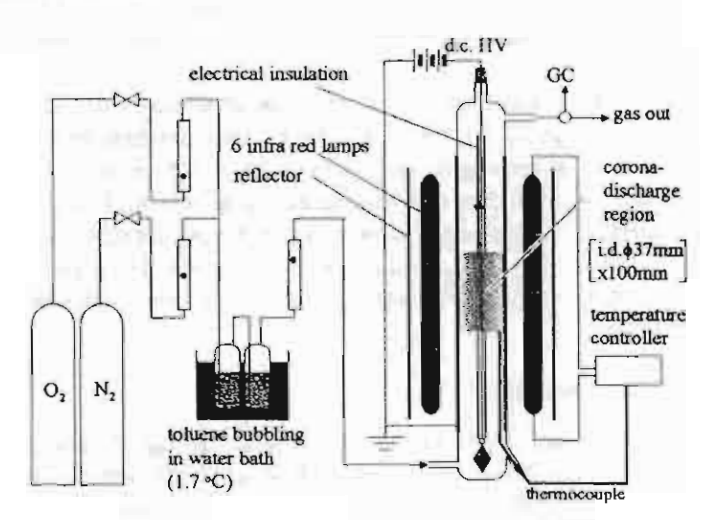


Figure 1. Experimental set up.

$$\langle E/N \rangle = \frac{\int_{R_o}^{R} (2\pi r)(E/N) dr}{\pi (R^2 - R_o^2)} = \frac{2V}{N(R + R_o) \ln (R/R_o)}$$
(2)

N is calculated by  $p/\{R(273+7)\}$ , where p, R, T are pressure, gas constant, and gas temperature, respectively. Figure 2 shows  $\langle E/\bar{N} \rangle$  against T when three cathode diameters were used in  $N_2$ - $O_2$  mixture. In these figures, it is shown that  $\langle E/N \rangle$  becomes higher when a thicker cathode is used, which is consistent with the previous report [10]. From this result, electron energy in the corona discharge is expected to be higher when a thicker cathode is used. As for the temperature dependence of  $\langle E/N \rangle$ , one can notice a tendency that  $\langle E/N \rangle$  decreases with temperature gradually. This is caused by the decrease of voltage induced by the temperature elevation.

# 3.2 Influence of cathode diameter and temperature on removal efficiency

The removal efficiency is defined by Eq. 3 based on the decrease of C<sub>6</sub>H<sub>5</sub>CH<sub>3</sub> concentration at the reactor outlet.

$$\Psi = (C_0 - C_i)/C_1 \tag{3}$$

 $\Psi$ ,  $C_0$ , and  $C_1$  are removal efficiency,  $C_6H_3CH_3$  concentration at the reactor outlet without discharge current, and that with discharge current, respectively. The discharge current applied in this study was 0.5 mA.  $\Psi$  obtained from the varied cathode diameters and temperatures in  $N_2$ - $O_2$  mixture are shown in Fig. 3. In these figures, there is a tendency that  $\Psi$  increases with the cathode diameter. This tendency is consistent with the reports on the removal of  $CH_3CHO$ ,  $CH_3I$ , and  $C_2F_3CI_3$  at room temperature [10]. In Figs. 3, it is found that this tendency is kept through out the temperature range, from room temperature to 400 °C.

As for the temperature effect on constant cathode diameter, it is found in Figs. 4 that  $\Psi$  decreases with temperature in relatively low temperature range. To consider

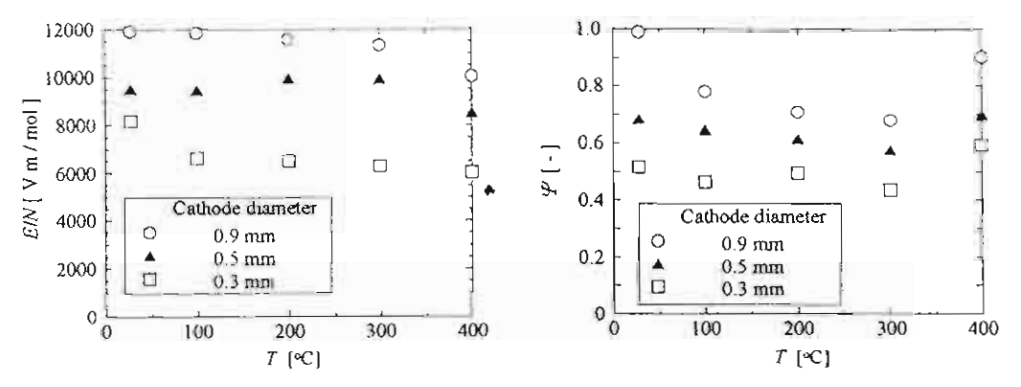


Figure 2. E/N for removal of C<sub>5</sub>H<sub>5</sub>CH<sub>3</sub> from N<sub>2</sub>-O<sub>2</sub> mixture:  $[O_2]$ =20%, I = 0.5 mA, Q = 1.67 x 10<sup>-6</sup> m<sup>3</sup>/s,  $C_{\text{in}}$  = 2000 ppm

Figure 3. Removal efficiency of C<sub>5</sub>H<sub>5</sub>CH<sub>3</sub> from N<sub>2</sub>-O<sub>2</sub> mixture:  $\{O_2\}$ =20%, I= 0.5 mA, Q= 1.67 x 10<sup>-6</sup> m<sup>3</sup>/s,  $C_{10}$ = 2000 ppm

this reason, it should be noted that the residence time of the gas flow in the reaction zone depends on the gas temperature because the molar gas volume expands when temperature increases. Therefore, the decrease of  $\Psi$  with T in low temperature range is caused by the decrease of the gas residence time. On the other hand, in the high temperature range above 300 °C,  $\Psi$  increases with T significantly. It means that the effect of high temperature to enhance the reactivity of discharged electrons and related reactive radicals with  $C_6H_5CH_3$  molecules is much more significant than the effect of gas expansion by temperature elevation. A previous article indicated that the corona discharge reactor has several reactions such as (1) electron attachment reactions, (2) dissociation by electron impact, (3) ions cluster formation, (4) radical reactions, (5)  $O_3$  reaction [6-10]. Among these reactions, ion cluster formation and  $O_3$  reaction would be negligible in the high temperature range because ions clusters and  $O_3$  are thought to be unstable at high temperature condition. In fact, our measurement of  $O_3$  concentration from our reactor revealed that  $O_3$  was produced up to 1370 ppm at room temperature, and it decreased down to negligible level when T was 300 °C.

# 3.3 Influence of cathode diameter and temperature on energetic efficiency

Even if we have obtained the information that the higher electron energy by use of thicker cathode improves the removal efficiency at a constant current, the higher electric powder is required for the thicker cathode because the voltage increases with the cathode diameter to generate a required current. Thus, to design the reactor for industrial applications, it is important to know the energetic efficiency. To show the energetic efficiency J, the mole number of the removed C<sub>6</sub>H<sub>3</sub>CH<sub>3</sub> by a unit energy, is shown in Figs. 4. J is calculated by Eq. 4.

$$J = (q_{\rm in} - q_{\rm out}) / (I V) \tag{4}$$

 $q_{\rm in}$ ,  $q_{\rm out}$ , I, V are the molar flow rate of  $C_6H_5CH_3$  at the reactor inlet, that at the reactor outlet, the discharge current, and the applied voltage, respectively. Here a tendency is found under some conditions that J increases with the cathode diameter. However, this tendency is not so clear as shown in Fig. 3. As for the temperature dependence on J, it is found that J increases with T with all examined cathode diameters.

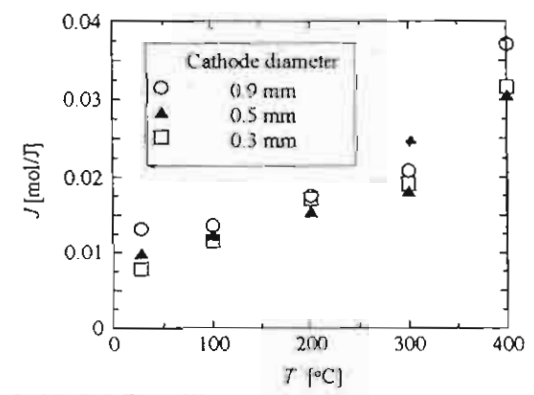


Figure 4. Energetic efficiency for removal of C5H5CH3 from N2-O2 mixture:  $[O_2]=20\%$ , I=0.5 mA,  $Q=1.67 \times 10^{-6}$  m<sup>3</sup>/s,  $C_{in}=2000$  ppm

From this result, high temperature can be recommended for higher J when gas can be heated up easily, such as in cogeneration systems, where exhausted heat from other unit is available. Also, if the temperature of the target gas is initially high, it is recommended to keep its temperature so high as 400 °C, so that J is kept high. As for the effect of cathode diameter, a thicker cathode is recommended in room temperature, with which J is clearly higher with thicker cathode. When temperature is relatively high, this tendency is not so clear. In such case, one can consider the stability of corona discharge to choose cathode diameter. Since an excessive current often causes electric breakdown inducing spark, it is sometimes better to control the current within a low value as possible. In such a case, the use of thicker cathode can be recommended.

#### 4 Conclusions

The experiments to remove  $C_6H_3CH_3$  from  $N_2$ - $O_2$  mixture were performed using d.c. corona discharge reactor with three different cathode diameters in the temperature range from room temperature to 400 °C. When a thicker cathode was used, the higher electron energy was expected because E/N became higher. As results, it was observed that the removal efficiency became higher when thicker cathode was used at constant current. When temperature is elevated, the efficiency decreases with temperature in the temperature range below 100 °C because of the gas expansion. However, this tendency was reversed in the range above 300 °C for the increase of reactivity of electrons and radicals with  $C_6H_3CH_3$ . In addition, energetic efficiency was obtained, resulting that this efficiency increased with temperature with all cathode diameters.

#### 5 Acknowledgement

This work received a grant from Thailand Research Fund (New Knowledge Generation Grant 2000 - 2002). W. T. and T. C. also received TRF-RTA Fund, whereas N. S. and H. T. visited Chulalongkorn University under Thailand-Japan Technology Transfer Project (TJTTP-OECF) financed by Japan Bank for International Cooperation (JBIC) (former Overseas Economic Cooperation Fund, Japan (OECF)).

#### Literature Cited

- 1. Kawamura K.; Kagaku Kogaku, 53 (1989) pp. 820-821.
- 2. Massay, S. H.; Negative Ions, Cambridge Univ. Press, Cambridge, England (1976)
- 3. Massay, S. H.; Atomic and Molecular Collisions, Taylor & Francis, London (1979)
- 4. Masuda S Proc. 8th Int. Symp. On Plasma Chemistry, Tokyo, Japan (1987) pp. 2187-2192.
- Masuda S., et al.; Proc. Int. Conf. on Electrostatic Precipitation, Padova, Italy (1987) pp.667-676.
- 6. Sano, N., Nagamoto T., Tamon H. and Okazaki M. J. Chem. Eng. Jpn., 29 (1996) pp.59-64.
- Sano N., Nagamoto T., Tamon H., Suzuki T., Okazaki M. I. E. C. Res., 36 (1997) pp. 3783-3791.
- Tamon H., Mizota H., Sano N., Schulze S. and Okazaki M. AIChE J., 41 (1995) pp.1701-1711.
- Tamon H., N. Sano and M. Okazaki; AIChE J., 42 (1996) pp. 1481-1486.
- Tanthapanichakoon W., Larpsuriyakul K., Charinpanitkul T., Sano N., Tamon H. and Okazaki M., J. Chem. Eng. Jpn., 31 (1998) pp.7-13.

# Effectiveness of Dust Emission Control on Ambient Air Quality in Stone Processing Zone in Saraburi Province

P. Vijitjaroenmuang, T. Charinpanitkul, and W. Tanthapanichakoon

Chulalongkorn University, Bangkok 10330, Thailand

Y. Takemoto

Yokkaichi University, Yokkaichi, 512-8512, Japan

Located about 110 km north of Bangkok, Saraburi Province is often afflicted by severe particulate pollution episodes during the winter season because more than 45 stone processing plants are concentrated in a zone of complex terrain of ca.25 sq. km. Therefore the government of Thailand has initiated a comprehensive plan to reduce by 80% the fugitive dust emission from the stone processing plants and mining sites. In this study an atmospheric dispersion model using terrain-fitting generalized coordinates is used to predict the ambient PM<sub>10</sub> concentrations at various ground-level receptors. First, simulations are carried out using historical meteorological data to confirm the suitability of the model parameters and to grasp the situation before the implementation of dust control. Next the model is employed to predict the ambient PM<sub>10</sub> after dust control implementation for various wind directions and speeds under stable and unstable atmospheric conditions. The simulation results reveal that, as the atmospheric condition becomes more stable (as the effective vertical dispersion coefficient decreases from 10 to 1 m<sup>2</sup>s<sup>-1</sup>), the corresponding 24-hour average PM<sub>10</sub> can increase up to 8 folds at some receptors. In either condition, the 24-hour PM<sub>10</sub> does not exceed the air quality standard at any of the 11 receptors in a typical week.

#### 1. Introduction

Due to rapid expansion of the construction industry in the 1990s, production capacity of processed stone from more than 45 plants in Saraburi province alone has climbed to a maximum of ca. 25 million cubic meters (62.5 million tons per year). Consequently, fugitive particulate matter from these stone processing plants posed serious air pollution problem and affected people living in and around this zone. PM<sub>10</sub> concentration in this zone was sometimes as high as 0.5 mg/m<sup>3</sup>, 4 times over Thailand air quality standard of 0.120 mg/m<sup>3</sup> [1]. The Thai government recognized the severity of this problem, so it announced comprehensive measures to improve air quality in this area and set a target to reduce by 80% the fugitive dust emission from all stone processing plants and mining sites. In order to evaluate the effectiveness of respirable dust pollution control, a grasp of the air quality situation before and after the implementation is required. However, exhaustive field studies in the preliminary stage are quite costly and time consuming, and the obtained results are not generally transferable to other location nor amenable to prediction of future condition. Therefore a dispersion model using generalized coordinates [2] is utilized here to predict PM<sub>10</sub> concentration at various ground-level receptors both before and after implementation of dust pollution control. The predicted PM<sub>10</sub> concentrations in this complex terrain area are useful for the evaluation of the environmental impact from existing sources and the estimation of the effects of possible equipment modification/improvement.

# 2. Modeling method

#### 2.1 Zone of study

The studied area in Saraburi province covers about 45 square kilometers with a population of over 70,000. The topographical contours of the area, actual sources or plant locations [1] and 11 selected receptor positions are marked in Figure 1. In 2000 there was only a single monitoring station located at Na Pra Laan (receptor P1) and operated by the Department of Pollution Control, Ministry of Science, Technology and Environment, which had rather extensive records of ambient PM<sub>10</sub> concentration and some local meteorological data. In the present simulations a variety of scattered receptor points was

selected and meteorological condition and measured PM<sub>10</sub> concentration during January 6-12, 2000, were used to validate the suitability of the present model.

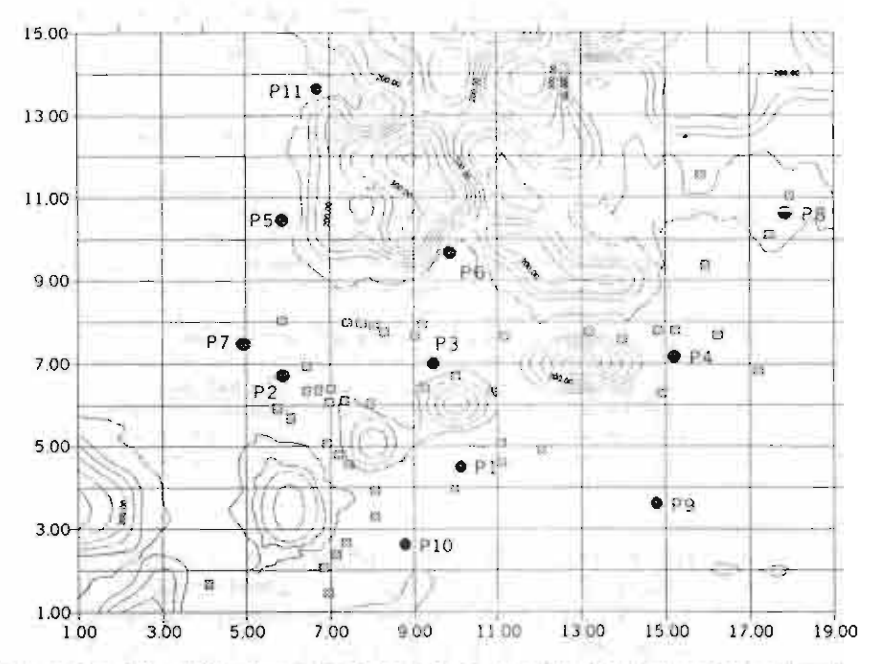


Figure 1 Map of the study area with locations of stone-processing plants (square dots) and receptors (round dots) [The numbers on the two axes are the assigned grid numbers]

### 2.2 Equation of motion for the atmospheric air

The following Navier-Stokes equation for uns.eady imcompressible viscous flow in dimensionless conservative form is used. Dimensionless flow velocities in this generalized coordinate system are defined as follows:

$$U = \frac{\partial \hat{i}}{\partial x} U + \frac{\partial \hat{i}}{\partial y} V + \frac{\partial \hat{i}}{\partial z} W, V = \frac{\partial \eta}{\partial x} U + \frac{\partial \eta}{\partial y} V + \frac{\partial \eta}{\partial z} W, W = \frac{\partial \zeta}{\partial x} U + \frac{\partial \zeta}{\partial y} V + \frac{\partial \zeta}{\partial y} W$$
 (1)
The contravariant flow velocity components U, V, and W correspond to the direction

components î, ç and æ. The continuity and Navier-Stokes equations can be rewritten as follows [2, 3]:

$$\frac{\partial q}{\partial t} + \frac{\partial E}{\partial \xi} + \frac{\partial F}{\partial \eta} + \frac{\partial G}{\partial \zeta} = Re^{-1} \left( \frac{\partial R}{\partial \xi} + \frac{\partial S}{\partial \eta} + \frac{\partial T}{\partial \zeta} \right)$$
 (2)

Where

$$Q = J^{-1}\begin{bmatrix} 0 \\ u \\ v \end{bmatrix}, E = J^{-1}\begin{bmatrix} uU + \frac{\partial \xi}{\partial x} \rho \\ vU + \frac{\partial \xi}{\partial y} \rho \\ wU + \frac{\partial \xi}{\partial z} - \rho \end{bmatrix}, F = J^{-1}\begin{bmatrix} uV + \frac{\partial \eta}{\partial x} \rho \\ vV + \frac{\partial \eta}{\partial y} \rho \\ wV + \frac{\partial \eta}{\partial z} \rho \end{bmatrix},$$

$$Q = J^{-1}\begin{bmatrix} w \\ uW + \frac{\partial \zeta}{\partial x} \rho \\ vW + \frac{\partial \zeta}{\partial y} \rho \\ wW + \frac{\partial \zeta}{\partial z} \rho \end{bmatrix}, R = J^{-1}\begin{bmatrix} g_1 \frac{\partial u}{\partial \xi} + g_2 \frac{\partial u}{\partial \eta} + g_3 \frac{\partial u}{\partial \zeta} \\ g_1 \frac{\partial v}{\partial \xi} + g_2 \frac{\partial v}{\partial \eta} + g_3 \frac{\partial v}{\partial \zeta} \\ g_1 \frac{\partial w}{\partial \xi} + g_2 \frac{\partial v}{\partial \eta} + g_3 \frac{\partial v}{\partial \zeta} \end{bmatrix},$$

$$S = J^{-1}\begin{bmatrix} g_2 \frac{\partial u}{\partial \xi} + g_3 \frac{\partial u}{\partial \eta} + g_3 \frac{\partial v}{\partial \zeta} \\ g_2 \frac{\partial v}{\partial \xi} + g_4 \frac{\partial v}{\partial \eta} + g_5 \frac{\partial v}{\partial \zeta} \\ g_2 \frac{\partial w}{\partial \xi} + g_4 \frac{\partial w}{\partial \eta} + g_5 \frac{\partial v}{\partial \zeta} \end{bmatrix}, T = J^{-1}\begin{bmatrix} g_3 \frac{\partial u}{\partial \xi} + g_5 \frac{\partial u}{\partial \eta} + g_6 \frac{\partial u}{\partial \zeta} \\ g_3 \frac{\partial v}{\partial \xi} + g_5 \frac{\partial v}{\partial \eta} + g_6 \frac{\partial v}{\partial \zeta} \\ g_3 \frac{\partial w}{\partial \xi} + g_5 \frac{\partial v}{\partial \eta} + g_6 \frac{\partial v}{\partial \zeta} \\ g_3 \frac{\partial w}{\partial \xi} + g_5 \frac{\partial w}{\partial \eta} + g_6 \frac{\partial w}{\partial \zeta} \end{bmatrix},$$

$$Q_1 = \begin{pmatrix} \frac{\partial i}{\partial x} \end{pmatrix}^2 + \begin{pmatrix} \frac{\partial i}{\partial y} \end{pmatrix}^2 + \begin{pmatrix} \frac{\partial i}{\partial z} \end{pmatrix}^2 + \begin{pmatrix} \frac{\partial w}{\partial z}$$

 $J^{-1}$  = the inverse of the Jacobian determinant  $[J = \partial(x, y, z) / \partial(\xi, \eta, \zeta)]$ 

#### 2.3 Dispersion equation for the PM<sub>10</sub>

For simplicity PM<sub>10</sub> is treated here as a typical gaseous pollutant. The equation for particulate dispersion in Cartesian coordinates is as follows:

$$\frac{\partial C}{\partial t} + \left( u \frac{\partial C}{\partial x} + v \frac{\partial C}{\partial y} + w \frac{\partial C}{\partial z} \right) = \frac{\partial}{\partial x} \left( K_{H} \frac{\partial C}{\partial x} \right) + \frac{\partial}{\partial y} \left( K_{V} \frac{\partial C}{\partial y} \right) + \frac{\partial}{\partial z} \left( K_{H} \frac{\partial C}{\partial z} \right) + Q$$
 (3)

Here  $K_H$  and  $K_V$  are the effective horizontal and vertical dispersion coefficients, respectively. Q is the amount of pollutant released per volume per unit time. Converted to the generalized coordinate system, equation (3) becomes

$$+ K_{v} \left[ \frac{\partial}{\partial \xi} (J^{-1}h_{1} \frac{\partial c}{\partial \xi} + J^{-1}h_{2} \frac{\partial c}{\partial \eta} + J^{-1}h_{3} \frac{\partial c}{\partial \zeta}) \right] + K_{v} \left[ \frac{\partial}{\partial \eta} (J^{-1}h_{2} \frac{\partial c}{\partial \xi} + J^{-1}h_{4} \frac{\partial c}{\partial \eta} + J^{-1}h_{5} \frac{\partial c}{\partial \zeta} \right]$$

$$+ K_{v} \left[ \frac{\partial}{\partial \zeta} J^{-1}h_{3} \frac{\partial c}{\partial \xi} + J^{-1}h_{5} \frac{\partial c}{\partial \eta} + J^{-1}h_{6} \frac{\partial c}{\partial \zeta} \right] + J^{-1}Q$$

$$+ K_{v} \left[ \frac{\partial}{\partial \zeta} J^{-1}h_{3} \frac{\partial c}{\partial \xi} + J^{-1}h_{5} \frac{\partial c}{\partial \eta} + J^{-1}h_{6} \frac{\partial c}{\partial \zeta} \right] + J^{-1}Q$$

$$+ K_{v} \left[ \frac{\partial}{\partial \zeta} J^{-1}h_{3} \frac{\partial c}{\partial \xi} + J^{-1}h_{5} \frac{\partial c}{\partial \eta} + J^{-1}h_{6} \frac{\partial c}{\partial \zeta} \right] + J^{-1}Q$$

$$+ K_{v} \left[ \frac{\partial}{\partial \zeta} J^{-1}h_{3} \frac{\partial c}{\partial \xi} + J^{-1}h_{5} \frac{\partial c}{\partial \eta} + J^{-1}h_{6} \frac{\partial c}{\partial \zeta} \right] + J^{-1}Q$$

$$+ K_{v} \left[ \frac{\partial}{\partial \zeta} J^{-1}h_{3} \frac{\partial c}{\partial \xi} + J^{-1}h_{5} \frac{\partial c}{\partial \zeta} \right]$$

$$+ K_{v} \left[ \frac{\partial}{\partial \zeta} J^{-1}h_{3} \frac{\partial c}{\partial \xi} + J^{-1}h_{5} \frac{\partial c}{\partial \zeta} \right]$$

$$+ K_{v} \left[ \frac{\partial}{\partial \zeta} J^{-1}h_{3} \frac{\partial c}{\partial \zeta} + J^{-1}h_{5} \frac{\partial c}{\partial \zeta} \right]$$

$$+ J^{-1}h_{5} \frac{\partial c}{\partial \zeta}$$

$$+ J^{-$$

For simplicity, measured wind velocity and direction at receptor P1(10m. above the ground) are assumed constant during the period of simulation and used to estimate the upper atmospheric velocity via the ¼ power law. As for the discretization, 3D QUICK scheme [3] is applied to finite-difference approximation of the nonlinear terms and Adams-Bashforth algorithm, to numerical time integration [2], respectively.

#### 3. Results and Discussion

#### 3.1 Validation of the mathematical model

First of all, historical meteorological data and past records of PM<sub>10</sub> concentration are used to confirm the suitability of the model parameters, particularly the vertical dispersion coefficient (K<sub>V</sub>) of 1 m<sup>2</sup>/s and horizontal dispersion coefficient (K<sub>H</sub>) of 200 m<sup>2</sup>/s for the stable atmospheric condition during, for example, January 6-12,2000. Figure 2 shows that most of the predicted 24-hr-average ambient PM<sub>10</sub> concentrations are close to the available values at receptor P1 (Na Pra Laan). Thus it may be considered that the above parameters are suitable for perdicting the PM<sub>10</sub> distribution in this area during the period of interest.

In order to grasp the situation of air quality in the study zone before implementation of dust control, the predicted 24-hour and weekly averages of  $PM_{10}$  concentrations at the other receptors are used. From the Table 1, it is found that during January 6-12, 2000, the predicted  $PM_{10}$  concentrations at 5 receptors (P2, P3, P4, P8 and P10) out of the 11 exceeded the Thai air quality standard of 120  $\mu g/m^3$ . Due to the terrain of these locations and the prevalent wind direction, flowing mostly from south-western to north-eastern, the predicted  $PM_{10}$  concentrations at the 5 receptors were quite high.

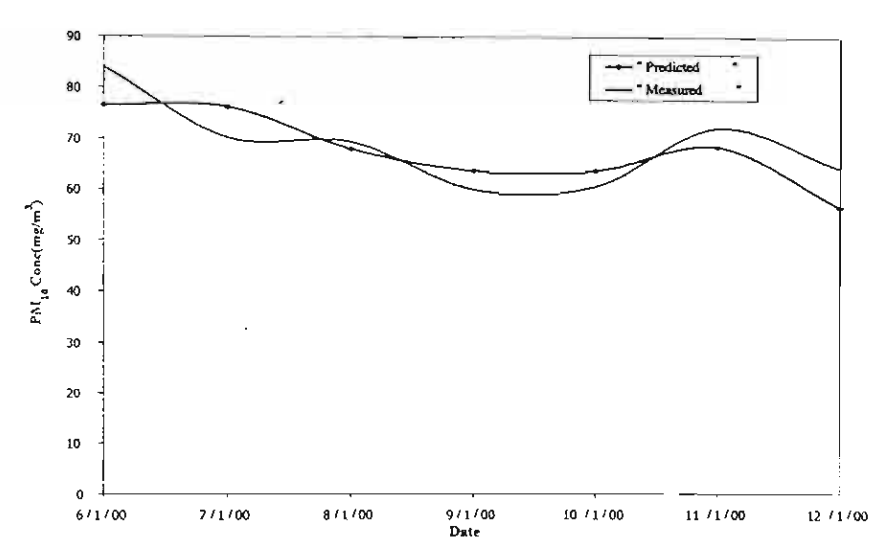


Figure 2 Comparison between the predicted 24-hr-average ambient concentration of PM<sub>10</sub> at a receptor (P1), 10 meter above the ground, and its counterpart value measured at the monitoring station at Na Pra Laan during January 6-12, 2000

Table 1 The predicted 1-week-average concentration of PM<sub>10</sub> before and after dust control implementation (January 6-12, 2000)

Receptor No.	Location	Before implementation	After implementation		
		PM <sub>10</sub> conc. (μg/m³)	PM <sub>10</sub> conc. (μg/m³) under unstable condition	PM <sub>10</sub> conc. (µg/m) under stable condition	
I.	Na Pra Laan	65.51	2.18	13.10	
ž -	Ban Chap Cha Aom	161.20	4.03	32.24	
3	Wat Kung Khao Khew	130.61	3.73	26.12	
4	Wat Khao Rock	130.01	11.31	26.00	
5	Wat Pu Dam Bunpot	2.09	0.07	0.42	
6	Wat Dam Sri Wilai	3.90	0.11	0.78	
7	Ban Tan Thong Daeng School	18.48	0.46	3.70	
8	Saraburi Cement	218.61	8.74	43.72	
9	Ban Khao Ngob	7.64	0.22	1.53	
10	Ban Nong Bo Phrong	148.36	3.30	29.67	
11	Ban Kung Pa Yang	0.34	0.01	0.07	

# 3.2 Evaluation of effect of 80% emission reduction

To evaluate the effectiveness of the announced 80% reduction of fugutive dust from the stone processing plants, the model was used to predict the 24-hour and 1-week-average  $PM_{10}$  concentrations during January 6-12, 2000, under both stable ( $K_v = 1 \text{ m}^2/\text{s}$ ) and unstable ( $K_v = 10 \text{ m}^2/\text{s}$ ) conditions. Table 1 shows that none of the predicted  $PM_{10}$  concentrations at any receptors exceeded the Thai air quality standard under either atmospheric condition. It should be noted that, when atmospheric stability changes from

unstable to stable condition, the 1-week-average PM<sub>10</sub> concentrations could increase up to 8 folds at a number of the receptors.

#### 4. Conclusion

To save space only the weekly-average  $PM_{10}$  are shown in Table 1. Nevertheless, the some conclusions can more or less be reached using the daily average values. A sensitivity analysis has also been carried out to understand quantitatively the effects of the key model parameters and the wind conditions. To increase the reliability of the conclusions, the period of the study will be extended to one year or even longer. So far the following tentative conclusions have been obtained.

- 1. For a majority of the receptors, the wind direction has more effect on the  $PM_{10}$  concentration than the wind speed because of the relatively calm wind condition ( $\leq 2$  m/s). 2. Under stable atmospheric condition, the  $PM_{10}$  concentrations at some receptors can increase up to 8 times those under unstable condition.
- 3. The target of 80% reduction of fugitive dust gives a satisfactory level of air quality in Saraburi Province under both unstable and stable atmospheric conditions.

5. Acknowledgement

P.V., T.C. and W.T. received financial support from Thailand Research Fund (Research Team Promotion of W.T. 1996-2002). The Pollution Control Department has kindly supplied useful information and monitoring data. Dr. S. Chiba, Yokkaichi university, provided the computer program for adapting the Cartesian grid to the topography-hugging generalized grid.

#### Nomenclature

 $C = instant concentration (\mu g/m^3)$ 

P = atmospheric pressure (bar)

 $\xi$ ,  $\eta$ ,  $\zeta$  = independent variables in generalized space

K<sub>H</sub> = horizontal dispersion coe: ficient (m<sup>2</sup>/s or cm<sup>2</sup>/s)

K<sub>v</sub> = vertical dispersion coefficient (m<sup>2</sup>/s or cm<sup>2</sup>/s)

u = wind speed in x direction (horizontal direction)

v = wind speed in y direction (vertical upward direction)

= wind speed in z direction (horizontal direction)

J = Jacobian determinant

Re = Reynolds number (-)

# Reference

- Meechumna, P. et al., Research Project on Environmental Management to Solve Dust Pollution Problem from Stone Mining Site and Processing Plants around Tambol Nah Pra Larn and its Vicinity in Saraburi Province, Final report submitted to Department of Mineral Resources of Industry, (1999): 4-1, 7-44.
- Takemoto, Y., and Nakamura, Y., Diffusion Simulation of Ground Level Concentration Discharge of Pollutants in the Yokkaichi, J. of Yokkaichi University., 9 (1996): 263-280.
- Takemoto, Y., Nakamura, Y., Yamabe, H. Abe, Y. and Minami, I., A curvilinear coordinate method for the solution of incompressible Navier-Stokes equations using the third-order upwind difference scheme, Trans. JSIDRE (Japan), 61(1986): 56-65.

# MICROWAVE DRYING FOR SYNTHESIS OF MESOPOROUS CARBON GELS

Hajime Tamon<sup>1</sup>, Shin R. Mukai<sup>1</sup>, Hirotomo Nishihara<sup>1</sup>, Takashi Yoshida<sup>1</sup>,

Takuji Yamamoto<sup>2</sup>, Nattaporn Tonanon<sup>3</sup> and Wiwut Tanthapanichakoon<sup>3</sup>

Department of Chemical Engineering, Kyoto University Kyoto 606-8501, Japan
tamon@chemc.kyoto-u.ac.jp

National Institute of Advanced Industrial Science and Technology
1-1-1 Higashi, Tsukuba 305-8565, Japan

Department of Chemical Engineering, Chulalongkorn University
Bangkok 10330, Thailand

Mesoporous carbon gels are usually obtained by pyrolyzing resorcinol-formaldehyde gels, which are synthesized via the sol-gel polycondensation of resorcinol with formaldehyde in a slightly basic aqueous solution followed by drying. In the drying stage, supercritical drying is usually used to prevent the shrinkage of the structure of the gels which occurs during drying. The authors have shown that mesoporous carbon gels can also be obtained using freeze drying instead of supercritical drying. In this work, the authors verified the possibility of using a more economical drying method, microwave drying. It was found that mesoporous carbons could be successfully obtained using microwave drying, by adjusting synthesis conditions such as catalyst concentration. The utilization of microwave drying is expected to contribute to the reduction of the production cost and to the large-scale production of mesoporous carbon gels.

#### Characterization

The porous properties of carbon gels were determined by nitrogen adsorption. The adsorption and desorption isotherms were measured at 77 K using an adsorption apparatus (BEL Japan, Inc.; BELSORP28). BET surface area,  $S_{\rm BET}$ , mesopore size distribution, and mesopore volume were evaluated. The pore size distribution and the mesopore volume,  $V_{\rm mes}$ , were determined by applying the Dollimore-Heal method (Dollimore and Heal, 1964) to the desorption isotherm.

The cross sections of carbon gels were observed using a scanning electron microscope (JEOL, Ltd.; JSM-6340FS).

#### Results and Discussion

Porous properties of carbon gels

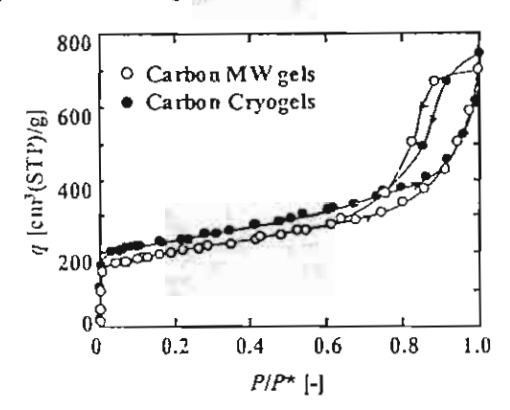


Figure 1. N<sub>2</sub> adsorption-desorption isotherms on carbon cryogels and carbon MW gels at 77K (R/C=400 mol/mol, R/W=250 kg/m<sup>3</sup>)

Figure 1 shows the adsorption-desorption isotherms of nitrogen on carbon cryogels and carbon MW gels prepared under the conditions of R/C=400 mol/mol and R/W=250 kg/m<sup>3</sup>. It can be seen that both of the isotherms on carbon cryogel and carbon MW gel are IV type. Figure 2 shows pore size distributions of carbon gels prepared under the conditions of R/C = 400 mol/mol and R/W = 250 kg/m<sup>3</sup>. From this figure, one can see that the both distributions are almost the same. It can be noticed that the carbon gel prepared using microwave at the drying stage shows mesoporosity similar to or even superior to that prepared using freezedrying. This result shows that microwave drying can be used instead of

supercritical or freeze-drying to obtain mesoporous carbon gels if appropriate values of R/C and R/W are selected.

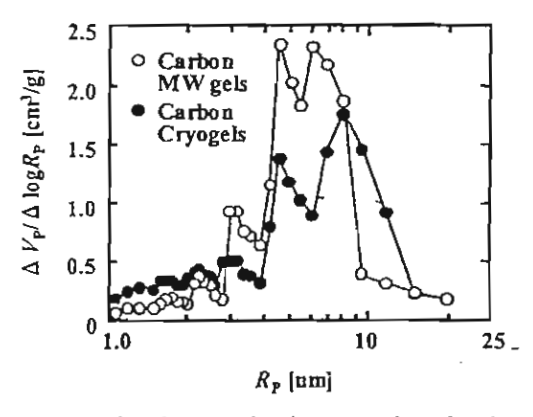


Figure 2. Mesopore size distributions of carbon cryogels and carbon MW gels (R/C=400 mol/mol, R/W=250 kg/m3)

# Synthesis conditions for preparing mesoporous carbon MW gels

The R/C and R/W values of the precursor solution are varied to clarify the range which microwave drying is effective for obtaining mesoporous carbons. Previously the authors found that the growth behavior of the colloidal particles, which are generated in the precursor solution and eventually transform into a hydrogel, highly depends on the C/W [mol/m<sup>3</sup>] value of the solution (Yamamoto et al., 2001b). Therefore, the porous properties of the resulting carbon gels are thought to be practically governed by this value. Hence, the BET surface areas, SBET, and mesopore volumes, V<sub>mes</sub>, of the carbon MW gels are plotted against the C/W values of their precursor solutions as shown in Figures 3 and 4. The values of carbon cryogels are also plotted for comparison. Mesoporous carbon cryogels can be obtained at a wide range of C/W values. On the other hand, at high C/W values, carbon gels prepared using microwave drying do not show significant porosity. It is assumed that the unique gel structure, which is the origin of the mesoporosity of carbon gels, collapsed during microwave drying. However, at low C/W values smaller than 20 mol/m3, mesoporous carbon gels could also be obtained using microwave drying.

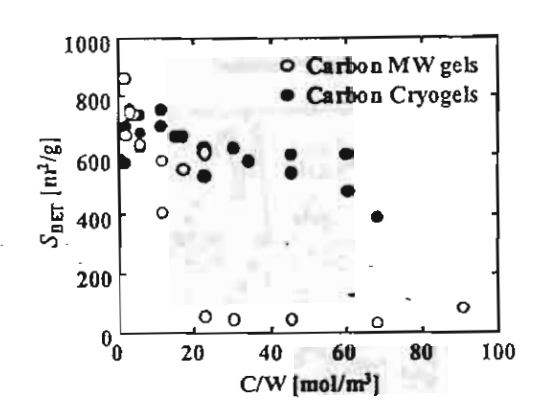


Figure 3. Relation between the C/W values and BET surface areas of carbon cryogels and carbon MW gels

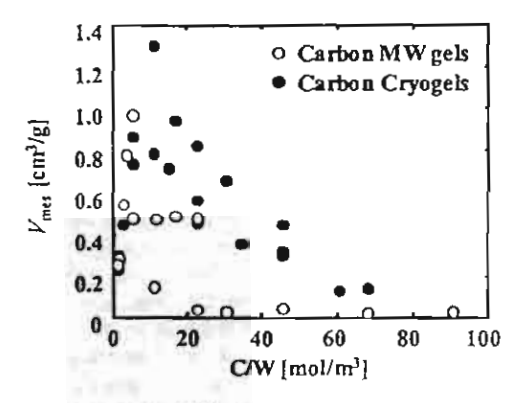


Figure 4. Relation between the C/W values and mesopore volumes of carbon cryogels and carbon MW gels

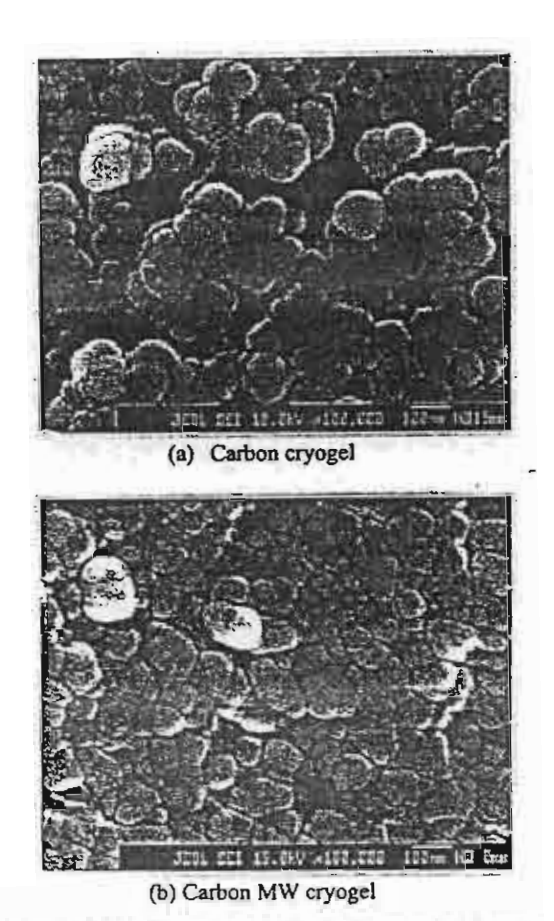


Figure 5. SEM image of cross sections of carbon cryogel and carbon MW gel prepared (R/C = 400 mol/mol, R/W = 250 kg/m³, C/W = 5.7 mol/m³)

Figure 5 shows the cross sections of carbon cryogel and carbon MW gel prepared under the conditions of R/C = 400 mol/mol, R/W = 250 kg/m<sup>3</sup>, C/W = 5.7 mol/m<sup>3</sup>. One can see that the carbon cryogel is composed of primary particles of around 100 nm diameter as shown in Figure 5 (a). Figure 5 (b) shows that the carbon MW gel is also composed of primary particles. Hence the pictures suggest that the carbon gels with almost the same structure as the carbon cryogel can be prepared by using microwave drying.

Figure 6 shows the cross sections of carbon MW gel prepared under the conditions of R/C = 50 mol/mol, R/W = 500 kg/m³, C/W = 91 mol/m³. The primary particles composing the carbon MW gel are shown to have melted

by pyrolysis. The carbon MW gel has no mesopores, which fact supports the mesoporosity estimated by nitrogen adsorption as shown in Figure 4.

From the above results, freeze drying and microwave drying are recommendable to prepare mesoporous carbon gels. It is confirmed that freeze drying is available to prepare mesoporous carbon cryogels over wide ranges of C/W values. When microwave drying is used, the C/W values should be kept smaller than 20 mol/m<sup>3</sup> to obtain mesoporous carbon MW gels.

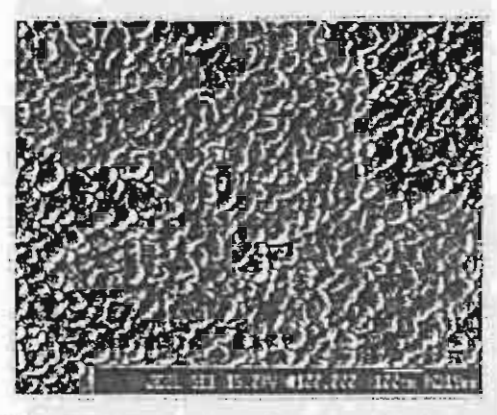


Figure 6. SEM image of cross sections of carbon MW gel prepared  $(R/C = 50 \text{ mol/mol}, R/W = 500 \text{ kg/m}^3, C/W = 91 \text{ mol/m}^3)$ 

# Conclusion

For the preparation of mesoporous carbon gels, microwave drying was evaluated from the viewpoint of the ranges of the ratio of catalyst to water (C/W). The following conclusions were obtained.

- Freeze drying is effective to prepare mesoporous carbon gels over wide ranges of C/W values.
- (2) Microwave drying is also available to preparing mesoporous carbon gels for the range of C/W values smaller than 20 mol/m³.
- (3) The utilization of microwave drying is expected to contribute to the reduction of the production cost and to the large-scale production of mesoporous carbon gels.

# Acknowledgements

This work was partially supported by Japan Society for the Promotion of Science, Grant-in Aid for Scientific Research (B) No. 14350416 (2002), and Industrial Technology Research Grant Program in 2001 from New Energy and Industrial Technology Development Organization (NEDO) of Japan. H. T., S. R. M. and N. T. exchanged visits for collaborative research under TJTTP-JBIC Program of Chulalongkom University. W. T. received partial financial support from Thailand Research Fund (TRF-RTA Project).

### Notation

P vapor pressure

[kPa]

saturated vapor pressure [kPa]

q amount of nitrogen adsorbed [cm³/g]

R<sub>p</sub> pore radius

SBET BET surface area

 $[m^2/kg]$ 

V<sub>p</sub> pore volume

[cm³/kg]

V<sub>mes</sub> mesopores volume
[cm³/kg]

#### References

- Dollimore, D., Heal, G.R. 1964. An improved method for the calculation of pore-size distribution from adsorption data. J. Appl. Chem. 14:109-114.
- Pekala, R.W. 1989. Organic aerogels from the polycondensation of resorcinol with formaldehyde. J. Mater. Sci. 24:3221-3227.
- Pekala, R.W., Alviso, C.T. 1992. Carbon aerogels and xerogels. Mater. Res. Soc. Symp. Proc. 270:3-14.
- Tamon, H., Ishizaka, H., Mikami, M. and Okazaki, M. 1997. Porous structure of organic and carbon aerogels synthesized by sol-gel polycondensation of resorcinol with formaldehyde. Carbon 35:791-796.
- Tamon, H., Ishizaka, H., Araki, T. and Okazaki, M. 1998. Control of mesoporous structure of organic and carbon aerogels. Carbon 36:1257-1262.
- Tamon, H. and Ishizaka, H., 1999a, Preparation of organic mesoporous gel by supercritical/freeze drying, Dry. Technol. 17:1653-1665.

[nm]

particles. After reaching above the peripheral bed level, these particles naturally rain back onto the two lateral regions existing between the hollowed core and the vessel walls. Thus, the overall bed is composed of a dilute -phase central core (spout region), through which the particles are moving upward by a concurrent flow of fluid, and a dense phase (lateral regions), through which the particles slowly travel down and inwards as a loosely packed bed (Kunii, D. and O. Levenspiel, 1991).

To obtain good detailed insights into the highly complex phenomena occurring within the spouted bed, highly sophisticated measuring instruments and experimental know-how are indispensable. Therefore reliable mathematical modeling and simulation of the two-phase system with minimum simplifying assumptions is a powerful alternative tool. Recently, Discrete Element Method (DEM) has successfully been employed to simulate two-phase flows with solid particles or droplets. For instance, Tsuji et al. (1992) employed the technique to elucidate plug flow of non-cohesive particles in a horizontal pipe. Tsuji et al. (1993) also extended the technique to investigate solid particle motion in a twodimensional fluidized bed with draft plates. They reported that the main characteristics of the spouting phenomena, such as minimum spouting velocity, particle motion and circulation, are in good agreement with the experimental observations. However, the mixing of solid particles inside the bed is discussed only qualitatively. The objective of this work is to study particle and fluid dynamics in a two-dimensional slanted-base spouted bed without draft plates. The characteristics of interest are minimum spouting velocity, velocity profiles of gas and particles, and degree of particle mixing.

#### TWO-PHASE FLOW MODEL

Fluid Motion

The following locally averaged equation of continuity and equation of motion are used to calculate the fluid motion in the spouted bed (Tsuji et al, 1993).

Equation of continuity of fluid

$$\frac{\partial}{\partial t}\varepsilon + \frac{\partial}{\partial x_j}(\varepsilon u_j) = 0 \tag{1}$$

Equation of motion of fluid

$$\frac{\partial}{\partial t}(\varepsilon u_i) + \frac{\partial}{\partial z}(\varepsilon u_i u_z) = -\frac{\varepsilon}{\rho_s} \frac{\partial p}{\partial z} + f_{pi}$$
 (2)

where p, u,  $\varepsilon$  and  $\rho_8$  are the pressure, fluid velocity, void fraction and fluid density respectively. The term represents the interaction between the fluid and particles. It is given by the following correlation.

$$f_{\rho i} = \frac{\beta}{\rho_g} \left( \overline{v}_{\rho i} - u_i \right) \tag{3}$$

in which  $\overline{\nu}_{pi}$  is the average particle velocity. The value of the coefficient  $\beta$  is obtainable from Ergun's equation in case of the dense phase [4] and Wen and Yu's equation in case of the dilute phase (Wen & Yu 1966). SIMPLE method [6] is used to integrate the equation of fluid flow.

# Particle Motion

The particle motion is individually and simultaneously integrated and tracked using the discrete element method (DEM) (Tsuji et al,1992,1993). Generally the forces acting on a particle are: the gravitational force ( $f_g = mg$ ), the fluid drag force ( $f_D$ ) and the various types of contact forces ( $f_C$ ). Newton's law is applied to each particle as follows:

$$\ddot{x} = \frac{f_C + f_D}{m} + g \tag{5}$$

where m is the mass of particle.

Meanwhile the rotational motion of each particle is governed by the following equation.

 $\ddot{\omega} = \frac{T}{I} \tag{6}$ 

where T is the torque caused by the tangential components of the contact forces, and I is the moment of inertia of the particle.

# Degree of Mixing

Since the state of particle mixing in the spouted bed is be characterized quantitatively in this work, the following definition for the degree of mixing in a selected sampling cell (or sampling region) is employed here. For simplicity the particles in the bed are divided into 2 groups to be called A and B. Initially particles A and B are completely segregated.

$$\sigma_p^2 = \sum (x_i - \bar{x}_c)^2 / N$$

$$\sigma_a^2 = x_c (1 - \bar{x}_c)$$
(7)

Degree of mixing =  $1 - \sigma_P / \sigma_o$ 

where

X<sub>c</sub> is the numerical composition of particles A in the bed

 $X_i$  is taken as unity for each particle A and zero for each B in the sampling cell

N is the total number of particles in the sampling cell

 $\sigma_p^2$  is the sample variance of the composition of  $\Lambda$  in the sampling cell  $\sigma_o^2$  is the expected variance of particles A upon complete segregation, a maximum

Particle		-
Diameter, d <sub>P</sub> (mm)	8.0	
Density, $\rho_p$ (kg/m <sup>3</sup> )	1,231	
Sphericity	1	1
Spouted bed		
Width, W (mm)	495	
Depth, L <sub>b</sub> (mm)	40	
Width of gas inlet, W1 (mm)	33	
Slant angle, θ (degree)	60	θ

FIGURE 1 Two-dimensional spouted bed

When the state of particle mixing evolves from complete segregation to homogeneous (completely random) mixing, the above degree of mixing will change from zero to unity.

# **RESULTS AND DISCUSSION**

# Simulating Conditions

The particle properties and geometry of the spouted bed are summarized in Table 1. The total number of particles is either 10,000 or 26,000, which corresponds to a bed height of 0.409 m or 0.769 m, respectively. The coefficient of friction and the coefficient of restitution are respectively 0.3 and 0.9. The value of spring constant is 800 N/m for the contact force model. The magnitude of the integration time step is 0.0003 sec, which is estimated using the oscillation period of the spring-mass system as recommended by Tsuji et al. Ambient air at 20°C and 1 atm is fed into the spouted bed. The grid size for calculating the gas flow is 11 mm × 19 mm. The properties of the particles are similar to shelled comparticles.

#### Minimum Spouting Velocity (U<sub>ms</sub>)

When the injected air velocity is not sufficiently high, expansion of the bed will occur mostly in the lower region of the central axis. As the air velocity is gradually increased, the pressure drop will likewise increase while the voidage

expansion will progressively penetrate the bed along its axial direction. At a certain value of air velocity, the voidage expansion will ideally reach the bed surface and the spouting phenomenon will begin. When the air velocity is further increased, it will result in a significant decrease in the pressure drop. Subsequently, the pressure drop will remain fairly constant as the air velocity is further increased. The minimum spouting velocity  $(U_{ms})$  is experimentally obtained while slowly decreasing the air flow and observing the bed behavior. Here the minimum spouting velocity  $(U_{ms})$  is determined as the point at which the pressure drop begins to rise steeply. The reported value of  $U_{ms}$  is based on the superficial air velocity over the entire cross section of the empty rectangular bed, not the injected air velocity.

Figures 2(a) and (b) show the observed relationship between the pressure drop and the reduced superficial air velocity for the bed heights of 0.409 m or 0.769 m, respectively. The theoretical value of  $U_{ms}$  obtained from a simple correlation is approximately 1.746 m/s irregardless of the bed height (Ergun,1952). However, the simulation results reveal that  $U_{ms}$  is 2.0 for bed height = 0.409 m and only poor bubbling fluidization is observed for bed height = 0.769 m. The discrepancy between the predicted and theoretical values could be attributed to the fact that a simple force balance between the weight of a particle bed and the drag force is used to estimate the minimum fluidizing velocity ( $U_{mf}$ ) without taking the complicated colliding and rotating effects into account. In addition, the mechanical energy dissipated by the air jet to cause spouting should depend on the bed height. In fact the observed snapshots of the particles inside the bed indicate that true spouting does not occur for bed height = 0.769 m but only slugging and bubbling take place.

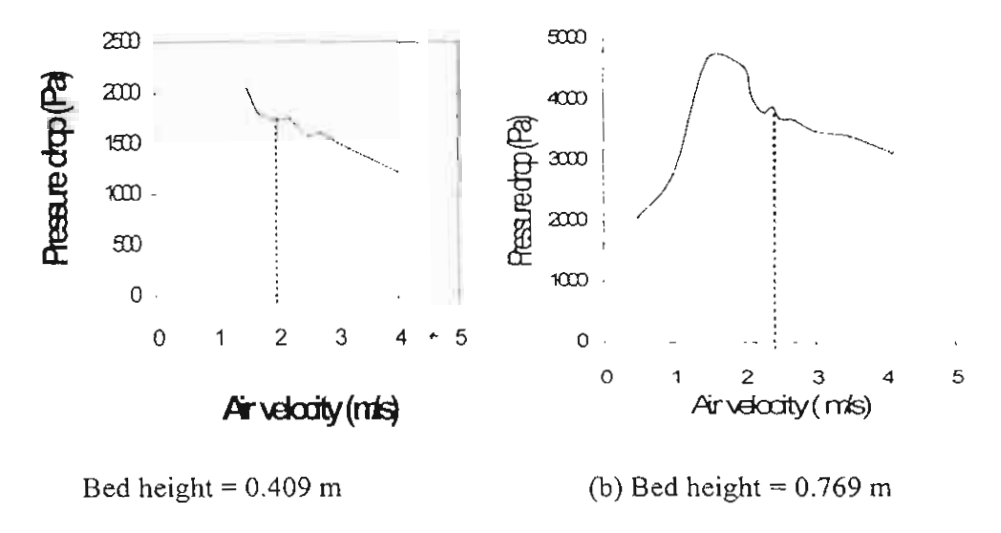
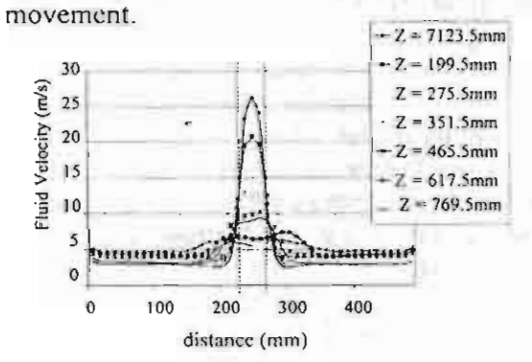
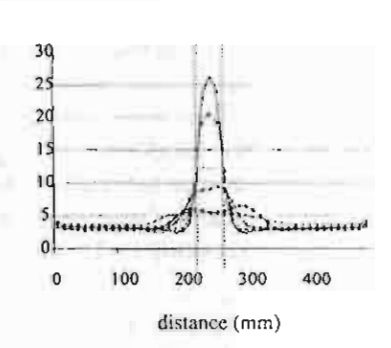


FIGURE 2 Relation between predicted pressure drop and superficial air velocity

Spatial Distributions of Fluid and Particle Velocity

Figures 3(a) and 3(b) show the spatial distributions of air velocity U<sub>Z</sub> inside the bed for the two bed heights. In the figures, the superficial gas velocity is set equal to their predicted U<sub>ms</sub>, namely 2.0 and 2.2 m/s, respectively. In each case, the air velocity in the central core is higher than the two lateral regions at the same height. The highest U<sub>Z</sub> is located just above the injection zone because the local void fraction there is the largest. Consequently, air can penetrate more easily through this central core region. As seen in the figures, the profile of U<sub>Z</sub> seems to be symmetric on both side of the spouted bed, especially for the lower bed height. Below a certain bed height, especially near the air inlet, the U<sub>Z</sub> is quite high because of the jetting and bubbling phenomena. Similarly, figures 4(a) and 4(b) show the average particle velocity profile at selected bed heights for the two cases. Particles are initially accelerated to a high velocity near the air inlet and they gradually decelerate by collisions while moving up the bed. The average particle velocity V<sub>Z</sub> not only decreases along the horizontal distance from the central core but it could become negative, thus indicating downward

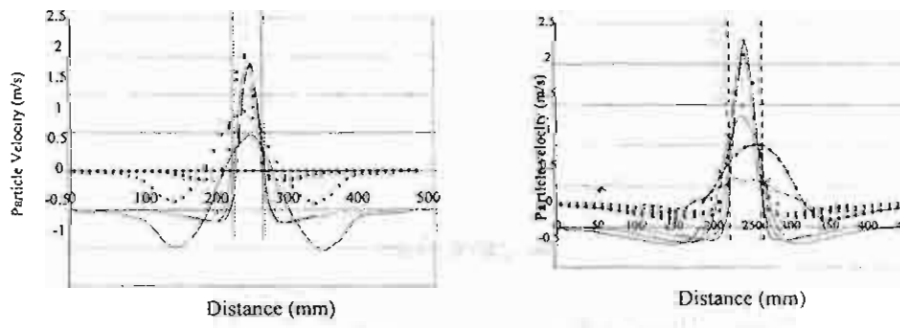




(a) Bed height = 0.409 m

(b) Bed height = 0.769 m

FIGURE 3 Predicted spatial distribution of air velocity Uz inside the spouted bed



(a) Bed height = 0.409 m

(b) Bed height = 0.769 m

FIGURE 4 Predicted spatial distribution of time-smoothed particle velocity V<sub>z</sub> inside the spouted bed (Legends are the same as those of Figure 3)

# DEGREE OF MIXING

Figure 5(a) shows the change of the degree of particle mixing with respect to the operating time in the case of bed height = 0.409 m at various superficial air velocities. The degree of mixing quickly approaches unity. Initially, its value strongly oscillates because the spouting effect is not yet steady. As the system approaches the steady state, the degree of mixing becomes nearly constant. It is interesting to note that a higher superficial air velocity has insignificant effect on the final degree of mixing. Figure 5(b) displays the change of the degree of mixing for bed height = 0.769 m. As expected, the mixing of particles is significantly poor and its value falls in the range between 0.5 and 0.6. The superficial air velocity exhibits a similar effect on the degree of mixing as in the case of bed height = 0.409 m though it takes longer to approach the steady state.

To elucidate more clearly the effect of the bed height on the degree of mixing, Figure 6 compares the degree of mixing for the case of minimum superficial spouting velocity = 2.0 m/s. Generally speaking, the higher the bed height, the larger the amplitude of oscillation.

#### CONCLUSION

The simulation results predict that, for the two-dimensional spouted bed without any draft plates, the minimum superficial spouting velocity  $(U_{ms})$  is approximately 2.0 m/s for bed height = 0.409 m. As expected, the fluid as well as particle velocities are highest in the central core, especially next to the gas inlet. Good mixing of particles takes place in the spouted bed as long as the air velocity is not slower than  $U_{ms}$ . For Bed height = 0.769 m, the spouting phenomenon can no longer be observed. Only poor fluidization could be observed.

#### **ACKNOWLEDGEMENT**

W.T. and T.C. received financial support from TRF-RTA (Prof. W. Tanthapanichakoon). The calculating facilities are partially supported by the Government-Industry Collaborative Research Fund granted to Center of Excellence in Particle Technology (CEPT) of Chulalongkom University. The original DEM source code was provided by Y. Tsuji et. al. of Osaka University as the joint research under TJTTP-JBIC.

#### LITERATURE CITED

Kunii, D. and O. Levenspiel. "Fluidization Engineering," Butterworth-Heinemann, 1991.

Tsuji, Y., T. Tanaka and T. Ishida; "Lagrangian numerical simulation of plug flow of cohesionless particles in a horizontal pipe," *Powder Technol.* 71, 239-250 (1992).

Tsuji, Y., T. Kawaguchi and T. Tanaka; Discrete particle simulation of two-dimensional fluidized bed, *Powder Technol.* 77, 79-87 (1993).

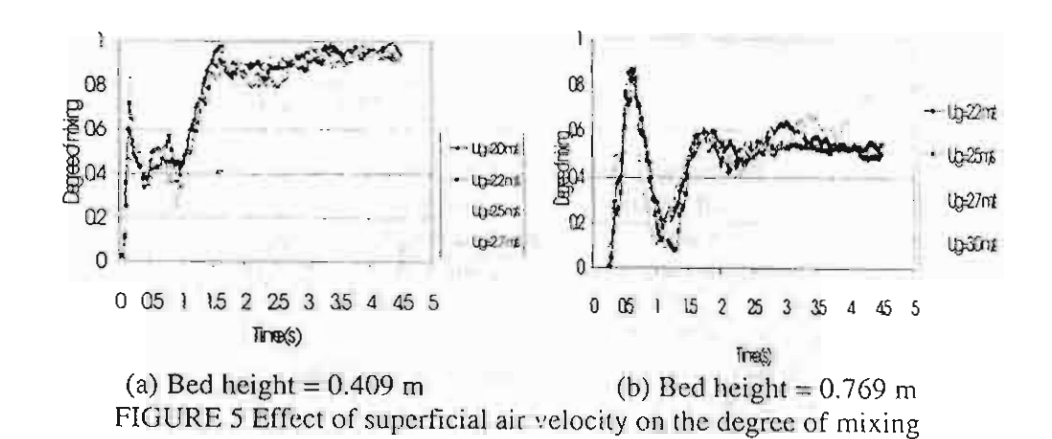
Ergun, S.; "Fluid flow through packed columns," Chem. Eng. Prog., 48 (2), 89-94 (1952).

Wen, C.Y. and Y.H. Yu; "Mechanics of Fluidization," Chem. Eng. Prog. Symp. Ser., 62 (62) 100-111 (1966).

Patankar, S.V.; "Numerical heat transfer and fluid flow," McGraw-Hill, 1980.

Cundall, P.A. and O. D. L. Strack; "A discrete numerical model for granular assemblies," *Geotechnique* 29 (1), 47-65 (1979).

Crowe, C., M. Sommerfeld and Y. Tsuji; "Multiphase flows with droplets and particles," CRC Press, 1998.



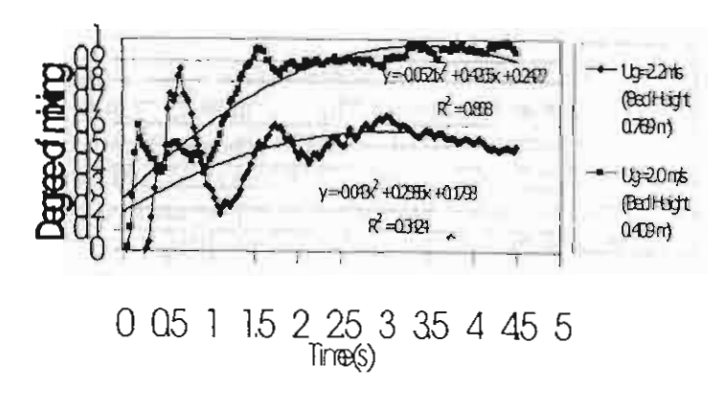


FIGURE 6 Effect of bed height on the degree of mixing

# Removal of Acetaldehyde in Oxygen-Nitrogen Mixture by a Wetted-Wall Corona Discharge Reactor

K. Faungnawakij<sup>1, 2</sup>, N. Sano<sup>2</sup>, T. Kanki<sup>2</sup>, W. Tanthapanichakoon<sup>1</sup>

Department of Chemical Engineering, Chulalongkorn University, Patumwan, Bangkok, Thailand, 10330 Department of Chemical Engineering, Himeji Institute of Technology, 2167 Shosha, Himeji, Japan, 671-2201

A wetted-wall corona discharge reactor, which consists of a wire cathode stretched along the center of cylindrical anode covered with a thin water film, was employed on removal of acetaldehyde in gas mixture of oxygen and nitrogen. The plasma reactions in the reactor produce radicals and ions, which drift to the interfacial water to produce reactive radical OH in water. Acetaldehyde is removed from gas stream by simultaneous absorption and gas corona reaction. The absorbed acetaldehyde in water is decomposed by the aqueous OH radical. There is an optimized corona current for highly effective removal performance.

#### 1. Introduction

Atmospheric discharge processes have widely been investigated for gas purification for example D.C. corona discharge [1-2], pulsed corona discharge [3], and barrier discharge [4]. Among these processes, the D.C. corona discharge is considered to be successful in removal of dilute target gases with high efficiency and relatively low by-product formation [1-2]. A wetted-wall corona discharge reactor, one type of D.C. corona discharge reactors, is proposed to enhance the removal efficiency by ionization-assisted absorption [2]. Recently, it was found that the wetted-wall reactor can be effectively used for not only gas purification but also water purification [6]. In the water purification process, the aqueous hydroxyl radical, OH, generated by the direct contact of coronainduced gaseous ions and radicals with the interfacial water decomposes the organic compounds

Considering these features, it can be expected that, along with gaseous removal corona reaction, the absorbed organic compounds from the gas stream can be decomposed in the aqueous phase, leading to sustainable absorption.

# 2. Experimental

The experimental setup is shown in Fig. 1. The wetted-wall corona discharge reactor consists of cylindrical anode (34-mm inner diameter and 200-mm length) and a wire cathode (0.34-mm diameter) stretched at the center of the anode. A D.C. high voltage generator with negative polarity is used to apply the high voltage ranging from -6 to -13 kV to the wire cathode to generate a corona discharge, while the anode is connected to the ground. The corona region length is fixed at 140 mm by insulating both top and the bottom parts of the cathode. The gas stream of acetaldehyde, O<sub>2</sub> and N<sub>2</sub>

is flowed through the reactor at 100 cm<sup>3</sup>/min while the water is circulated to make a falling thin film over the inner wall of the cylindrical anode at 1400 cm<sup>3</sup>/min. The temperature of the circulating water is controlled at 10 °C by flowing through a heat exchanger unit.

An FID gas chromatograph (GC) was used to analyze the treated gas, and ozone concentration was measured by KI method. For analysis of the circulating water, the FID gas chromatograph, a total organic curbon analyzer, and a high performance liquid chromatograph (HPLC) with a UV-VIS detector were employed.

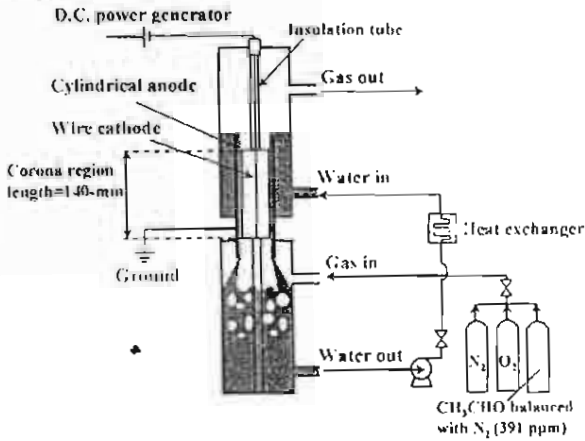


Figure 1. The experimental apparatus

### 3. Results and Discussion

When corona discharge is generated, electrons are emitted from the wire cathode and then drift toward the liquid film. In the corona plasma region where the electron energy is higher than 1.85 eV [6], dissociation and ionization of oxygen can produce O, O', etc [7-8]. In the low energy electron region next to the narrow plasma zone, dissociative electron attachment to oxygen and water vapor would produce O, O', OH, etc [7-8]. When the charged and

uncharged species produced in the corona discharge reach the liquid film on the cylindrical anode by the electric force and the convection induced by the ion wind, these species react with water molecules to produce reactive radicals at the interfacial water. These radicals, such as OH radical, contribute to the degradation of the organic contaminants in water. When an organic compound in the gas stream enters the corona zone, the removal of the organic compound is achieved by electron attachment [1-2], cluster formation [2], radical reactions [9], and so forth. It was explored by gas analysis inside the reactor that majority of acetaldehyde is absorbed into the water before entering the corona zone, and therefore the aqueous acetaldehyde is mainly decomposed by the reactive radicals in water.

Figure 2 shows the outlet concentration of Cog during discharge gaseous acetaldchyde operation with 200 ppm inlet concentration Circuit When the corona discharge is not generated, Cong drastically increases with time, suggesting that the absorbed acetaldehyde is accumulated in water and inhibits the absorption rate. When the corona discharge is generated, the increase in increasing  $C_{ng}$ is attenuated. When the corona current is higher than 0.1 mA, the Cag can be kept constant indicating that the removal of acetaldehyde by absorption along with gas corona reactions becomes steady state. However, the steady state concentration of acetaldehyde cannot be obtained when the current is so low as 0.02 mA.

Figure 3 shows the concentration of aqueous acetaldehyde in circulating water  $C_w$  during discharge operation. Without the corona discharge,  $C_w$  increases with time. This is because acetaldehyde is continuously absorbed into the water until  $C_w$  reaches its saturation. When corona is generated, the increasing  $C_w$  is retarded because the absorbed acetaldehyde is decomposed by reaction with OH radical. The increase in corona current causes the increase in decomposition rate since OH radical can be more produced by increasing electron flux. When corona current is so low as 0.02 mA, the increase in  $C_w$  cannot be effectively attenuated, which is consistent with the increase in  $C_{o,a}$  as mentioned above.

According to the by-product analysis by GC and HPLC, the aqueous by-product is detected with the same retention time as acetic acid whereas other by-products are negligible. There is no significant by-product detected in treated gas. This result could suggest that the acetaldehyde might be mainly decomposed in aqueous phase.

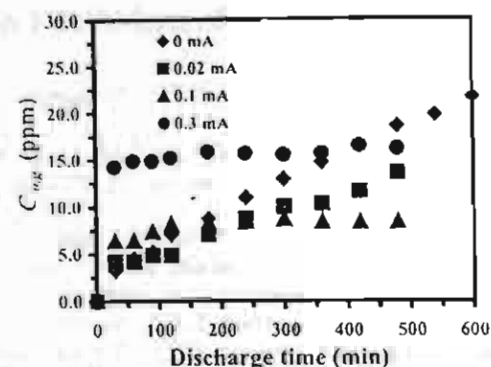


Figure 2. Concentration of acetaldehyde in treated gas during discharge operation ( $C_{i,e}$ =200ppm, [ $O_{i,e}$ ]=21%)

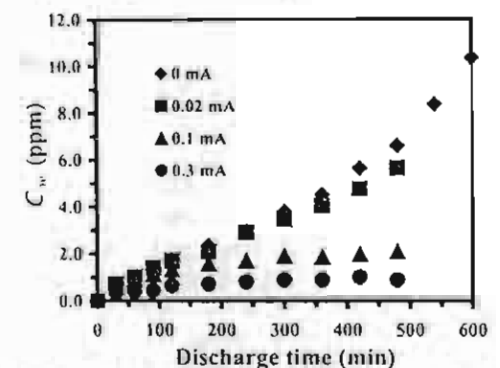


Figure 3. Concentration of acetaldehyde in circulating water during discharge operation ( $C_{e,g}$ =200ppm  $[O_2]$ =21%)

# Acknowledgment

Thailand Research Fund-Royal Golden Jubilee Ph.D. Program (TRF-RGJ), Research Team Award (TRF-RTA) and AIEJ Student Exchange Program are gratefully acknowledged.

# References

- [1] H. Tamon et al., AIChE J., 41 (1995) 1701-
- [2] N. Sano et al., J. Chem. Eng. Japan., 29 (1996) 59-64.
- [3] L. Huang et al., Ind. Eng. Chem. Res., 40 (2001), 5481- 5486.
- [4] T. Yamamoto et al., IEEE Trans. Ind. Appl., 28 (1992) 528-534.
- [5] N. Sano et al., Ind. Eng. Chem. Res., 42 (2003) 5423-5428.
- [6] J. Chen; J.H. Davidson, Plasma Chem. Plasma P., 23 (2003) 83-102.
- [7] R. Peyrous et al., J. Phys. D: Appl. Phys., 22 (1989), 1658-1667.
- [8] J.L. Moruzzi et al., J. Chem. Phys., 45 (1966) 4617- 4627.
- [9] C.R. Melarnon et al., Ind. Eng. Chem. Res., 39 (2000) 2779-2787.

Influence of Oxygen on Removal of Gaseous Acetaldehyde by Wetted-Wall Corona Discharge Reactor (学)K. Faungnawakij<sup>2,1</sup>, N. Sano<sup>1,\*</sup>, D. Yamamoto<sup>1</sup>, T. Kanki<sup>1</sup>, T. Charinpanitkul<sup>2</sup>, W. Tanthapanichakoon<sup>2</sup> (1.Himeji Inst. Technol.)(2.Chulalongkorn Univ.)

#### 1. Introduction

A wetted-wall corona discharge reactor is one type of D.C. corona discharge reactor used for gas purification with high removal efficiency and low byproduct formation. In this reactor, some of the negative ions produced by electron attachment are absorbed into a falling liquid film on the anode surface. This absorption of the ions improves the removal efficiency of soluble gas components1.2). Moreover, the gas impurities absorbed into the water would be decomposed by reactive radicals and ozone created in the water3) by corona discharge. In addition, the anode self-cleaning action makes the wetted-wall reactor suitable for a long period of operation. Since oxygen seems to be a key component for this method,3) the effect of oxygen concentration was investigated and the removal mechanism was discussed based on the experimental results.

#### 2. Experimental

Fig.1 shows the experimental set-up. A high voltage (8-13 kV, negative polarity) was applied on a wire cathode (0.34 mm diameter, SUS) sustained at the center of a grounded cylindrical anode (34 mm inside diameter, 200 mm Length, SUS) to generate the corona. Gas mixture was fed downward trough the reactor by 100 cm3/min. The concentrations of acetaldehyde and oxygen in the gas mixture were adjusted by mixing commercial standard gases. De-ionized water was circulated as a falling film on the inner surface of the anode by 1400 cm<sup>3</sup>/min. For gas analysis, an FID gas chromatograph was used to analyze treated gas and ozone was measured by KI method. Meanwhile, the FID gas chromatograph and TOC analyzer were employed for analysis of the circulating water.

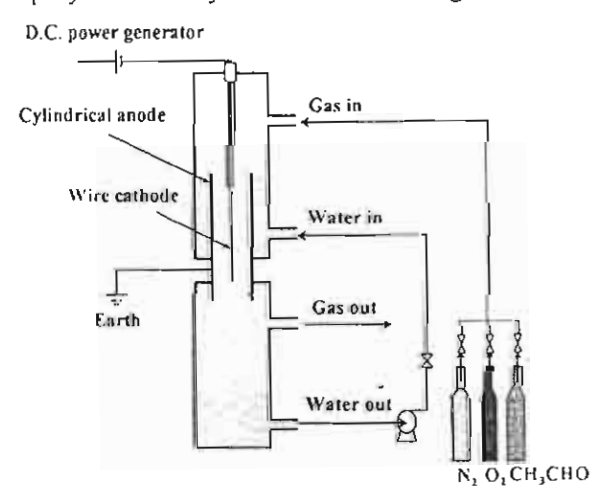


Fig.1 Experimental apparatus

# 3. Results and Discussion

The concentrations of acetaldehyde in treated gas were plotted against time in Fig.2. The results show that the stabilizing of concentrations of gaseous cannot be achieved in absence of oxygen. On the other hand, acetaldehyde was removed effectively in presence of oxygen. When the oxygen concentration was 5%, the concentration of acetaldehyde kept constant at about 5 ppm. When oxygen concentration was increased from 5 to 10 and 21 %, the outlet concentrations of acetaldehyde were increased to around 8 and 10 ppm, respectively. For the reason why the removal of acetaldehyde was inhibited by increase in oxygen may be attributed to coronainduced turbulence in the gas stream flowing inside the reactor. The corona wind velocity was measured by Pitot tube technique and showed that increase in oxygen concentration caused an increase in corona wind. It was considered that corona wind induced the turbulence inside the reactor that caused the shorter resident time, which was known to inhibit the conversion efficiency.

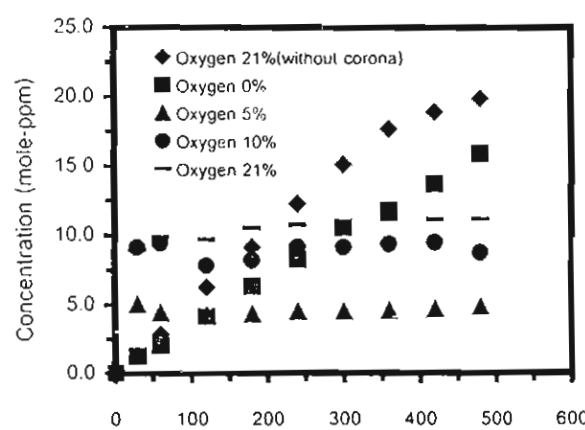


Fig.2 CH<sub>3</sub>CHO continuitgents the treated gas during discharge operation. Inlet conc.=200 mole-ppm; *I*=0.3 mA; Water volume=1000 cm<sup>3</sup>

#### 5. Acknowledgment

This research is supported by Thailand Research Fund-Royal Golden Jubilee Ph.D. Program (TRF-RGJ), Research Team Award (TRF-RTA) and AIEJ Student Exchange Program.

#### 4. Reference

Tamon, H. et al., AIChE J., 41, 1701-1711 (1995)
 Sano N. et al., J. Chem. Eng. Japan., 29, 59-64 (1996)

3)Sano N. et al., I. E. C. Res., 41, 5906-5911 (2002) TEL/FAX: 0792-67-4845

Corresponding author: sano@mech.eng.himeji-tech.ac.jp

# Removal of Acetaldehyde in Air by Wetted-Wall Corona Discharge Reactor

N. Sano<sup>1</sup> · OK. Faungnawakij<sup>2,1</sup> · D. Yamamoto<sup>1</sup> · T. Kanki<sup>1</sup> · W. Tanthapanichkoon<sup>2</sup> (1.Himeji Inst. Technol.)(2.Chulalongkorn Univ.)

#### 1. Introduction

A d.c. corona discharge is the powerful technique for gas purification at extremely low concentration <sup>11</sup>. However, the deposit formed at the anode during the removal process may induce re-entrainment when the reactor is operated for a long period. In order to solve this problem, the wetted-wall corona discharge reactor<sup>1,2</sup> is investigated here on the removal of acetaldehyde in air. Not only the formation of the deposit is prevented but also the gas impurities absorbed into the water would be decomposed by ozone and reactive radicals created in the water<sup>3)</sup> by corona discharge.

#### 2. Experimental

Fig.1 shows the experimental set-up. A high voltage (8-13 kV, negative polarity) is applied on a wire cathode (0.34 mm diameter, SUS) sustained at the center of a grounded cylindrical anode (34 mm inside diameter, 200 mm Length, SUS). In the gas phase, FID gas chromatograph (Shimadzu, GC-9A) was used to analyze treated gas and ozone was measured by KI method. In the water phase, the FID gas chromatograph (Shimadzu, GC-9A) was used to analyze acetaldehyde concentration. TOC and pH were monitored by TOC analyzer (Shimadzu, TOC-5000) and pH meter (Horiba, pH meter F-22), respectively.

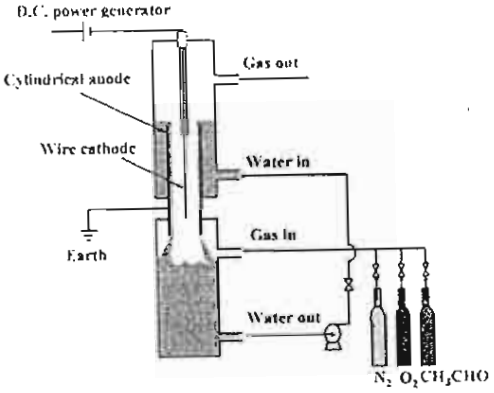


Fig.1 Experimental apparatus of removal of acetaldehyde using a wetted-wall corona discharge reactor.

# 3. Results and Discussion

The concentrations of acetaldehyde in the gas and water are plotted against time in Figs.2 and 3, respectively. The results show that the wetted-wall type exhibits clearly higher removal efficiency of acetaldehyde in air than the dry deposition type.

In the wetted-wall reactor, O, O<sub>2</sub>, O and OH are expected to be produced in gas corona discharge. When some of them reached the surface

of water film, reactive radical OH can be generated in water to decompose the organic compounds therein.

It was confirmed by gas analysis inside the reactor that acetaldehyde is absorbed into the water before entering the corona zone, and therefore the aqueous acetaldehyde was decomposed by the reactive radicals in water. When the current is high enough, further increase of aqueous acetaldehyde is prevented because of the effective decomposition.

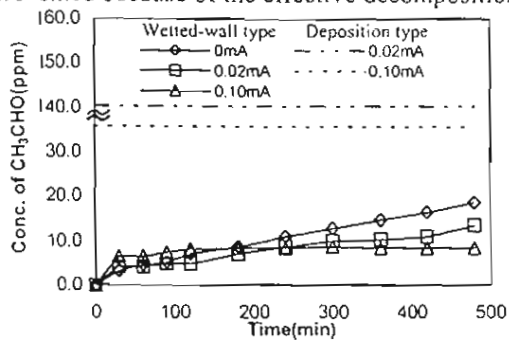


Fig.2 CH<sub>3</sub>CHO concentration in treated gas. Inlet conc.=200ppm:Gas flow rate=100cm<sup>3</sup>/min. Water volume=1000cm<sup>3</sup>:Corona length=140 mm. Water circulation rate: 1400cm3/min

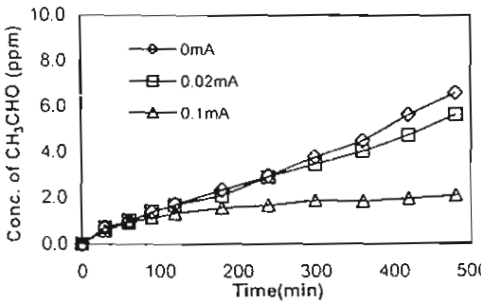


Fig.3 CH<sub>3</sub>CHO concentration in circulated water. Inlet conc.=200ppm:Gas flow rate=100cm<sup>3</sup>/min. Water volume=1000cm<sup>3</sup>:Corona length=140 mm. Water circulation rate=1400cm3/min.

#### 5. Acknowledgment

This research is supported by Thailand Research Fund-Royal Golden Jubilee Ph.D. Program (TRF-RGJ), Research Team Award (TRF-RTA) and AIEJ Student Exchange Program.

#### 4. Reference

1) Tamon, H. et al., AIChE J., 41, 1701-1711 (1995) 2) Sano N. et al., J. Chem. Eng. Japan., 29, 59-64 (1996)

3)Sano N. et al., I. E. C. Rcs., 41, 5906-5911 (2002) \*TEL/FAX: 0792-67-4845

e-mail: sano@mech.eng.himeji-tech.ac.jp

# Production of Carbon Nanoparticles using Submerged Arc in Solution

Poonlasak Muthakarn<sup>1,2,\*</sup>, Tawatchai Charinpanitkul<sup>1</sup>, Noriaki Sano<sup>2</sup>, Wiwut Tanthapanichakoon<sup>1</sup> and Tatsuo Kanki<sup>2</sup>

<sup>1</sup> Center of Excellence in Particle Technology, Faculty of Engineering, Chulalongkorn University, Bangkok 10330, THAILAND

<sup>2</sup> Department of Mechanical and System Engineering, Himeji Institute of Technology, University of Hyogo, 2167 Shosha, Himeji, 671-2201, JAPAN

Corresponding Author: Poonlasak.M@student.chula.ac.th

# **ABSTRACT**

Nowadays, arc discharge in water method has been accepted as one of the most economical methods to produce carbon nanoparticles (CNPs) because it does not require any costly vacuum system, high pressure, and other expensive equipments. Therefore many attempts to investigate the operating parameters affecting the yield of CNPs synthesis using this method have been conducted. Among those parameters, the effects of ion species dissolved in the water on the synthesis of CNPs have not been clearly understood. This investigation will be conducted to study the effect of aqueous ions added into the water. The aqueous species investigated are sodium carbonate representing ionic compound and ethanol representing organic species. As the preliminary results of our investigation using FESEM and TEM analysis, it is found that obtained CNPs consisted of multi-walled carbon nanotubes, polyhedral particles and crystalline product. The concentration of aqueous species has significant effect on the structure of the obtained CNPs. For the salt solutions, the ions provided an influence on the types of CNPs formed meanwhile the existence of hydrocarbons also gave rise to similar influence.

Keywords: carbon nanoparticles, are discharge in water, ion

#### INTRODUCTION

Several years ago, it is believed that carbon has only two structures, graphite and diamond (Fig.1). Since the continuous discoveries of bucky-ball, carbon nanotube, and other fullerene-family structures, intense efforts have been poured into studying for synthesis of those various kinds of carbon structures, especially novel carbon nanoparticles (CNPs). Nowadays, several fabrication methodologies have been proposed such as laser ablation, thermal pyrolysis of gaseous compound, plasma-enhanced chemical vapor deposition, high pressure CO conversion, arc discharge and so on [1-8]. However, it is well known that those conventional methods have highly setting and running costs for operation.

Hence, there have been some efforts on developing the novel economical processes to produce carbon nanoparticles by using submerged arc in de-mineralized water [9-15]. In order to maximize the yield of CNPs, many important parameters of the reaction should be optimized such as current density, gas pressure, temperature gradient in the reaction zone, concentration of carbon species and so on. Among those parameters,

Zhu et al. [10] have successfully produced high-quality multi-walled carbon nanotubes (MW-CNTs) by adding salts in water. Meanwhile ion species have some effects on formation of CNPs, but it has not been clearly understood.

The objective of this work is to investigate the effect of aqueous species (Na<sub>2</sub>CO<sub>3</sub> representing ionic compound and ethanol representing organic compound) on the yield and structures of CNPs by water arcing method.

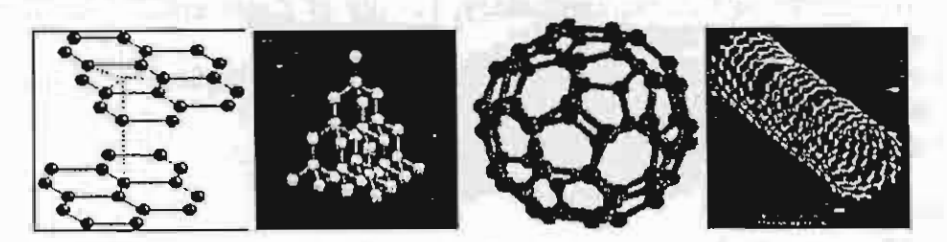
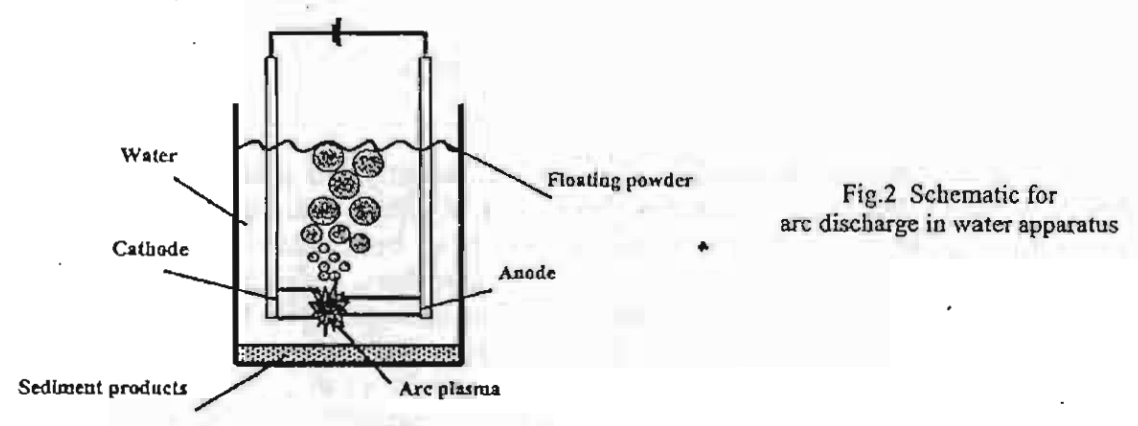


Fig. 1 Graphite, diamond, fullerene (C60) and carbon nanotubes structures (from left to right)

# EXPERIMENTAL

Schematic apparatus for synthesize carbon nanoparticles (CNPs) using submerged arc discharge is shown in Fig. 2. A direct current (dc) from welding machine is generated in water between a couple of (99.999% Toyo Tanso) pure graphite electrode in the demineralized water filled with aqueous additives of which concentration was carefully controlled. The stable arc current (50 A) and voltage (20-25 V) could be intentionally maintained after being initiated by approaching the anode to the stationary cathode and then constantly feeding the anode to maintain a cathode-anode gap of 1 mm.

The synthesized particles were characterized and analyzed by transmission electron microscopy (TEM; JEOL2010), field emission electron microscopy (FESEM; HITACHI, S-900), dynamic light scattering (DLS; MALVERN, ZETASIZER300HSA) and Raman spectroscopy (JASCO, NR1100).



# RESULTS AND DISCUSSION

#### Effect of addition of Na<sub>2</sub>CO<sub>3</sub> into de-mineralized water

It could be seen from FESEM image in Fig. 3 (a) that the synthesized products are mixtures of carbon nanoparticles with different morphology similar to those of previous investigations [9-15]. These CNPs are mainly composed of entangling multi-walled